# 國立交通大學

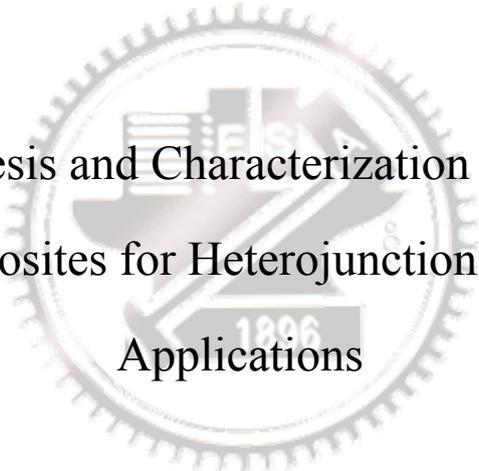## 材料科學與工程學系

## 博士論文

聚（3-己基噻吩）/硫化鎘複合物用於異質接面
太陽能電池上之合成與特性研究

In-situ Synthesis and Characterization of P3HT/CdS

nanocomposites for Heterojunction Solar Cell

Applications

研 究 生：廖泓洲

指導教授：陳三元 教授

中華民國九十九年六月

# 聚（3-己基噻吩）/硫化鎘複合物用於異質接面太陽能電池上之合成與研究
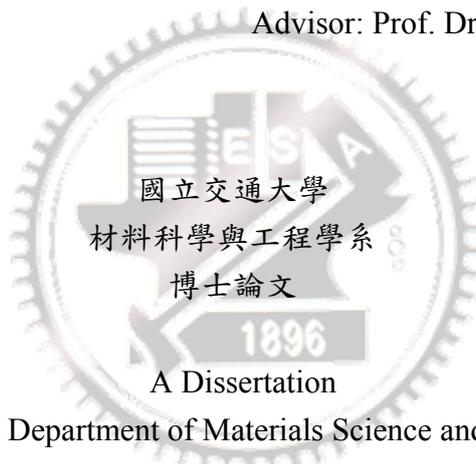
# In-situ Synthesis and Characterization of P3HT/CdS nanocomposites for Heterojunction Solar Cell Applications

學生: 廖泓洲　　　　　　　　　　　Student: Hung-Chou Liao

指導教授: 陳三元　　　　　　　　　Advisor: Prof. Dr. San-Yuan Chen

國立交通大學
材料科學與工程學系
博士論文

A Dissertation
Submitted to Department of Materials Science and Engineering
College of Engineering
National Chiao Tung University
In Partial Fulfillment of the Requirements for the Degree of Doctor of Philosophy
in

Materials Science and Engineering

June 2010

Hsinchu, Taiwan, Repubile of China

中華民國九十九年六月

# Contents

# Acknowledgments

First of all, I am greatly indebted to my advisor Prof. San-Yuan Chen for his kindness advices and useful discussions during my study period. He guided and encouraged me to use my potential to finish this thesis. Moreover, he taught me to how to research independently and deeply so I learned very much from him in academic research. In addition, I also have benefited much from his philosophy of life. I also sincerely thank Prof. Dean-Mo Liu for his fruitful discussions and constructive suggestions in thesis work. Moreover, Prof. Liu's assistance in editing of the English led my papers to much less errors and fluency.

I would like to thank the colleagues in my lab. They always inspired and accompanied me through any difficulty that I have to be overcome. I cannot finish this thesis without them. Finally, I want to thank my family for their unconditional supports during my study period.

# 摘要

太陽能電池的種類繁多，若以材料種類分類，可以分成：矽太陽能電池、無機化合物太陽能電池、染料敏化太陽能電池、有機太陽能電池等。其中是以單晶矽太陽能電池效率最高，但是其製作成本高，不符合經濟效益。而有機太陽能電池的

在能源危機的世代，研究出適合的再生能源是當務之急。而再生能源中又以太陽能電池受到大眾矚目。在太陽能電池領域中，矽太陽能電池一直是主要的發展對象。雖然它的轉換效率相當的高，但是價格卻不便宜且需要耗費大量能量來製造。因此發展大面積、低成本和低耗費量能的技術就顯得越來越重要。近年來，一種由有機物和無機物所組成的太陽能電池開始被大量的研究，其優點在於製作成本低，只需旋轉塗佈機便可以塗佈上作用層，再用加熱板加熱結晶，屬於低溫製程。造價低加上厚度薄，若是用於塑膠基板上變成可橈式太陽能電池，十分具有實用價值。因此在本論文主要在探討此一類型的太陽電池。

聚（3-己基噻吩）是目前最被廣泛被使用，因為其具有適合的能帶寬，高吸收係數和電洞的傳導係數。在本論文中，聚（3-己基噻吩）/硫化鎘複合物的合成，光學特性與太陽能電池元件的應用是主要的探討的部分。本論文首先利用水溶液法合成氧化鋅奈米柱，接著包覆一層氧化鎂，再利用熱處理得到氧化鎂摻雜的氧化鋅奈米柱。其光學和結構特性以 X 光繞射儀、穿透式電子顯微鏡、光激發光譜來鑑定。接著合成不同直徑的硫化鎘量子點修飾在氧化鋅奈米柱上再灌入聚（3-己基噻吩）製成太陽電池元件，發現因為量子侷限效應造成能階位移而促使電子躍遷變容易所以元件的效率升提 4 倍相較於沒有量子點的元件。然而雖然效率獲得提升，但是仍是太低，所以我們發展 in-situ 方法合成聚（3-己基噻吩）/硫化鎘複合物，在此方法中我們利用聚（3-己基噻吩）的分

子鏈作為模板，藉由改變實驗條件合成出不同長寬比的單晶硫化鎘，接著探討其太陽能轉換效率，發現轉換效率隨著長寬比而增加，當長寬比條件為 16 時可得最佳效率達到 2.9%。另外，我們也開始經由熱處理來研究聚（3-己基噻吩）和硫化鎘複之間的作用力和元件效率之間的關係。我們從聚（3-己基噻吩）/硫化鎘複合物的紫外光-可見光吸收光譜中發現藍位移且隨著長寬比增加而增加。此外聚（3-己基噻吩）/硫化鎘複合物的熱性質也會受到長寬比影響。因此可以推論硫化鎘的存在會減少聚（3-己基噻吩）的結晶度，而結晶度是可以經由熱處理得到回復，因此轉換效率有隨著熱處理的溫度和時間增加明顯的提升，然而過久的熱處理使得硫化鎘過度的聚集而造成轉換效率的衰退，而且此現象隨到長寬比減少而更明顯。從核磁共振光譜得知聚（3-己基噻吩）分子鏈和硫化鎘之間的作用力隨著長寬比而增強也因此因造成硫化鎘的聚集速率較慢，而使得元件效率對熱的穩定性較佳。

最後我們嚐試利用三維的電極取代平面電極來提升轉換效率，因此我們利用噴霧裂解法在氧化鋅奈米柱上製備具備低電阻率與高可見光穿透率的含氟氧化錫透明導電薄膜。由結果得知，當奈米柱的長度增長時，轉換效率隨著提升，但當長度長於 320 nm，高分子會有填充於奈米柱間隙不完全，造成轉換效率衰退。當使用三維的電極時對具有較長長寬比的硫化鎘而言會有填充於奈米柱間隙的問題，因此最佳的效率為 2.6%當長寬比條件等於 4。

# Abstract

Conventional solar cells were built from inorganic materials such as silicon. Although the efficiency of such conventional solar cells is high, very expensive materials and energy intensive processing techniques are required. The need to develop and deploy large-scale, cost-effective, renewable energy is becoming increasingly important. In recent years, a hybrid solar cell consisting of a combination of both organic and inorganic materials has achieved good power conversion efficiencies (PCE), which will become the focus in this thesis.

A series of P3HT/CdS composites have been synthesized to study the photovoltaic characteristics with ZnO nanorod arrays. First of all, we synthesize highly arrayed ZnO nanorod arrays via chemical process and attempt to fabricate MgO-doped ZnO nanorod arrays. The MgO-doped behavior and PL properties of single-crystal ZnO nanorods were investigated in terms of the annealing temperatures. Second, we evaluate an ordered organic-inorganic solar cell architecture based on CdS QD-decorated ZnO nanorod arrays encased in the hole-conducting polymer P3HT. A photovoltaic device based that has been decorated with CdS QDs yields power conversion efficiency over 4 times greater than that for a similar device without CdS QDs. The best device yields a short circuit current density of 1.38 $mAcm^{-2}$ under Air Mass (A.M.) 1.5 illumination (100 mW $cm^{-2}$), resulting in a power conversion efficiency of 0.21%. Third, we developed a novel method used to synthesize CdS single-crystal nanorods directly in the presence of conjugated polymer poly(3-hexylthiophene- 2,5-diyl) (P3HT), where the P3HT is acting as a molecular template for geometrical manipulation of CdS nanocrystals and in the meantime, as an

efficient charge conductor in composite form. The mechanism of in-situ growth of high-aspect-ratio CdS nanorod is proposed based on spectroscopic analysis. A considerably improved PL quenching was detected for the nanorods and suggested a result of electronic coupling between the high-aspect-ratio CdS nanorods and the conducting polymer matrix. A photovoltaic device consisting of CdS nanorods with aspect ratio (AR) of ca. 16 and the conjugated polymer poly-3(hexylthiophene) was well assembled and showed a power conversion efficiency of as high as 2.9% under A.M. 1.5 Global solar conditions. We found that the interaction between polymer chains and the CdS nanocrystals increased with the aspect ratio and thus the optical and thermal properties of P3HT/CdS composites change with the aspect ratios. The interaction also affected changes in the morphology of the active layer upon thermal treatment. Therefore, the performances of P3HT/CdS nanocrystals devices dramatically depended on annealing condtions. Finally, hybrid CdS/P3HT photovoltaic devices using F-doped $SnO_2$ (FTO)-coated ZnO nanorod arrays as electrodes were studied. The crystalline FTO made using the low-cost spray pyrolysis deposition (SPD) displayed a nominally complete and uniform coating over the entire outer surface of the ZnO nanorods. The incorporation of CdS into the P3HT much enhanced the Jsc of the devices with a nanorod FTO electrode. The PCE of the device with a ZnO nanorod length of 320 nm was increased from 0.37% for P3HT without CdS to 1.8% with CdS of aspect ratio=1 (spherical shape). With a further increase the AR of CdS nanocrystal to 4, the PCE was further increased up to 2.6%. Longer CdS nanocrystals conversely caused deterioration in PCE as result of the nanorod array morphology. These results indicate that, although increased nanorod length could improve the photocurrent and efficiency, other factors, such as P3HT infiltration, nanorod array morphology and CdS nanocrystal length are required for obtaining optimal performance of these devices.

# Chapter 1

# Introduction

Development of devices for conversion of solar energy into electricity has attracted a great attention in recent years due to strong interest in renewable energy and the problem of global climate changes. For many decades the solar cell industry has been dominated by inorganic solid-state devices, mainly based on silicon. Energy conversion efficiency of the best monocrystalline Si photovoltaic cells is nearly 25% [1, 2]. However, manufacturing of Si-based devices is very expensive due to strong requirement to the high purity of the crystalline semiconductor. Therefore, new ways of manufacturing solar cells that can scale up to large volumes and low cost are required. New materials or fabrication procedures that could reduce the cost of photovoltaic electricity substantially could help drive a rapid expansion in implementation of photovoltaic technology. Organic semiconductors such as conjugated polymers, small molecules and dyes, are particularly interesting for this purpose, largely because of the potential for processing such materials directly from solution, and so enabling low-cost manufacture of large-area thin semiconductor films. Because polymer cells have higher optical absorption coefficients than silicon, they are more efficient at absorbing light, which means that much thinner photovoltaic cells are required, such as poly(3-hexylthiophene- 2,5-diyl) (P3HT) and poly[2-methoxy-5-(3′,7′-dimethyloctyloxy)-1,4-phenylenevinylene] (MDMO-PPV). These conjugated molecules are electronically active because of their highly polarizable $\pi$-systems, which are hybridized orbitals based on the constituent $p$ atomic orbitals. The $\pi$−$\pi$* optical transitions are strong (absorption coefficients greater than

~$10^5$ cm$^{-1}$), typically fall in the visible, and can be tuned synthetically through molecular design. Charge carrier mobilities as high as 10 cm$^2$/V·s made them competitive with amorphous silicon. Furthermore, organic semiconductors have several advantages: (1) low-cost synthesis and (2) easy manufacture of thin film devices by vacuum evaporation/sublimation or solution cast or printing technologies.

Polymer-based devices based on the use of bulk heterojunctions can provide a large contact area between the donor and acceptor species. Bulk heterojunctions are formed by spin casting the polymer and an electron acceptor from a common solvent. Common acceptors used in polymer bulk heterojunctions are fullerenes, polymers, and *n*-type inorganic nanoparticles. Up to now, most of the literature has focused on blends of P3HT and the *n*-type inorganic nanoparticles. In general, high-quality nanocrystals of II–VI semiconductors such as CdS and CdSe can be prepared by chemical synthesis. However, a high surface energy of the small-sized semiconductor crystals often leads to their aggregation or oxidation. Therefore, an organic layer is required for surrounding the nanoparticles to prevent such processes. One of the most popular method is pyrolysis of organometallic precursors (Cd(CH$_3$)$_2$, bis(trimethylsilyl)sulfide or bis(trimethylsilyl)selenium) in a mixture containing trioctylphosphine oxide (TOPO), tributyl- or trioctylphosphine (TOP) and small amount of various phosphonic acids as a strong ligand for cadmium ions [3–6]. The organic ligand also ensures solubility of the nanocrystals in organic medium which is highly important for preparation of the nanoparticle–polymer blends. However, the organic ligand inhibits charge transfer between the polymer and the nanocrystals [7], resulting in a decreased power conversion efficiency. Therefore, an in-situ synthetic method was developed to directly grow CdS nanocrystals in a conducting polymer (P3HT) solution without surfactants or ligands and investigated the optical and photovoltaic properties of the P3HT/CdS composites in the thesis.

Another important polymer-based device technology stems from replacing nanoparticle with a vertically aligned inorganic semiconductor nanostructure, e.g. nanorod and nanotube arrays. The nanorods can help improve electron transport by avoiding the particle-to-particle hopping that occurs in the $n$-type inorganic nanoparticles. Furthermore, nanorods provide direct conduction pathways for the electrons from the point of injection to the collection electrode. Most successful organic/inorganic hybrid cells use transparent metal oxides, such as $TiO_2$ or ZnO, as the $n$-type semiconductor because of their high electron mobility, transparency, and ease of processing. Groups at NREL [8] and Imperial College London [9] have demonstrated EQE values of over 15% for P3HT–ZnO nanorod devices. Comparison with devices based on ZnO nanoparticles of similar diameter showed superior performance for the nanorod devices, apparently due in part to slower interfacial charge recombination in the nanorods than in the particles [9]. These polymer–ZnO nanorod devices have so far been limited by the relatively large rod diameters and correspondingly large pore volumes, which limit the efficiency of exciton dissociation, and by exciton harvesting, charge transport and $V$oc. Except creating the ideal nanostructure that enables maximum efficiency, we improved the charge transports between ZnO nanorod and P3HT by decorating CdS QDs to ZnO nanorods. Moreover, hybrid CdS/P3HT photovoltaic devices using F-doped $SnO_2$ (FTO)-coated ZnO nanorod arrays as electrodes were studied in this thesis.

An improvement of the photovoltaic efficiency requires a clear understanding of structure–properties relationships and numerous challenges related to synthesis of the composite materials and fabrication procedure of the device still remain to be overcome. In this way, the thesis is organized as follows. In **Chapter 2**, we will give a general introduction to the materials, working principles and literature reviews of the polymer solar cells. The experiment steps and characterization techniques employed

in this work were outlined in **Chapter 3**, that is, X-ray diffraction (XRD), transmission electron microscope (TEM), ultraviolet-visible (UV-vis), photoluminescence emission (PL), Raman, DSC, and scanning electron microscopy (SEM) for structure and morphology characterization, and optical and thermal properties, and I-V curve measurement for efficiency. In **Chapter 4**, we synthesize highly arrayed MgO-coated ZnO nanorod arrays via wet-chemical process. The MgO-doped behavior and PL properties of single-crystal ZnO nanorods were investigated in terms of the annealing temperatures. In **Chapter 5**, we study the photovoltaic characteristics of P3HT/ZnO nanorod solar cells by decorating CdS quantum dots (QDs) with different sizes on ZnO nanorods. The modification with CdS QDs can serve not only as a photosensitizer but mainly as an energy funnel and/or an electronic mediator to significantly improve the electron injection efficiency from P3HT to ZnO nanorods. The power conversion efficiency of the photovoltaic device based on that decorated with CdS QDs will be studied and compared with that for a similar device without CdS QDs.

In **Chapter 6**, we report a novel in-situ method to synthesize CdS single-crystal nanorods directly in the presence of conjugated polymer P3HT, where the P3HT is acting as a molecular template for geometrical manipulation of CdS nanocrystals and in the meantime, as an efficient charge conductor in composite form. Such a templating process allows the CdS nanorods with various aspect ratios to be easily manufactured via a controlled solvency of a co-solvent mixture, under which the conformational variation of the P3HT chain can be manipulated.

In **Chapter 7**, we focus on interaction between the P3HT and the CdS surface. ^{1}H NMR analysis indicates physical attachment between the CdS nanocrystals and the thiophene ring of P3HT; the interaction strength between the P3HT and CdS surface increases with the AR. The UV-vis spectra of the P3HT/CdS composite films show a

blue shift with an increasing AR of the CdS nanocrystals because CdS nanocrystals destruct the ordered structure of polymer chains as evidenced by the decrease in the melting point of P3HT main chain crystals. Atomic force microscope measurements on P3HT/CdS film demonstrate the aggregation of CdS nanocrystal in the P3HTmatrix is more apparent for the CdS nanocrystals of AR=4 than that of AR=16. It is concluded that upon annealing, a stronger interaction between P3HT and CdS for a larger AR (16) tend to reduce the CdS aggregation, which is favorable for the network structure and formation of percolation paths to increase the transport properties of the P3HT/CdS solar cells. Therefore, the PCE of the in-situ-growth P3HT/CdS with AR=16 composite shows a higher Photovoltaic performance.

In **Chapter 8**, we reported hybrid CdS/P3HT photovoltaic devices using F-doped SnO$_2$ (FTO)-coated ZnO nanorod arrays as electrodes using the low-cost spray pyrolysis deposition (SPD). The photovoltaic performance of CdS/P3HT photovoltaic devices was studied as a function of FTO-coated ZnO nanorod length and thickness of the FTO layer. However, although increased nanorod length could improve the photocurrent and efficiency, other factors, such as P3HT infiltration, nanorod array morphology and CdS nanocrystal length are required for obtaining optimal performance of these devices. Finally, conclusion and future researches will be summarized in **Chapter 9.**

# Chapter 2

# Theory and Literature Review

## 2.1 Electrical Characteristics of a Solar Cell

In Figure 2.1, the current-voltage characteristics are shown for a solar cell in the dark and under illumination. In the dark, there is almost no current flowing, until the contacts start to inject heavily at forward bias for voltages larger than the open circuit voltage. Under illumination, the current flows in the opposite direction than the injected currents. At (a) the maximum generated photocurrent flows under short-circuit conditions; at (b) the photogenerated current is balanced to zero (flat band condition). Between (a) and (b), in the fourth quadrant, the device generates power (i.e., current × voltage). At a certain point, denoted as maximum power point (MPP), the product between current and voltage and hence the power output is largest. The photovoltaic power conversion efficiency ( $\eta_e$ ) of a solar cell is determined by:

$$\eta_e = \frac{V_{OC} \times I_{SC} \times FF}{P_{in}} \tag{2.1}$$

$$FF = \frac{V_{mpp} \times V_{mpp}}{I_{SC} \times V_{OC}} \tag{2.2}$$

where $V_{OC}$ is the open circuit voltage, Isc is the short-circuit current, FF is the fill factor and Pin is the incident light power density, which is standardized at 1000 W/m$^2$ for solar cell testing with a spectral intensity distribution matching that of the sun on the earth's surface at an incident angle of 48.2$^o$, which is called the AM 1.5 spectrum [10]. I$_{mpp}$ and V$_{mpp}$ are the current and voltage at the maximum power point in the fourth quadrant of the current–voltage characteristics.

Generally, the I-V characteristics of a photovoltaic device can be described by

$$I = I_0 \cdot \{\exp(\frac{e}{nkT}(U - IR_S)) - 1\} + \frac{U - IR_S}{R_{SH}} - I_{PH} \qquad (2.3)$$

where $I_0$ is the dark current, e the elementary charge, n the diode ideality factor, U the applied voltage, $R_S$ the series, $R_{SH}$ the shunt resistance, and $I_{PH}$ is the photocurrent. The corresponding equivalent circuit is depicted in Figure 2.2. For a high FF, two things are required: (1) that the shunt resistance is very large to prevent leakage currents and (2) that the series resistance is very low to get a sharp rise in the forward current. The series resistance simply adds up from all series resistance contributions in the device, that is, from bulk transport, from interface transfer and from transport through the contacts.
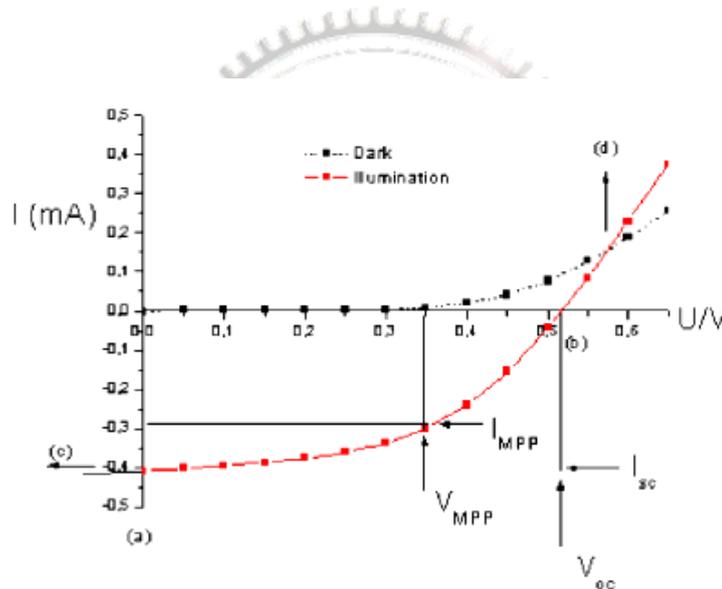


**Figure 2.1** Current–voltage (I–V) curves of an organic solar cell (dark, dashed; illuminated, red, full line).
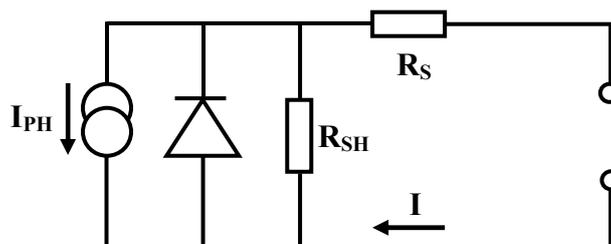


**Figure 2.2** Equivalent circuit for a solar cell.

7

## 2.2 Hybrid Conjugated Polymer-Semiconductor Solar Cells

A key development for polymer-based photovoltaic (PV) cells came from Tang [11] when he demonstrated the concept of bringing two semiconductors into contact to increase the power conversion efficiency (PCE). This interface is known as a heterojunction. The first dispersed polymer heterojunction PV cell was demonstrated by Yu et al. [12] in 1994. Nanoparticle–polymer cells generally have a photoactive layer consisting of interconnected semiconducting nanoparticles in a solid semiconducting polymer phase [13]. Crystalline inorganic nanoparticles have several attributes as electron acceptors, including relatively high electron mobility, high electron affinities, and good physical and chemical stability. The nanoparticles have at least one dimension within the range of 1 nm to ca. 100 nm that they are colloids. It combines the unique properties of inorganic semiconductors with the film-forming properties of the conjugated polymers [14]. Organic materials usually are inexpensive, easily processable, and their functionality can be tailored by molecular design and chemical synthesis. On the other hand, inorganic semiconductors can also be manufactured as processable nanoparticulate colloids and solution-processible nanocrystalline semiconductors that can be prepared in different morphologies offer the potential for a large area interface when combined with a solution-processed organic component.

Excitons created upon photoexcitation are separated into free charge carriers at interfaces between a conjugated polymer and inorganic semiconductors. Electrons will then be accepted by the material with the higher electron affinity (electron acceptor, inorganic semiconductors), and the hole by the material with the lower ionization potential, which also acts as the electron donor. The solubility of the n-type and p-type components is an important parameter of the construction of hybrid solar

cells processed from solutions. By varying the size of the nanoparticles, their band gap can be tuned and their absorption/emission spectra can be tailored [15].

## 2.2.1 Working Principles of Polymer-Semiconductor Solar Cells

The energy levels for a general polymer cell are shown in Figure 2.3. The photoactive layer contains a light harvesting material which acts as a photon absorber. Photons with energy greater than the band gap ($E_g$) are absorbed by the photoactive layer to create a neutral exciton by promotion of an electron from the highest occupied molecular orbital (HOMO) to the lowest unoccupied molecular orbital (LUMO) of the light harvesting polymer. An exciton can be considered as a bound electron-hole pair. The average length over which the exciton can diffuse within the polymer before recombination of the hole and electron occurs is the exciton diffusion length, $L_{ex}$ ($\approx$10 nm for P3HT). Exciton dissociation can take place at a suitable junction provided that recombination does not compete. (Recombination, which is the process whereby an electron and hole combine, results in annihilation of the charge carrier.) After dissociation the charges migrate to their respective electrodes as a result of an internal electric field generated by the difference in their Fermi levels.
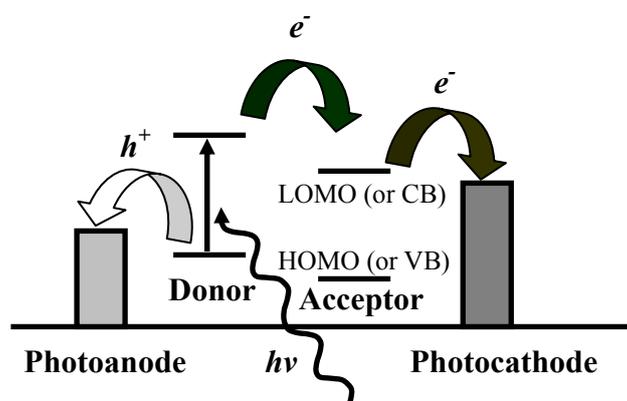


**Figure 2.3** Energy levels and the harvesting of energy from a photon for an acceptor/donor interface within a photoactive layer of a PV cell.

As mention above, each step has different efficiency and their product determines the external quantum efficiency (EQE) [16]:

$$EQE = \eta_A \eta_{diff} \eta_{sep} \eta_{tr} \eta_{cc} \qquad (2.4)$$

In Eq. (2.4) $\eta_A$ is the photon absorption yield (the number of generated excitons/the number of incident photons). This is determined by the optical absorption coefficient of the photoactive layer and its thickness.

The parameter $\eta_{diff}$ is the charge carriers diffusion yield (the number of diffusing excitons to the D–A interface/the number of generated excitons). If the average diffusion length that the exciton must travel to reach a heterojunction is relatively large compared to $L_{ex}$ then recombination of the charge carriers is favored and $\eta_{diff} < 1$.

$\eta_{sep}$ is the charge carries separation yield (the number of dissociated excitons/the number of excitons at the interface) which is the probability that the hole and electron will be separated by the internal electric field at a heterojunction. In most polymer semiconductors excitons have a binding energy of a fraction of an eV (below) and it is necessary to incorporate materials with a suitable offset in the energy levels within the photoactive layer to dissociate these excited states. In nanoparticle–polymer PV cells the nanoparticles have a relatively low electron affinity and accept electrons from the polymer under illumination. The electrons are accepted by the LUMO (in the case of organic nanoparticles) or the conduction band (in the case of inorganic nanoparticles) (Figure 2.3). The polymer acts as an electron donor. This process results in exciton dissociation. The energy required to separate the exciton [17] is ca. 0.4 eV in a polymer semiconductor. In a well designed nanoparticle–polymer cell the energy required to separate the exciton is provided by

the energy difference (offset) between the LUMOs of the donor and acceptor Figure 2.3).

$\eta_{tr}$ is the charge transport yield in the donor and acceptor materials (the number of the free charge carriers transported to the collecting electrode/the number of the charge carriers dissociated at D–A interface). Charge transport involves hopping processes and is affected by traps in the composite film. Traps originate from structural defects or impurity species. They provide localized energy minima of variable depth for charge transport which reduce charge mobility.

$\eta_{cc}$ is the charge collection yield (the number of the charge carriers in the external circuit/the number of the charge carriers transported to the electrode). The collection of charge at the electrodes is crucial to overall efficiency. This parameter represents the ability of the charges to be transferred from the photoactive layer to the electrodes. It is a function of the energy levels of the components (Figure 2.3) and the interfacial contacts between the photoactive layer and the electrodes. High $\eta_{cc}$ values can occur when (a) the Fermi level of the photoanode is greater than the energy level of the donor's HOMO and (b) the energy level of the acceptor's LUMO is greater than the Fermi level of the photocathode (Figure 2.3).

In photovoltaic p–n junction cells the driving force for the charge transport is a built-in potential $V_{bi}$ [18]. According to the simplified model, in metal/insulator/metal devices it corresponds to the difference between the work functions of the collecting electrodes and may be estimated by measuring the open circuit voltage, $V_{OC}$, at high illumination intensity and zero dark current. It turns out, however, that the barrier height only weakly depends on the metal used, because of Fermi level pinning to the semiconductor due to the presence of interface surface states and/or defects [19]. The Fermi level pinning describes a situation where the work function of the metal electrode is pinned to the work function of the semiconductor. Similar approach has

been applied to explain an origin of the open circuit potential of organic photovoltaic cells, based on conjugated polymer and fullerene derivatives. Brabec et al. [20–22] have found that the value of $V_{OC}$ in these cells is directly related to the energy difference of HOMO level of the donor and the LUMO level of the acceptor components. This electrode-insensitive voltage behavior was ascribed to the Fermi level pinning of the negative metal electrode to the reduction potential of fullerene via charged interfacial states. Thus, the $V_{OC}$ value in plastic solar cells is mainly related to the electronic structure of acceptor and may be tuned by molecular engineering. In addition, the value of $V_{OC}$ is also influenced by an interfacial factor associated with different morphology of composite films [23]. Moreover, the value of $V_{OC}$ in semiconductor–polymer hybrid cell may be influenced by the size of nanorod diameter, according to tendency of the increase of the bandgap energy with decrease of the nanostructure size.

## 2.2.2 Competitive processes in the hybrid systems

A flux of photo-generated charge carriers, responsible for the value of photocurrent may be diminished by several processes: (1) Recombination in the bulk, when the travel path of the excitons is longer than their diffusion length. Since the exciton diffusion lengths in various conjugated polymers ranges from 5 to 20 nm [24], the electron–hole recombination may be diminished by preparation of the bulk heterojunction solar cell with nanostructures well distributed in the polymer phase. (2) Back-transfer recombination, when the hole from the conducting polymer recombines at the interface with the electron from semiconductor [25]. This type of recombination is strongly influenced by unbalanced hole and electrons mobilities in corresponding materials. Since the electron mobility exceeds hole mobility by two orders of magnitude, the improvement of the hole transport mobility in the polymer should

significantly improve the PV cell performance [26]. The recombination is also strongly enhanced if the charge transport towards the electrodes is hindered by the domain boundaries between the electron donating and accepting materials [27], leading to a strongly morphology-dependent quantum efficiency of hybrid PV cell [28, 29].

## 2.3 Materials used in the photoactive layer

## 2.3.1 Conducting Polymers used in the photoactive layer

Conjugated polymers in the polymer–semiconductor hybrid systems can play both the role of photoactive materials as well as acceptor of holes. The electron transfer from conjugated polymers to the semiconductor phase may be detected by measurement of quenching of photoluminescence from conducting polymer after addition of semiconductor nanocrystals [30–32] or by photoinduced absorption experiments [33].

The chemical structures for polymers usually used in nanoparticle– polymer PV cells are shown in Figure 2.4. All of them are hydrophobic and have extensive conjugation. Table 1 gives parameters that are important from the viewpoint of PV cell performance. With the exception of PTAA, the polymers are used for photogeneration as well as charge transport. (PTAA has a relatively large $E_g$ value and is less suited for photogeneration.) P3HT is the most widely used semiconducting polymer for nanoparticle–polymer PVs due to very high value of the hole mobility and good processability.
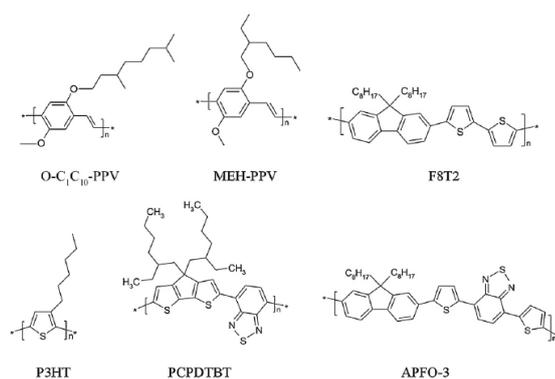
**Figure 2.4** Chemical structures of selected polymers commonly used in hybrid solar cells.

**Table 1** Selected parameters for conducting polymers used in hybrid polymer–semiconductor PV cells.

| Polymer | $E_{LUMO}$ (ev) | $E_{HUMO}$ (ev) | $E_g$ (ev) | Hole mobility ($cm_2V^{-1}s^{-1}$) | Ref |
|---------|-----------------|-----------------|------------|------------------------------------|-----|
| P3HT (NR) | -2.55 | -4.65 | 2.1 | $10^{-5}$ to $10^{-4}$ | 151 |
| P3HT (RR) | -3.0 | -4.90 | 1.9 | 0.05-0.1 | 155 |
| MEH-PPV | -2.9 | -5.3 | 2.4 | $10^{-4}$ to $10^{-3}$ | 156 |
| $OC_1C_{10}$-PPV | -3.0 | -5.26 | 2.86 | $10^{-6}$ | 158 |
| F8T2 | -3.1 | -5.5 | 2.4 | 0.01-0.02 | 143 |
| APFO-3 | -3.53 | -5.84 | 2.31 | $3.1x10^{-5}$ | 148 |

The characterisation of conjugated polymers used in nanoparticle–polymer PVs usually involves electrical property, structure and chain length measurements. The electrical properties are defined by the energy levels ($E_{HOMO}$, $E_{LUMO}$ and $E_g$) as well as the mobility. The position of the HOMO levels is important for the PCE of nanoparticle-polymer PVs as well as its stability to oxygen. The ionisation potential of a conjugated polymer directly affects $V_{OC}$ as well as the stability to air. Previous studies have shown that the ionisation potential should not be lower than [34] ca. 5.2 eV otherwise the polymers are susceptible to oxidation by $O_2$. Generally the ionisation potential of a polymer can be tailored by adding electron withdrawing or donating substituents to the main chain. An important factor taken into account in choosing the most preferable conducting polymer as the composite material for PV cell is the

14

position of the HOMO and LUMO energy levels with respect to the energy of conducting and valence bands of semiconductor. Because lowering of the $E_g$ allows moving the limit for absorption of photons, a significant increase of the number of excitons created under illumination may be achieved.

The hole and electron mobilities of polymers also affect PCE because high mobilities are essential within polymer-based PVs in order to minimize recombination losses. Mobilities of ca. $10^{-3}$ cm$^2$ V$^{-1}$ s$^{-1}$ are needed to prevent photocurrent losses for PV cells with thickness of several hundred nanometers. The mobility can be determined by applying a saturation regime equation to the measured I vs. V data [35]. The conducting polymers in the neutral state the typical values range from $10^{-1}$ to $10^{-7}$ cm$^2$ V$^{-1}$ s$^{-1}$ for holes [36, 37] and from $10^{-4}$ to $10^{-9}$ cm$^2$ V$^{-1}$ s$^{-1}$ for electrons [38, 39]. The charge transport in the conducting polymer may be enhanced by the increase of degree of polymer regioregularity (RR) by means of regioselective synthesis of the polymer [40–42]. This relationship has been widely studied for poly(3-alkylthiophenes) (PATs). For example, the hole mobility in the neutral regioregular PATs, with over 95% of head-to-tail couplings, ranges from $10^{-3}$ to $10^{-1}$ cm$^2$ V$^{-1}$ s$^{-1}$ [43–45] compared with $10^{-5}$ to $10^{-4}$ cm$^2$ V$^{-1}$ s$^{-1}$ in regiorandom analogues [46, 47]. This is because the HT coupling of the monomer units in RR polymer essentially favors a rod-like form, in contrast to more twisted chains in regiorandom polymer. In several reports [37, 48, 49] the high mobility of the charge carriers in RR polymers has been ascribed to the interchain π-π stacking, which results in delocalization of the charge carriers over the several neighboring chains. In effect, the charge carriers may easily hope between the chains giving rise to the higher mobility. According to Sirringhaus et al. [48] the interchain π-π stacking leads to the self-organization in P3HT film in a lamella structure with twodimensional conjugated sheets. In addition the mobility generally increases with molar mass because fewer

hopping events are required for films composed of longer chains.

The structure investigations involve chain packing and morphology. A combination of out-of-plane and in-plane grazing incidence XRD is well suited to study P3HT matrix structure [35]. The morphology of the films is usually studied by AFM and SEM. These studies have shown that within P3HT films the chains can form well-defined nanorods [35] when the molar mass was less than 4000 g mol$^{-1}$. A less ordered structure occurred at higher molar masses.


## 2.3.2 Inorganic Nanoparticles used in the photoactive layer

Conjugated polymer-semiconductor solar cells have been demonstrated in various semiconducting polymer blends containing CdSe [49-51], CdS [52], CuInS$_2$ [14], or PbS [53] nanocrystals. This strategy is promising for several reasons [54]: (1) Inorganic semiconductor materials can have high absorption coefficients and photoconductivity as many organic semiconductor materials. (2) The n- or p-type doping level of the nanocrystalline materials can easily be varied by synthetic routes so that charge transfer in composites of n- or p-type organic semiconducting materials with corresponding inorganic counterparts can be studied. (3) If the inorganic nanoparticles become smaller than the size of the exciton in the bulk semiconductor (typically about 10 nm), their electronic structure changes. The electronic and optical properties of such small particles depend not only on the material, of which they are composed but also on their size [15, 49, 55-57]. Band-gap tuning in inorganic nanoparticles with different nanoparticle sizes can be used for realization of device architectures, such as tandem solar cells in which the different bandgaps can be obtained by modifying only one chemical compound [58, 59]. A substantial interfacial area for charge separation is provided by nanocrystals, which have high surface area to volume ratios [51].

High surface tension of very small inorganic nanocrystals makes them unstable, and thus they have a tendency to grow to larger particles by a process called "Ostwald ripening" [60]. Therefore, nanoparticles are synthesized commonly shielded by an organic ligand. For example, nanocrystals of II–VI semiconductors such as CdS and CdSe can be prepared by chemical synthesis. One of the most popular method is pyrolysis of organometallic precursors ($Cd(CH_3)_2$, bis(trimethylsilyl)sulfide or bis(trimethylsilyl)selenium) in a mixture containing trioctylphosphine oxide (TOPO), tributhyl- or trioctylphosphine (TOP) and small amount of various phosphonic acids as a strong ligand for cadmium ions [3–5]. A high surface energy of the small-sized semiconductor crystals leads to their aggregation or oxidation. An organic layer surrounding the nanoparticle can prevent such processes and also ensures solubility of the nanocrystals in organic medium which is highly important for preparation of the nanoparticle–polymer blends. However, this organic ligand, on the other hand, is a barrier for transport of charges from nanoparticle to nanoparticle. Therefore, in the hybrid solar cells, such ligands have to be removed to ensure intimate electrical contact between the nanoparticles [56, 61].

The growth conditions and the shape of nanocrystals, from dots to 1D rods of different length (Figure 2.5 (a)–(d)) and to branched structures, may be optimized by manipulating the composition of the reaction solution, concentration of reagents, temperature, as well as the injection method [62–64]. Manna et al. [65] have demonstrated that the formation of CdSe nanocrystals with rod, arrow, snowflake and tetrapod shapes may be controlled by variation of the ratio of trioctylphosphine oxide and hexylphosphonic acid used for synthesis. Recently, Manna and co-workers [66] have reported a more general approach for synthesizing of tetrapod-shaped nanocrystals made of various combinations of II–VI semiconductors. This method, based on a seeded-growth process, allows varying independently the compositions of

the core and the arms of tetrapods. The nanoparticle geometry and aspect ratio (AR) have a strong influence on PCE. Nanoparticles with moderate aspect ratios generally increase the PCE for inorganic nanoparticle–polymer PV cells.
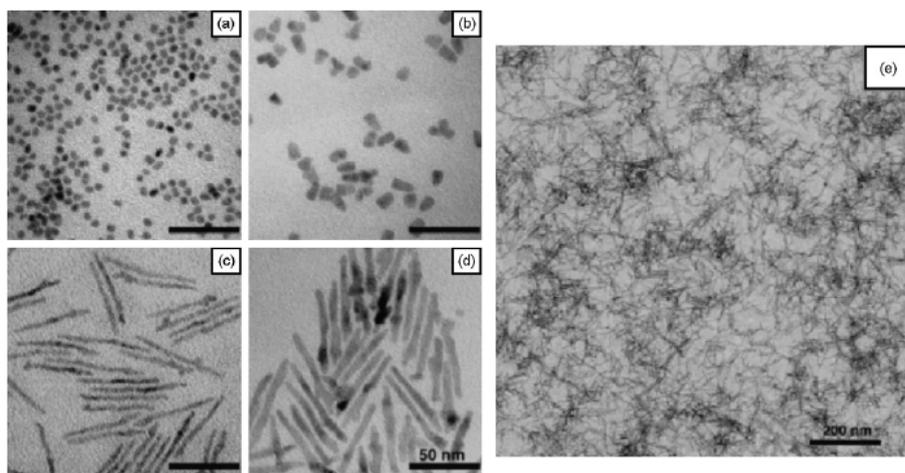


**Figure 2.5** TEM images of (a) 7 nm×7 nm, (b) 8 nm×13 nm, (c) 3 nm×60 nm, (d) 7 nm×60 nm CdSe nanocrystals and (e) TEM image of a film prepared from 40 wt% 3 nm×60 nm CdSe nanorods in P3HT, spin cast from the mixture of 10 vol% pyridine in chloroform. [69].

In general, the synthesis of CdS nanorods may be also performed by thermal decomposition of single-molecule precursor, $Cd(S_2CNEt_2)_2$, in the presence of hexadecylamine as surfactant [67]. The use of single precursor has an advantage of avoiding the toxic and explosive cadmium compounds and eliminating the undesired effects of additional ions during the synthesis. The shape and size of nanostructures may be controlled by temperature and precursor concentration. Thermal decomposition method has been also used for synthesis of TOPO-capped $CuInSe_2$ sharp-edged nanoparticles with dimensions of approximately 15nm by 20nm [68, 69]. There are also several other highly perspective methods of obtaining of semiconductor nanorods and/or more complex structures (tetrapods, arrows), like soft template methods (such as liquid crystal [70] and micellar [71–73]), structure-directing

18

coordinate solvent methods (such as solvothermal route [74–76]) and vapor–liquid–solid (VLS) [77] and solution–liquid–solid [78] methods.

The ligand used during synthesis of nanocrystals protects before aggregation of particles but on the other hand, it forms a barrier of several Angstrom thickness around the nanocrystals. Then, after blending with the conjugated polymer, the barrier of ligand may decrease the conversion efficiency of hybrid material by impeding the transport of the electrons between the adjacent nanocrystals [52] and between conducting polymer and nanocrystals. It has been found however, that the surface ligand can be changed without altering the intrinsic electronic properties of nanocrystal. Huynh et al. [64] have shown that the TOPO can be replaced by a weak-binding ligand, as pyridine, allowing also for a uniform distribution of CdSe nanocrystals in poly(3-hexylthiophene) film obtained by spin-coating from pyridine–chloroform solution (containing from 4 to 12 vol% of pyridine, see Figure 2.5 (e)). However, too much pyridine is not recommended to avoid precipitation of P3HT, which is soluble in chloroform but insoluble in pyridine. Moreover, pyridine may also act as non-radiative recombination site leading to decrease of the external quantum efficiency of the PV device and therefore, it should be removed from the hybrid layer by heating.


## 2.4 Methods of preparation of polymer-semiconductor solar cells

Hybrid polymer–inorganic structures can be prepared in different ways: (1) a planar bilayer structure where an organic layer is deposited on top of an inorganic semiconductor layer, (2) nanostructured porous structures where a connected semiconductor layer is filled with a conjugated polymer, and (3) blends of nanocrystals with polymer where semiconductor nanoparticles and polymer are deposited from the same solution. The inorganic semiconductors studied for hybrid

devices have included II–VI and I–III–VI compound semiconductors, which, critically, also offer optical absorption in the red part of the spectrum [52], and metal oxide semiconductors.

## 2.4.1 Bilayer heterojunctions

The easiest way is to prepare a bilayer heterojunction. In a bilayer heterojunction device, p-type and n-type semiconductors are sequentially stacked on top of each other, as shown in Figure 2.6. The semiconductor may be deposited chemically [79, 80] or electrochemically [81] on the transparent ITO and covered by drop-casting or spin-coating with the conducting polymer. However, due to relatively small area of interfacial surface, this type of hybrid systems is not perspective. The efficiency of bilayer solar cells is limited by the charge generation 5-15 nm (exciton diffuse length) around the donor-acceptor interface. Since a typical absorption depth in conducting polymer is about 100 nm, most of absorbed photons are lost due to recombination of the excitons created at the distance above the diffusion length.
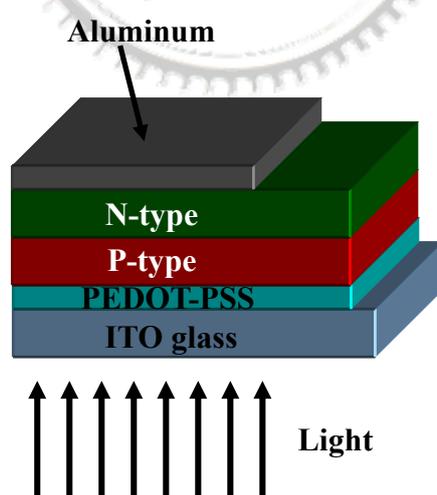


**Figure 2.6** Bilayer configuration in organic solar cells.

## 2.4.2 Bulk heterojunctions

The limitation in a bilayer heterojunction may be overcome by preparation a bulk heterojunction cell. Bulk heterojunction is a blend of the donor and acceptor components in a bulk volume (Figure 2.7). The both components are usually prepared separately, blended in organic solvent and then grafted on the substrate. The blend exhibits a donor-acceptor phase separation in a 5-15 nm length scale. In such a nanoscale interpenetrating network, each interface is within a distance less than the exciton diffusion length from the absorbing site. The bulk heterojunction concept has heavily increased (orders of magnitude) the interfacial area between the donor and acceptor phases and resulted in improved efficiency solar cells [82]. Meanwhile, separated charges require percolated pathways for the hole and electron transporting phases to the contacts. In other words, the donor and acceptor phases have to form a nanoscale, bicontinuous, and interpenetrating network [83]. Therefore, the bulk heterojunction devices are much more sensitive to the nanoscale morphology in the blend. Optimal morphology is achieved by a careful balance between the nanoparticle aggregation needed for good charge transport and phase separation needed for efficient exciton dissociation. Wang et al. [84] have postulated that the capped pyridine molecules at the CdS surface facilitate dissolution of CdS nanocrystals in the pyridine solvent. Moreover, pyridine acts as a surfactant which improves compatibility of CdS nanocrystals with the polymer chains (MEH-PPV) both in the solution and in the solid film. Homogeneous dispersion of nanoparticles in the polymer blends leads to the larger area of donor–acceptor interface which could improve the charge separation efficiency.
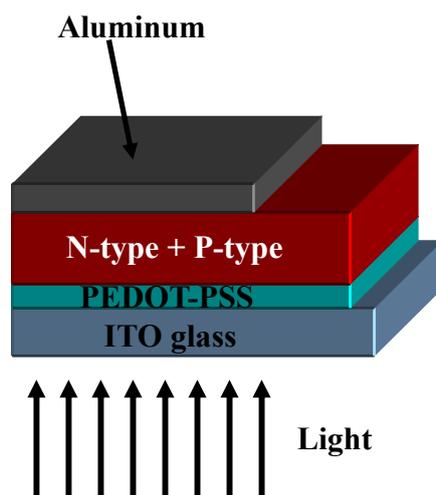
**Figure 2.7** Bulk heterojunction configuration in organic solar cells.

The performance of photovoltaic devices may be also controlled by changing the size, shape and concentration of nanocrystals. The influence of semiconductor nanoparticle content on the efficiency of PV hybrid cell has been studied by Greenham at al. [52]. It has been shown that at low concentrations of spherical 5 nm CdSe nanoparticles in MEH-PPV only part of electrons have a continuous pathway to the external circuit. At higher concentrations (65 wt%) the nanocrystals begin to form a connected network and both components provide continuous ways for the charge carriers to the electrodes. The highest EQE (12%) was obtained at 90 wt% of CdSe. However, even at the optimum concentration, the EQE is still low due to trapping of the electrons at "dead ends" in the nanocrystal network. Therefore, the much effort was focused on preparation of the hybrid cells containing nanorods or branched semiconductor structures.

It has demonstrated that one-dimensional nanorods [50, 64] or branched semiconductors [85–89] are used to create the percolation networks in the polymer/semiconductor blend improving the charge transport through the semiconductor phase to the electrode. Huynh at al. [50, 64] have demonstrated that change of the aspect ratio of CdSe nanocrystals from 1 to 10 results in the increase of

the external quantum efficiency at the wavelength of 500 nm from about 18% to 54%, respectively (Figure 2.8). By contrast, the cells containing hyperbranched CdSe approached maximum PCE values at lower nanoparticle concentration values than the other nanoparticle geometries [85]. Gur et al. [85] argued this was because of more efficient formation of charge transfer pathways. Furthermore, the cells based on hyperbranched particles revealed near-linear rise of $J_{SC}$ and power conversion efficiency with increased loading of CdSe, also at a low content of nanostructures. This suggests that single incorporated hyperbranched particle can contribute independently to the output of the cell [85].

In another paper Gur et al. have shown that a unique tetragonal structure of CdTe nanocrystals gives rise to a natural ordering in the deposited films [90, 91]. Namely, three arms of each tetrapod contact the substrate at its base, while the fourth arm points up, perpendicular to the substrate. This ordering remains in the composite films created by spin-coating of the polymer–nanocrystal mixture. However, the efficiency of the device based on CdTe tetrapods and P3HT spin cast from chloroform solution are still low (less than 1%), suggesting the need of further improvement by optimization of device composition and morphology [90].
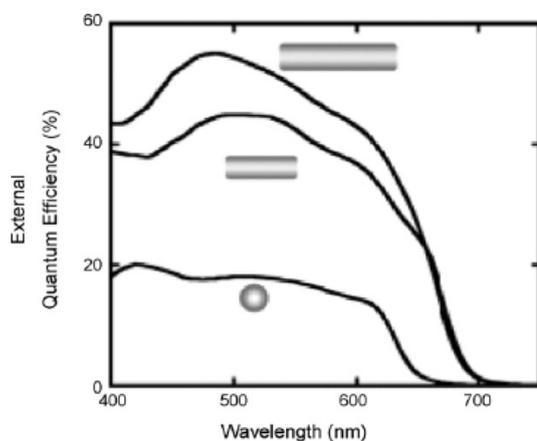


**Figure 2.8** Influence of the increasing length (7, 30 and 60 nm) of 7-nm diameter CdSe nanorods on the external quantum efficiency of CdSe (90 wt%)/P3HT 200-nm thick solar cell. [50]

23

One of the major difficulties in preparation of the bulk heterojunction cell is the phase segregation of organic and inorganic phases. The key parameters are processing conditions as the type of the solvents used for preparation of the polymer/semiconductor mixture and temperature which control the rate of drying of the hybrid system. The influence of the rate of solvent evaporation on the formation of the π-stacked aggregates and in consequence, on the charge carrier mobility, has been also confirmed [92–94]. Yang et al. [94] have shown that drop-casting of P3HT reinforces the lamellar π-π stacking perpendicular to the substrate, depending on the type of solvent. The charge mobility in the film decreases in the order $CHCl_3$ > THF > toluene > $CH_2Cl_2$. The significantly lower charge mobility in the films deposited from toluene and dichloromethane was attributed to the formation of distinct grain boundaries and the short nanorod-like structures. In contrast, the polymer chains cast from $CHCl_3$ form highly interconnected nanofibrillar networks without grain boundaries providing fast charge transport through the film.

Solvent evaporation causes a transition from a one phase to a two phase region. Extensive nanoparticle aggregation and phase separation of the polymer phase is favored as nanoparticle and polymer volume fraction increase. In well-controlled solvent evaporation processes this gives a bicontinuous solid dispersion. It is in this way that non-equilibrium morphologies can be frozen (kinetically trapped) into the photoactive layers of nanoparticle–polymer PV cells.

Phase segregation during casting may lead to formation of "dead ends" and isolated domains trapping the charge carriers. The polymer wetting and charge transfer dynamics may be improved by means of interface modifiers. One option is to use a surfactant containing the head group of a high affinity to semiconductor and the end group providing solubility in the chosen solvent. Milliron et al. [95] have

demonstrated that pentathiophene phosphonic acid (T5-PA), served as a complexing agent with respect to the CdSe nanocrystals, could be used as a third component in nanocrystal–polymer devices mediating the charge transport between these two materials.

Alternative approach applied by Liu et al. [96] consisted in functionalization of the polymer chain ends with amine groups, which are strongly adsorbed onto CdSe nanoparticles. The endamino groups attached to the P3HT replace the pyridine surfactant on the surface of nanorods and thereby enhance the miscibility of the polymer with the nanocrystals and improve the power conversion efficiency of hybrid device. The ligand-exchange method has been also applied to graft the carbodithioate-containing oligo- and polythiophenes on the CdSe surface [97].

Another strategy, which utilizes direct attachment of P3HT onto the CdSe nanorod surface, has been applied by Zhang et al. [98] by coupling of vinylterminated P3HT to arylbromide-functionalized CdSe. The recent advances in preparation the organic–inorganic nanohybrids through tailoring of semiconductor nanocrystals with conjugated polymers have been discussed by Lin in the review paper [99].

An efficient way of impeding the phase segregation is also to induce strong interaction between organic–inorganic components through molecular recognition phenomena. This concept has been successfully used by De Girolamo et al. [100] in preparation of the composites of diamino-pyrimidine functionalized P3HT with thymine-capped CdSe nanocrystals. This molecular processing method has been also exploited for the alternating deposition of thymine-capped nanocrystals and functionalized polymer monolayers by layer-by-layer assembly [101].

Thermal treatment of the polymer in the vicinity of its melting temperature ($T_m$) was proven to be an effective method to increase the hole transport velocity due to enhanced chain ordering ($\pi$-stacking) [102,103] and self-organization of the polymer

[64]. According to Wang et al. [84], improvement of the device performance after annealing is mainly attributed to reorganization of the inorganic nanocrystal/polymer interface, leading to the increase of exciton dissociation efficiency and reduction of the recombination loses. It may be also a result of reduced interface defects [104] and improved phase-structured morphology [105]. Dittmer et al. [106] have postulated that annealing of hybrid system promotes the equilibrium morphology of a spin-coated film, improves crystallinity within the phase-separated networks and thereby facilitates the charge transport to the electrodes. Thermally induced crystallization enhances also of the efficiency of the charge transport across the interface between the bulk of material and the collecting electrode ($\eta_{tr}$). Most of the reports in the literature on the influence of annealing on the efficiency of hybrid cells concern the polymer/PCBM systems but the mechanism of performance enhancement for the polymer/inorganic semiconductor hybrid systems is less clear.

## 2.4.3 Porous and Vertically ordered semiconductor–polymer systems

There are also several attempts to prepare the PV cells on the base of nanostructured large-band gap semiconductors. This approach was used to combine $TiO_2$ with conjugated polymer [107-109] because $TiO_2$ can be easily obtained in the form of mesoporous material [110] providing the continuous network for electron transport. In PV cell developed by Coakley and McGehee [107] the conducting polymer (P3HT), acting as solid-state sensitizer, was infiltrated into 100nm thick mesoporous $TiO_2$ film. The external quantum efficiency was about 10%, whereas the power conversion efficiency under monochromatic illumination (at 514 nm) was1.5%. A shortcoming of this type of the cell is poor polymer penetration in the porous structure, small interfacial area, slow transport of the holes generated in the polymer in a distance longer than 10–20 nm from the top of the film and back recombination with the

electrons from $TiO_2$.

The photovoltaic performance of the devices may be improved by structuring one of the components into vertically ordered rods or pores with a diameter less than the exciton diffusion length, as displayed in Figure 2.9. The two phases have to be interdigitated in percolated highways to ensure high mobility charge carrier transport with reduced recombination. Last but not least, a pure donor phase at the hole collecting electrode and a pure acceptor phase at the electron collecting electrodes have to be placed. This minimizes the losses by recombination of the wrong sign of charges at the wrong electrode, as well as acting as diffusion barriers for the wrong sign charge carriers at the respective electrodes. Ordered heterojunctions are generally made by infiltrating polymers into vertically aligned oxides, such as nanorods and nanotubes. Nanostructured $TiO_2$ or ZnO is an attractive approach to develop extremely efficient organic photovoltaics. They are abundant, nontoxic, and has been well-studied by the dye-sensitized solar cell community.

An alternative approach for vertical alignment is single-crystal nanorod arrays of other semiconductors (CdS, CdSe). They have been obtained by electrochemical synthesis using a hard template of anodic aluminum oxide (AAO) [111–116]. Kang and Kim [153] have applied such a matrix to construct the heterojunction solar cells with vertically aligned CdS nanorods and pores filled in with MEH-PPV.

The nanostructure in Figure 2.9 is considered ideal because it has small, straight pores and is thick enough to absorb most of the sunlight. The pore radius should be slightly less than the exciton diffusion length to enable maximum exciton harvesting. The thickness of the nanostructure should be 300–500 nm so that the infiltrated polymer can absorb most of the incident light. The pores (or channels) should be straight to provide the most direct path to the anode and cathode.
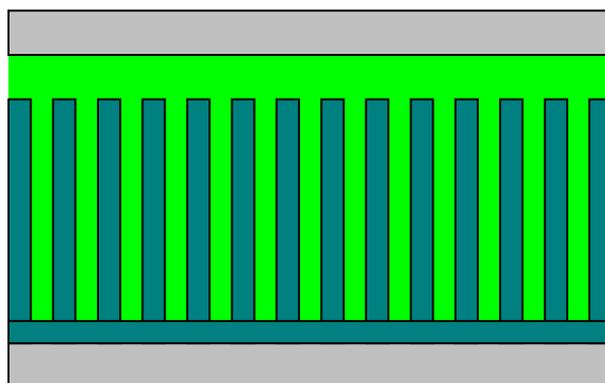
**Figure 2.9** Scheme of polymer–inorganic semiconductor hybrid system with vertically aligned semiconductor nanostructures.

Currently, the most efficient ordered nanostructured oxide/polymer device is significantly worse than bulk heterojunctions PV. It should be born in mind, which the procedure of preparation of vertically aligned nanorods with infiltrated polymer meets many difficulties in synthesizing the semiconductor arrays with suitable inter-rod spacing and infiltrating the non-polar conjugated polymer into the channels. Although there are a variety of methods (i.e. melt infiltration, dip-coating, and polymerization) used to fill pores, a high viscosity of the concentrated solution of conducting polymer and low wettability of the semiconductor surface leads to formation of the gaps between the two phases, impeding the interfacial charge transfer. Furthermore, the polymer mobility, which is crucial in determining fill factor and $J_{SC}$ in semicrystalline polymers, can be reduced inside small pores (~10 nm). There is no general rule to understand the effects of pore size on the mobility of a given polymer, because hole transport is dependent on the specific microstructure of the polymer film. It has been shown that only 68% of excitons are split at the titania/polymer interface inside mesoporous films [118], possibly because of reduced exciton diffusivity and

imperfect exciton quenching. Fortunately, the nanostructured oxide surface can be modified using dyes, carboxylic, and phosphoric acid groups, which have the potential to improve polymer wetting and charge transfer dynamics. Using interface modifiers, it is possible to completely quench excitons at the $TiO_2$/polymer interface [119, 120].

# Chapter 3

# Experimental Section

## 3.1 Characterization

The surface morphology were observed by field emission scanning electron microscopy (FE-SEM). JEOL-6500 system was employed in this study. The transmission electron microscopy (TEM; JEOL 2100) operated at 200 kV was used for detail crystal analysis. Samples for the TEM were prepared by depositing a drop of the samples in appropriate solvent onto a carbon grid and the grid was dried in air. The crystal structures were investigated by X-ray diffraction (Siemens, D5000) using Cu K$\alpha$ radiation ($\lambda$=0.15405 nm) (40 kv, 200 mA) and a nickel filter at scanning rate of $5^{o}$/min. When an x-ray beam strikes a crystal surface at some angle, a portion is scatted by the layer of atoms at the surface. For optical properties of ZnO nanorods, photoluminescence measurement was performed by the excitation from 325 nm *He–Cd* laser at room temperature. Fourier Transfer Infrared Spectrophotometer (FTIR, PerkinElmer Spectrum 100 spectrometer) was used to identify the chemical structure of materials. Reaction solution was dropped on KBr plate for analysis. Optical properties were analyzed by UV-vis spectroscopy and fluorescence spectrometer (Hitachi F4500) equipped with an excitation source of 450 nm wavelength. Differential scanning calorimetry (DSC) curves for P3HT and the two different P3HT/CdS nannorod were obtained with a TAQ2000 DSC. Approximately 4mg of each sample was loaded in an aluminum pan. The analyses were conducted from -10 °C to 230 °C at heating and cooling rates of 20 °C /min and a nitrogen flow rate of

5 mL/min. ^{1}HNMR spectra of the blend solutions were recorded using VARIAN 500 MHz. Chemical shifts are referred to tetramethylsilane for [1]H. All NMR spectra measurement was done in $CDCl_3$ at room temperature. Power efficiency measurements under approximately AM1.5G conditions (100 $mW/cm^2$) were performed using a xenon lamp-based Newport 91160 W solar simulator. J-V characteristics were measured using a Keithley 2400 electrometer. A Si photodiode (Hamamatsu S1133) was used to check the uniformity of the area exposed. The spectrum of the solar simulator was calibrated using a PV measurement (PVM-154) mono-Si solar cell (NREL calibrated). Reported efficiencies are obtained from an average value of four measurements from a set of four regions on each substrate. These data points are representative of the defect-free device performance and reflect the generally observed trend.

## 3.2 Material Fabrication

### 3.2.1 Chemical growth of ZnO nanorods

A ZnO buffered layer was deposited on substrate by radio frequency (rf) magnetron sputtering using 99.99% ZnO as the target. The ZnO nanorods were grown on the substrate. The ZnO-coated substrates were placed in a solution containing an equimolar (0.02M) aqueous solution of $Zn(NO_3)_2.6H_2O$ and Hexamethylenetetramine (HMT) and reacted at 75 °C for 30-300 min. After that, the substrates were removed from the aqueous solutions, rinsed with distilled water, and dried at room temperature overnight. A nanorod substrate was baked at 400 °C for 30 minutes. Finally, high quality one-dimensional ZnO nanostructures were developed.

### 3.2.2 MgO Coating on ZnO nanorods and annealing treatments

The ZnO nanorods were immersed into $Mg(CH_3COO)_2$ aqueous solution. The

solution was then stirred gently for about 30 min and then an aqueous solution of 0.03M $Na_2CO_3$ was dropped into the solution at the rate of 2.5 $cm^3$ $min^{-1}$ and mixed for another 270 min. At the end, after washed with alcohol, dried at 80 °C for 3 h, and then fired at 350 °C for 0.5 h in Ar atmosphere, the as-made MgO-coated ZnO nanorods were obtained. The coated nanorods were then immediately placed in a furnace preheated to 600-900 °C and annealed for 30 min in $O_2$ and $H_2/N_2$ (5%/95%) atmospheres.

### 3.2.3 Synthesis of CdS QDs and attachment of CdS QDs on ZnO nanorods

CdS QDs were prepared via a literature method [121]. Typically, CdS nanocrystals were synthesized in octadecene (ODE) solution with oleic acid (OA) as a capping agent. In a typical experiment, CdO (0.20 mmol), OA (3 mmol), and ODE (8.92 ml) were mixed in a three-necked flask and heated to 300 °C for 10 min under vigorous stirring and a flow of argon. S powder (0.1 mmol) was dissolved in ODE (2.5 ml) by ultrasonic treatment and then swiftly injected into the reaction flask. The reaction temperature was kept at 250 °C for the subsequent growth process. The unconsumed cadmium precursor was separated from the nanocrystals by the repeated extraction of the reaction aliquots with an equal volume of $CHCl_3/CH_3OH$ (1:1). After the extracting process was applied twice, the CdS nanocrystals could be obtained by adding acetone.

The ITO/ZnO nanorods were immersed in a 1 M mercaptopropionic acid (MPA) + 0.01 M sulfuric acid acetonitrile solution for 24 h and then rinsed thoroughly with acetonitrile and toluene. After that, the ITO/ZnO nanorods were transferred to the CdS QD solution to ensure saturated adsorption of the QD onto the ZnO nanorods.

**3.2.4 Synthesis of CdS-P3HT composites**

In a three-neck round bottom flask equipped with a magnetic stirring bar and condenser, 8 ml of dichlorobenzene (DCB), 4 ml of dimethyl sulfoxide (DMSO), 0.01 g cadmium acetate dihydrate and 0.01 g of P3HT (regioregular, Mn=30000~60000) were heated to 100 °C and degassed with nitrogen for 30 min. In a second vial, 0.002 g of sulfur was dissolved in 1mL of anhydrous DCB. Both solutions were heated to the temperature of the reaction (between 120–180 °C) depending on the composite. Then, 1ml of the sulfur solution was then injected swiftly into the cadmium precursor solution. The solution was allowed to react for 30 min. The mixture of CdS and conducting polymer was purified by removing any cadmium, sulfur ions and DMSO via adding anhydrous methanol to form precipitate. After centrifugation, the supernatant was then removed and the composite dissolved in DCB.

**3.2.5 F-doped SnO$_2$ deposition on ZnO nanorods**

To deposit the FTO films on ZnO nanorods by ultrasonic spray pyrolysis, the initial solution was prepared from 0.5 moles of stannous chloride in 1.0 L of deionized water. In order to promote solubility, 5% HCl was added into the stannous chloride precursor solution. Upon stirring, the solution immediately became transparent, indicating its solubilization. Finally, a 50% ammonium fluoride precursor was mixed at room temperature and stirred for 5 min. The deposition temperature was set at 400 °C for all of the depositions, and the deposition time was 0.5-3 min. The carrier gas flow rate was maintained at 20 L/min in air.

**3.2.6 Fabrication of solar cells**

Bulk heterojunction: The indium tin oxide (ITO) coated glass was purchased from Merck and resistivity is 10 ohms/sq. The ITO-coated glass was pre-cleaned (DI water,

acetone, ethanol and isopropyl alcohol) and treated with oxygen plasma prior to use. PEDOT:PSS layer (50 nm) was spin-coated at 2000 rpm and annealed at 120 ºC for 30 min. The CdS/P3HT layers (200 nm) were spin-coated from their corresponding dichlorobenzene solutions (30 mg/mL) at 1500 rpm and annealed at 160 °C for 60 min, followed by thermal evaporation of an aluminum electrode. Al top electrodes (100 nm) were deposited by thermal evaporation through a shadow mask, resulting in individual devices with 0.1 cm$^2$ nominal area.

Ordered heterojunction: The indium tin oxide (ITO) coated glass was purchased from Merck and resistivity is 10 ohms/sq. The ITO-coated glass was pre-cleaned (DI water, acetone, ethanol and isopropyl alcohol) and treated with oxygen plasma prior to use. The ZnO nanorods were grown on the substrate, as mentioned above (Chapter 3.2.1). The CdS/P3HT layers (200 nm) were spin-coated from their corresponding dichlorobenzene solutions (30 mg/mL) at 1500 rpm and annealed at 160 °C for 60 min. The PEDOT:PSS layer (50 nm) was spin-coated at 2000 rpm, followed by thermal evaporation of an Au electrode.

# Chapter 4

# Fabrication and characterization of MgO-doped ZnO

# nanorod arrays

## 4.1 Introduction

Research on ZnO has generated great interests for its potential applications in photonics, especially on short wavelength light-emitting, UV lasing and transparent conducting materials due to its wide direct gap of 3.37 eV, large exciton binding energy of 60 meV at room temperature and its promising versatile applications [122]. Recently, doped ZnO are of technological importance because of their great potential for applications, such as transparent conducting electrodes [123].

Alloying ZnO with MgO makes ZnMgO a potential candidate for future optoelectronic devices because of its wide band gap, less lattice mismatch with ZnO as the ionic radius of $Mg^{2+}$ and $Zn^{2+}$ are similar [124, 125]. The band gap of the MgZnO alloys could be expanded from 3.3 to 4.20 eV and the microstructure and PL property of MgO–ZnO mixture have also been studied by several groups [126, 127]. In these works, this alloy produced a stronger UV luminescence at room temperature that was found to be excitonic in nature. These recent developments open up enormous interest in this materials system.

Recently, single-crystal ZnO nanorods have drawn considerable interests as building blocks or basic units for the fabrication of nanosized devices due to their wide band gap and a large exciton binding energy with high crystalline quality. In

order to realize ZnMgO-based electronic and optoelectronic devices [128, 129], band gap engineering of the nanorods would be prerequisite and many researchers have reported the technologies by incorporating MgO into ZnO. However, few studies have been investigated into ZnO-MgO core-shell nanorods grown by coating MgO nanoparticles on the surface of ZnO nanorods using wet-chemical solution process. Therefore, in this work, a simple method was used to fabricate MgO-coated ZnO nanorods and a rapid post-annealing was performed to investigate the effect of thermal treatment on the surface microstructure and luminescent properties of MgO-coated ZnO heterostructured nanorods.

## 4.2 Surface morphologies after annealing treatments

Figure 4.1 shows the scanning electron microscopy (SEM) images taken from several samples with highly uniform and densely packed arrays of ZnO nanorods and MgO-coated ZnO nanorods grown on Si substrate. Figure 4.1(a) and 4.1(b) illustrate as-grown ZnO nanorods and MgO-coated ZnO nanorods. It can be observed that MgO nanoparticles have been successfully deposited on the surface of the ZnO nanorods. After annealed at 900 °C in $O_2$ atmosphere, Figure 4.1(c) shows the MgO-coated ZnO nanorods still kept hexagonal shape and the morphology of ZnO nanorods remained almost unchanged as compared to that of the as-grown ZnO nanorods. However, it was noted that the surface of the MgO-coated ZnO nanorods annealed at 900 ºC in $O_2$ atmosphere was flattened and became rather smooth. In contrast, as annealed at 800 °C in $H_2/N_2$, it was observed in Figure 4.1(d) that some of the MgO-coated ZnO nanorods are slightly collapsed, probably because $H_2/N_2$ reduction atmosphere caused surface etching [130].
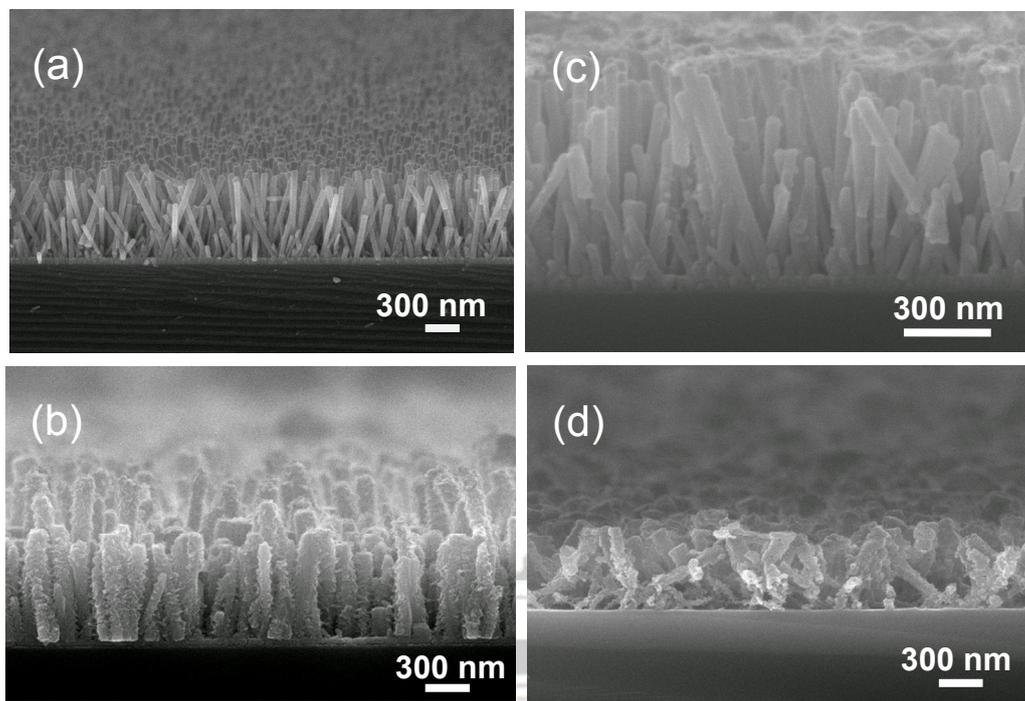
**Figure 4.1** SEM images of (a) ZnO nanorods, (b) as-made MgO-coated ZnO nanorods, and annealed MgO-coated ZnO nanorods at (c) 900 °C in $O_2$, and (d) 800 °C in $H_2/N_2$.

Figure 4.2(a) shows the X-ray diffraction (XRD) patterns of as-made and annealed MgO-coated ZnO nanorods. A weak (200) peak characteristic of the cubic MgO phase was detected for the as-made sample as confirmed to the XRD pattern of the MgO precursor in the inset of Figure 4.2(a) which is obtained at 350 ºC. In contrast, as the MgO-coated ZnO nanorods were annealed at 900 ℃ in $O_2$ or 800 °C in $N_2$-$H_2$ atmosheres, no MgO phase can be detected from the XRD patterns, indicating an interaction occurred in between ZnO and MgO. It is known that ZnO and MgO react easily to form MgZnO alloys at annealing temperatures higher than 700 °C [131]. In addition, it was also found that the ZnO (0 0 2) diffraction peak of the as-made and the annealed samples (in $O_2$) is located at 34.46° and 34.52°, respectively. It is thought that $Zn^{2+}$ ions in the ZnO lattice were replaced partly by $Mg^{2+}$ ions with

37

smaller radium, resulting in the decrease of the lattice constant along the c-plane [132]. According to the phase diagram [133], the thermodynamic solid solubility limit of MgO in ZnO was less than 4 mol%. Within the range of MgO 4 mol%, the MgZnO had a hexagonal phase similar to that of ZnO. Therefore, it can be deduced that MgZnO was probably formed.
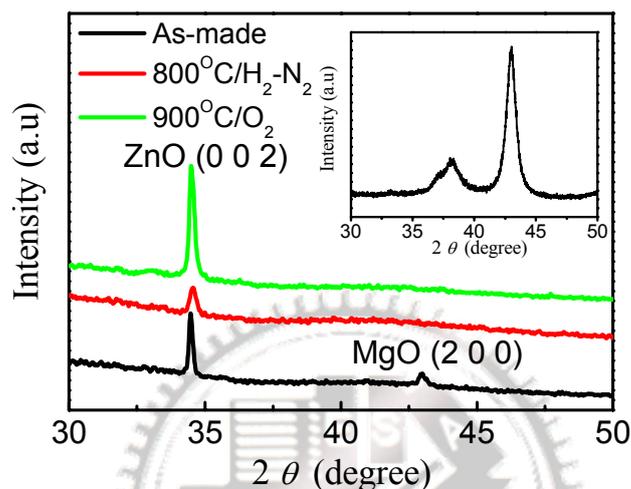


**Figure 4.2** XRD patterns of the MgO-coated ZnO nanorods annealed in various atmospheres. The inset is the XRD pattern of MgO precursor annealed at 350 °C.

It was postulated that during the process of hydrolysis, OH$^-$ could react with Mg$^{2+}$, leading to MgO nanoparticles adhering better on the surface of ZnO nanorods [134], as shown in Figure 4.3(a). After thermal treatment at 800 ºC in O$_2$ atmosphere, hetrostructured core (ZnO)-shell (Mg compound) nanorods were observed as evidenced from transmission electron microscopy (TEM) image in Figure 4.3(b). The diameter of the core (ZnO nanorods) and the shell (MgO$_x$) thin layer is about 70 nm and 7 nm, respectively. High resolution transmission electron microscopy (HRTEM) image of the MgO-coated ZnO nanorods in Figure 4.3(c) shows the (002) lattice fringe of the ZnO nanorod core and an amorphous layer can be identified in shell-MgO$_x$ thin layer, implying the diffusion of Mg into the ZnO nanorods during MgZnO alloy formation. Furthermore, the HRTEM image in Figure 4.3(d) obtained

from 900 °C annealing sample demonstrated that no significant amorphous $MgO_x$ was observable and the lattice fringes do notshow obvious distortions due to the small difference between the ionic radius of $Mg^{2+}$ and $Zn^{2+}$.
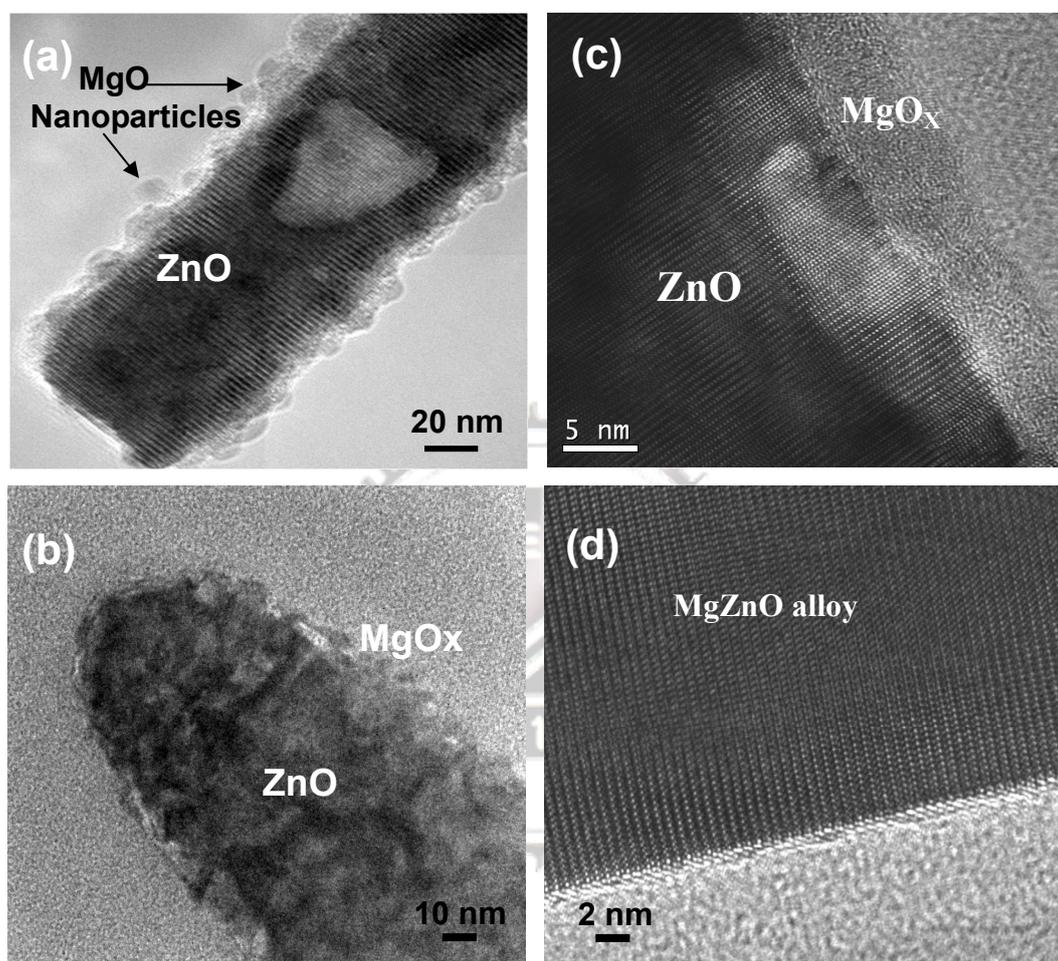


**Figure 4.3** TEM image of (a) as-made MgO nanoparticles on the surface of ZnO nanorods. (b) Low-magnification TEM and (c) HRTEM of annealed MgO-coated ZnO nanorod at 800 °C in $O_2$ atmosphere and (d) HRTEM image of 900 °C -annealed MgZnO alloy nanorod

## 4.3 Annealing effect on photoluminescence

Figure 4.4 illustrates the room-temperature photoluminescence (PL) properties of ZnO and MgO-doped ZnO nanorods. The ultraviolet (UV) emission peak of ZnO is generally attributed to the exciton-related activity, and the deep level emission generally results from structural defects, single ionized vacancies, and impurities

[135].When the MgO-coated ZnO nanorods were annealed above 800 °C in $O_2$ atmosphere, a blue shift of the near-band-edge emission was observed in Figure 4.4(a) due to the formation of MgZnO alloy. These results are in reasonable agreement with the thermal diffusion of Mg atoms at the MgO/ZnO heterointerface with the formation of MgZnO alloys [136].

The UV emission peaks at 371 and 367 nm for the samples annealed at 800 °C and 900 °C, respectively, are attributed to the increased substitution ratio of Mg on Zn sites and the band gap energy. Furthermore, an enhancement of the near band edge emission is achieved by annealing MgO–ZnO mixture in oxygen due to the reduction of structure defects.[6] In addition, it was also found that the blue shift of the near-band-edge emission for the MgO-coated ZnO nanorods annealed in $H_2/N_2$ atmosphere above 700 °C, as shown in Figure 4.4(b). Moreover, with an increase of the temperature of annealing up to 800 °C, a blue band peaked at 454 nm was observed. It indicates that MgO diffusion process may produce a new luminescent center to emit the blue emission in $H_2/N_2$ reduction atmosphere. However, the explanation on the blue emission produced by annealing the sample at 800 °C in $H_2/N_2$ is still not fully understood at present.
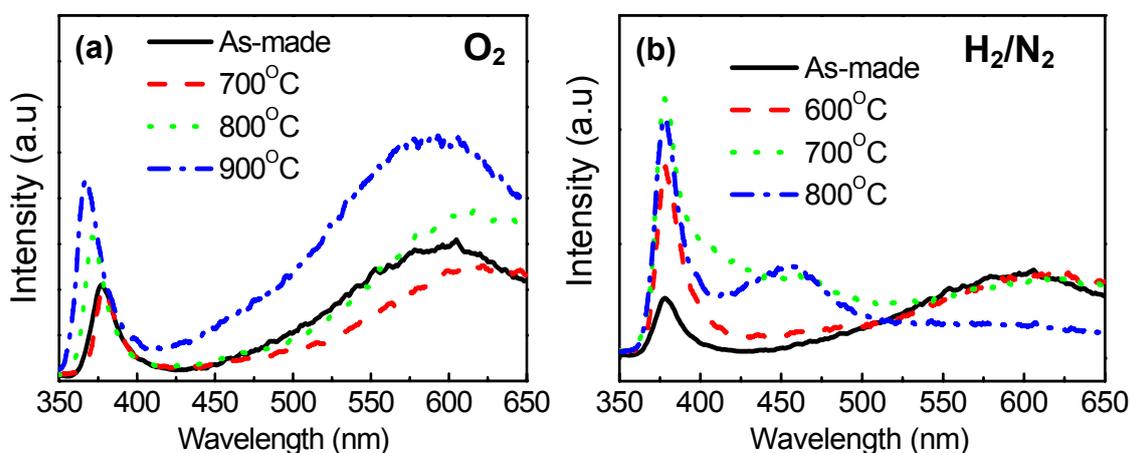


**Figure 4.4** Room-temperature PL spectra of ZnO nanorods annealed at various temperatures in (a) $O_2$, (b) $H_2/N_2$ atmospheres.

## 4.4 Summary

The microstructure and photoluminescent properties of MgO-coated ZnO nanorods prepared by solution techniques are investigated. The samples annealed at 700– 900 °C show well crystalline wurtzite structure of the ZnO nanorods. Annealing at high temperatures (>700 °C) in $O_2$ atmospheres leads to Mg diffusion in ZnO and MgZnO alloy formation. The room-temperature UV emission of the ZnO nanorods enhances with the increase of annealing temperature due to the reduction of structure defects. Furthermore, a blue shift in the near-band-edge emission was observed as a result of the alloy band gap widening. Moreover, it is noted that the visible emission from the MgO-doped ZnO nanorods annealed at 800 °C in $H_2/N_2$ is centered at about 454 nm. In contrast, the visible emission from the MgZnO nanorods annealed $O_2$ is at 595 nm.
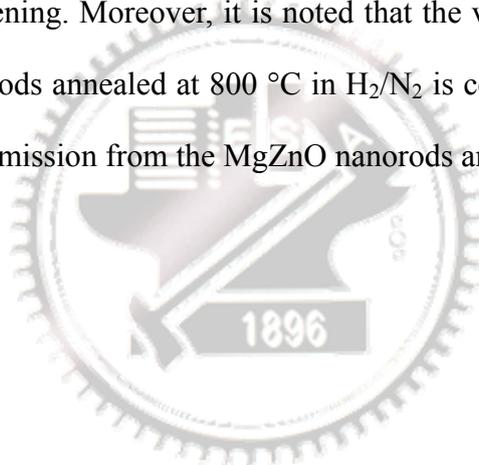
# Chapter 5

# Improvement of charge injection in nanostructured ZnO/P3HT hybrid solar cells

## 5.1 Introduction

Recently, organic-inorganic hybrid solar cells have attracted a great deal of interest recently due to their potential application in developing low-cost, large-area, mechanically flexible photovoltaic devices [50]. In organic-inorganic hybrid solar cells with planar junctions, the power conversion efficiency (PCE) is limited because the exciton diffusion length of the donor material is typically significantly shorter than its absorption length, resulting in recombining easily. In order to overcome this problem, a bulk heterojunction structure has been developed for organic-inorganic hybrid solar cells. Inorganic nanocrystalline materials can be used as alternative electron acceptors $TiO_2$ and ZnO nanocrystals [87, 102], or photo-absorption such as CdSe quantum dots [87, 137], which may be dispersed in solution together with the organic donor to form QDs-decorated ZnO-based hybrid solar cell. Several theoretical studies conclude that the ideal polymer-inorganic device topology is a perfect vertical array of single-crystal nanorods of the appropriate dimensions and pitch, encased in a film of the polymer [138]. A key advantage of using a vertical array of single-crystal nanorods as electron acceptors is that it provides direct channels for electron and hole transport to the electrodes. Besides, Electron transport in crystalline wires is expected to be several orders of magnitude faster than percolation through a random

polycrystalline network. In addition, QDs can provide the ability to match the solar spectrum better by tuning their particle size.

Organic-inorganic hybrid solar cells convert sunlight to electrical power by splitting photogenerated excitons across an interface between an electron donor and an electron acceptor material [139]. Hence, the study on the interface engineering is essential toward improving excitonic solar cells performance. Recently there are some reports on improvement in the photocurrent by the chemical modification with ruthenium dyes [140], carboxylic, and phosphoric acid groups [120], which have the potential to improve polymer wetting and charge transfer dynamics. Generally, interface modifiers are known to passivate inorganic surface states by chemically interacting with surface dangling bonds [141]. However, the mechanism for the improvement by the chemical modification is poorly understood. Therefore, in this study, the ZnO nanorods were directly decorated with CdS quantum dots and the surface energetic was changed by using different-sized quantum dots (QDs) to investigate the effect of energy level of QDs on the charge injection efficiency. In this study, ZnO nanorods were directly decorated with CdS quantum dots and the energy level by controlling the size of CdS quantum dots. It is demonstrated that the photovoltaic efficiency of the ZnO nanorods/P3HT solar cells can be improved 4-fold by decorating the nanorod arrays with CdS QDs.

## 5.2 Optical properties of CdS QDs

Figure 5.1 shows the absorption spectra of the three different-sized CdS QDs employed in the present study. These particles exhibit absorption in the UV or visible with an onset corresponding to particle size. The shift of the onset absorption to lower wavelengths with decreasing particle size represents size quantization effects in these particles. By comparing the excitonic transition (361, 404, 435 nm) to the absorption

curve reported by Yu and co-workers [121], the particle mean diameter of these samples was estimated as 2.2, 3.2 and 4.6 nm respectively. These different-sized QDs would be then deposited on ZnO nanorods for spectroscopic and photovoltaic investigation.
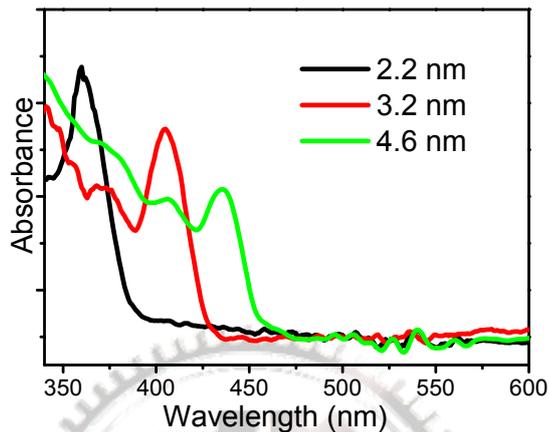


**Figure 5.1** Absorption spectra of 2.2, 3.2, and 4.6 nm diameter CdS quantum dots in toluene.

## 5.3 Decoration of CdS QDs on ZnO nanorods

Figure 5.2(a) shows the cross-sectional scanning electron micrograph (SEM) of typical single-crystal ZnO nanorods on the ITO glass substrate. The nanorods have lengths and diameters ca. 320 nm and 90 nm, respectively. Figure 5.2(b) shows dark-field TEM images of a ZnO nanorod decorated with CdS QDs (4.6 nm) and demonstrates CdS QD coverage on the nanorods was so high to cover the nanorods. The attached QDs appear as randomly oriented crossed-fringe patterns on the nanorods surface, and energy dispersive spectrometer (EDS) confirms that they are CdS (Figure 5.2(c)). These figures prove we achieve relatively high coverage of CdS QDs on ZnO nanorods and a uniform coverage throughout the film. Moreover, because prolonging time of immersion in CdS solution does not further increase CdS absorption, we assume the coverage of CdS particles on ZnO nanords surface to be a

monolayer. Such monolayer coverage of the CdS particles is analogous to TiO$_2$ films modified with sensitizing dyes [142].
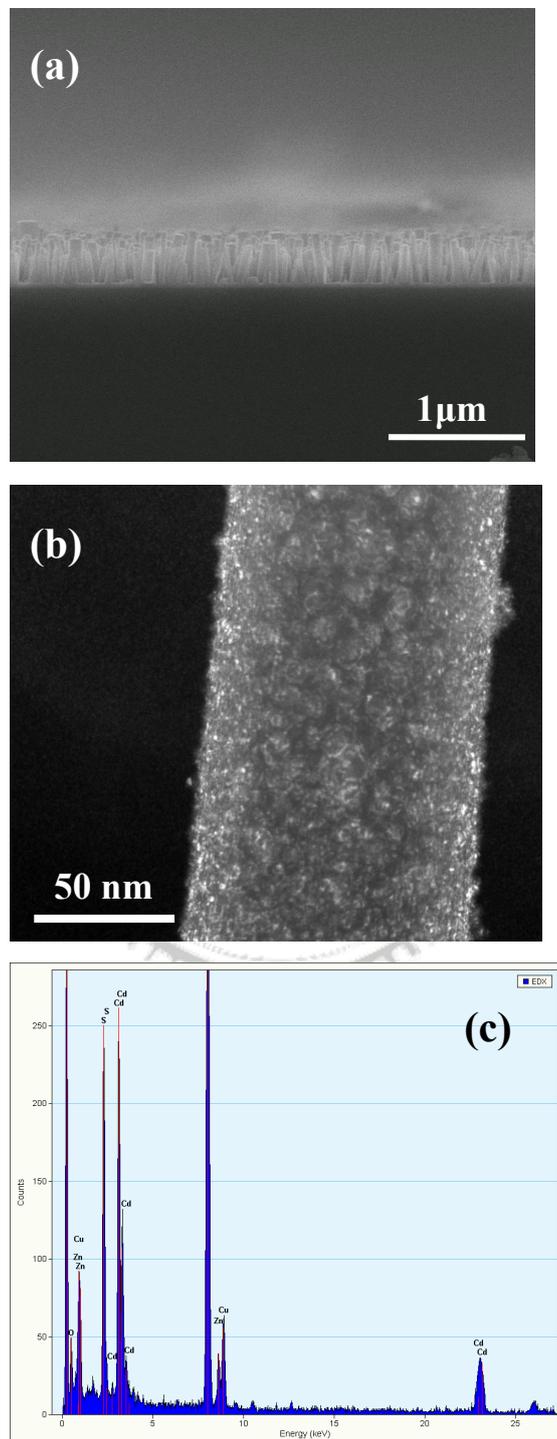


**Figure 5.2** (a) Cross-sectional scanning electron micrograph of ZnO nanorods. (b) Dark-field transmission electron micrograph of a ZnO nanorod decorated with CdS

QDs. (c) Element composition analysis of an individual ZnO nanorod decorated with CdS QDs.

## 5.4 Annealing effect on P3HT

The P3HT film annealed at 200 °C, around the melting point of P3HT [143], suggest that the polymer completely fills the nanorod array, as shown in Figure 5.3(a). Moreover, X-ray diffraction (XRD) patterns show that annealed the composite film substantially improves the P3HT crystallinity, which should enhance its hole mobility [144]. Intensifies and sharpens of the P3HT (100) diffraction peak are improved significantly, which originates from crystals with their alkyl spacing direction (100) normal to the substrate (Figure 5.3(a)). Diffraction peaks of CdS QDs don't appear due to a fewer amount of CdS QDs. Figure 5.3(b) illustrates the UV-vis spectra of ZnO/P3HT annealed at 220 °C and without annealing. The UV-vis spectra of composite films show the development of a well-defined shoulder at ~610 nm upon annealing. This feature is connected with an increase in molecular order and enhanced hole mobility in the P3HT film [145].
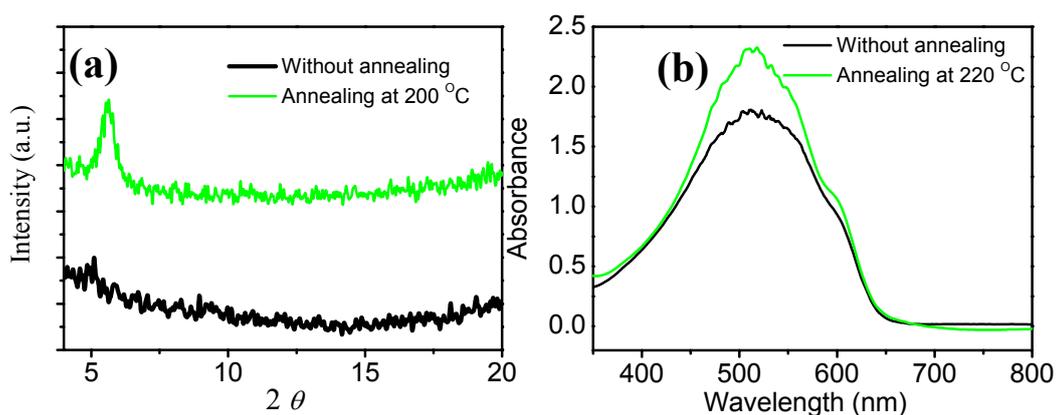


**Figure 5.3** (a) XRD patterns of ZnO/CdS/P3HT with annealing at 220 °C and without annealing. (b) Absorption spectra of ZnO/CdS/P3HT with annealing at 220 °C and without annealing.

## 5.5 Effect of CdS QD size

Figure 5.4 shows the current density-voltage (J-V) characteristics of hybrid solar cells based on P3HT and ZnO nanords with and without CdS QDs under simulated AM 1.5G irraadiation at an intensity of 100 mW cm$^{-2}$ in the air. Modifying the ZnO nannorods with CdS QDs, short-circuit current density $J_{SC}$ of the hybrid solar cell reached 1.14 mA cm$^{-2}$, which was 2.9 times larger than that without CdS QDs. (Table 2 and Figure 4). It seems plausible that the increased photocurrent is attributed to the efficient photosensitizing effect of the CdS QD for metal oxide owing to the absorption bands in the visible region. To determine the origin of the increase in $J_{SC}$, we measured the J-V curves of solar cells based on P3HT and ZnO nanords modified with three different-sized CdS QDs, as can be seen in Figure 5.4. It shows that when the absorption bands of CdS QD shift to UV region (2.2 nm and 3.2 nm), the $J_{SC}$ are still improved. The $J_{SC}$ varies with particle sizes and the maximum photocurrent is seen with 3.2 nm diameter CdS particles. It suggests that other mechanisms should be involved in the increase in $J_{SC}$ except photocurrent from QDs. For electron transfer from donor to acceptor to occur, the lowest unoccupied molecular orbital (LUMO) of donor needs to be ~0.5 eV higher than the LUMO of the acceptor [146]. In this case of P3HT, however, this energy difference is much higher, namely 1.2 eV so we suspected that the ZnO/P3HT interface is not a suitable one for charge separation. Therefore, we replaced ZnO/P3HT interface with CdS QDs/P3HT interface which is known to readily split excitons generated in P3HT. Expected energy levels of ZnO, CdS, and P3HT, determined from literature values [147-149], are presented in Figure 5.5(a). The conduction band of bulk CdS is lower in energy than LUMO of P3HT, enabling an electron transfer cascade from P3HT to the CdS interface layer to ZnO and, thereby, potentially enhancing charge separation at the ZnO interface.

Additionally, due to the valence band level of bulk CdS relative to P3HT, the CdS QD is expected to obstruct hole transfer between P3HT and ZnO, and thus to localize hole in the P3HT away from the metal oxide surface. Thus, the CdS QDs serve as an electronic mediator that enhances the electron transfer efficiency from P3HT to ZnO. Moreover, because of the small electron effective mass ($m_e$ = 0.2 $m_o$) versus the significantly larger hole mass ($m_h$ = 0.8 $m_o$), the shift in the conduction band energy is significantly greater than the shift in valence band energy for quantized particles resulting in increasing the driving force for charge injection. Thus, we can optimize the interface energetics by adjusting the size of CdS QDs.
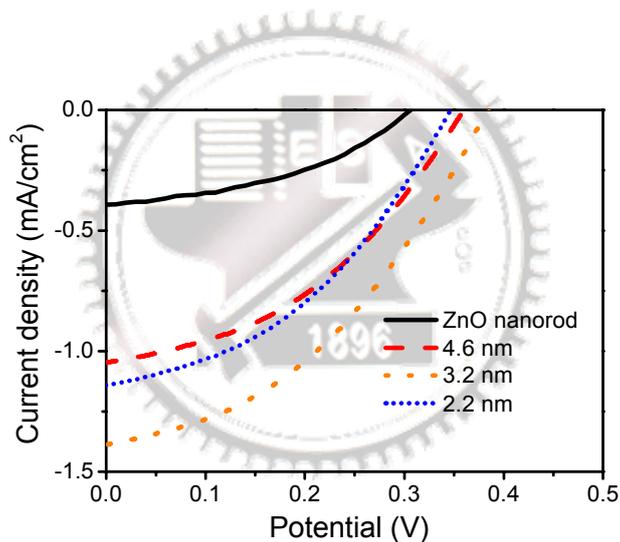


**Figure 5.4** Photovoltaic performances of the devices with different diameter CdS quantum dots.

**Table 2** Summary of the device performance of different diameter CdS quantum dots.

| | $J_{SC}$ /mA cm$^{-2}$ | $V_{OC}$ / V | FF (%) | PCE (%) |
|---|---|---|---|---|
| Only ZnO | 0.39 | 0.30 | 40 | 0.05 |
| 2.2 nm | 1.05 | 0.36 | 39 | 0.15 |
| 3.2 nm | 1.38 | 0.38 | 41 | 0.21 |
| 4.6 nm | 1.17 | 0.35 | 40 | 0.16 |

The energy of the lowest exciton state ($E_{CdS}$*), a bound pair of 1S electron in the conduction band (CB) and 1S hole in the valence band (VB), is given by [150,151]

$$E_{CdS*}[1s_e, 1s_h] = E_g + \frac{\hbar^2 \pi^2}{2R^2}[\frac{1}{m_e^*} + \frac{1}{m_h^*}] - \frac{1.8e^2}{4\pi\varepsilon_0 \varepsilon R} \qquad (1)$$

where $E_g$ is the bulk bang gap, $R$ is the radius of the QD, and $m_e^*$ and $m_h^*$ are the effective masses of electrons and holes, respectively. The second and third terms are the confinement energy of the 1S electron and 1S hole, respectively. The fourth term results from electron hole coulomb attraction. Following the Brus' theory [150,151], we estimated the shift in the conduction band energy for QDs with an average diameter 2.2 nm, 3.2 nm, and 4.6 nm is about 0.9 eV, 0.5 eV, and 0.2 eV respectively. Therefore, when we employ 3.2 nm CdS instead of 4.6 nm quantum dots, the energy difference between the CB of CdS and the LUMO of P3HT is reduced to 0.5 eV which is optimal value for electron transfer.[19] Because of the optimal offset, easy electron transfer from P3HT to CdS causer the $J_{SC}$ to increase 1.3 times. In contrast with 2.2 nm CdS QDs, lower $J_{SC}$ should be mainly due to less overlap between 2.2 nm CdS QDs absorption and the solar spectrum.
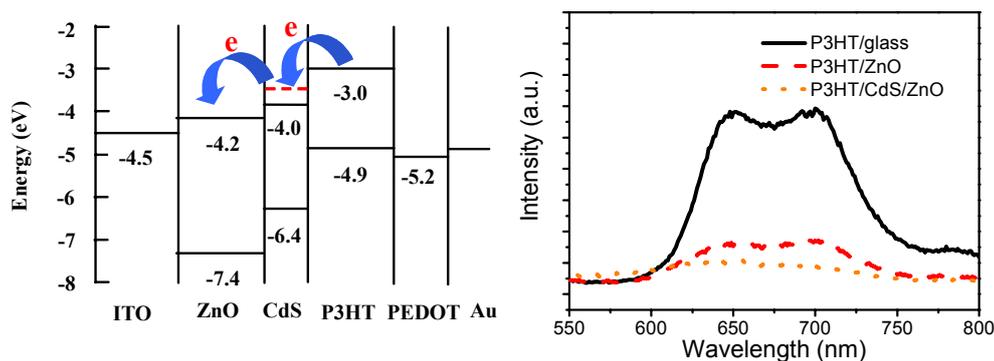
**Figure 5.5** (a) The corresponding energy levels of the nanostructured photovoltaic device based on ZnO/CdS/P3HT hybrid. (b) The photoluminescence spectra of P3HT deposited on glass slides and on ZnO nanords with and without 3.2 nm CdS QDs.

In addition, the increased $V_{OC}$ should be attributed to the action of the CdS QDs which act as an energy barrier both in blocking holes in the P3HT from reaching the ZnO surface and recombining with electrons in the oxide. This is probably because the monolayer high coverage of CdS QDs is analogous to dyes at the interface separate the P3HT from ZnO nanorods properly and completely prevents the direct contact between them, thereby suppressing the charge recombination between the holes in the P3HT and the electrons injected into ZnO nanorods. The range of open circuit voltages observed for devices with CdS QDs is 0.35 to 0.38 V. The open-circuit potential is slightly dependent on CdS particle size, indicating that electrons injected from excited CdS into ZnO quickly relax to the lowest conduction band energy.

Figure 5.5(b) shows the photoluminescence (PL) spectra of P3HT deposited on glass slides and on ZnO nanords with and without 3.2 nm CdS QDs. CdS QDs and ZnO nanorods both can act as electron acceptor when they are combined with P3HT. When P3HT deposited on ZnO, a quenching of the emission can be seen. PL quenching can evidence the photoinduced charge transfer from P3HT to ZnO

nanorods. When CdS QDs were anchored on ZnO nanorods, a more quenching of the emission is observed in ZnO/CdS/P3HT structure, suggesting CdS QDs can improve electron transfer from P3HT to the ZnO. This result is consistent with the increased $J_{SC}$ in Figure 5.4.

## 5.6 Summary

We found that decorating CdS QDs on ZnO nanorods improves not only $J_{SC}$ but also $V_{OC}$. Moreover, the $J_{SC}$ is highly related to the size of CdS QDs due to the improvement of electron injection. On the other hand, $V_{OC}$ also increases by decorating QDs but it is slightly dependent on the size of CdS QDs. Based on these results, we demonstrate that the use of QDs result in significant improvements in device performance, and that these improvements are due to faster electron injection and slower charge recombination. A photovoltaic device based on the decorated-QD nanorod structure with P3HT polymer shows PCE over four times greater than that for a similar device without QDs. The best ZnO nanorod/CdS/P3HT device yields a short circuit current density of 1.38 mA cm$^{-2}$ under AM1.5 illumination and resulting in a power conversion efficiency of 0.21% (100 mW cm$^{-2}$).

# Chapter 6

# In-situ Growing CdS Single-Crystal Nanorods via P3HT Polymer as a Soft Template for Enhancing Photovoltaic Performance

## 6.1 Introduction

Optoelectronic devices based upon conducting polymers and inorganic nanocrystals are widely studied as type-II bulk heterojunctions [6, 50, 152–154] because nanocrystals can act as electron acceptors to assist charge separation and broaden the spectral response. Creating these materials with well defined physical and electronic properties is an important step towards building type-II bulk heterojunctions. Various high electron affinity inorganic semiconductors including CdSe [50] ZnO [155] CdTe [156] and $TiO_2$ [157] have been widely studied for bulk heterojunction polymer solar cells. However, few studies have been reported for utilization of CdS as an important II-VI semiconductor in nanocrystals-conjugated polymer composite, probably due to the relatively large band gap (2.42 eV) that absorbs light ranging from 300 to 512 nm and mismatches with the solar terrestrial radiation (300-1500 nm). Among them the highest power conversion efficiency for a CdS/polymer hybrid solar cell was reported by Wang et al., who fabricated a hybrid solar cell with MEH-PPV and CdS nanorods with a diameter of 3.5 nm and length of 35 nm and obtained a power conversion efficiency of 1.17% [84]. However, since CdS has high electron mobility and the conduction band edge is more negative than the $H_2O/H_2$ redox potential [158], it is believed that there has much room for further improvement in the conversion

efficiency for hybrid CdS/conjugated polymer photovoltaic devices.

Conventional method for preparing a nanocrystal-conjugated polymer composite is by mixing a given polymer with nanocrystals through the use of surfactants, where the surfactants would form an insulating interface, even in a nanometric length, between the polymer matrix and the nanocrystals, further deteriorates charge transfer ability [50, 153]. A variety of methods exists in literature for the synthesis of ligand-capped metal chalcogenide nanocrystals with controlled size and shape [159-161]. Although the incorporation of the surface ligands into an organic/inorganic composite can improve distribution of nanocrystals in a conjugated polymer, two significant drawbacks ruin the efficiency considerably. First, the ligands inhibit charge transfer between the polymer and the nanocrystals [6]. Second, mixing pyridine-capped nanocrystals and polymer requires the use of co-solvent, which can adversely affect nanocrystal solubility and polymer chain orientation. These problems can be bypassed by directly growing nanocrystals in a conducting polymer solution without surfactants or ligands [154, 162]. As demonstrated in an early report where an in-situ synthetic method was employed to synthesize PbS nanocrystals/MEH-PPV composite and showed that the polymer chains can act sterically to stabilize nanocrystal growth in solution [162, 163]. Up to now, only a few reports were related to the polymer template-directed synthesis of semiconductor nanowires, with notable examples including micro channels within a thin polymer film [164], a polymer-assisted solvothermal process [165-167], mesoscale structures self-assembled from AB or ABC block copolymers [168, 169]. It is generally believed that the in-situ formation of 1-D nanostructures, e.g. nanorods, in the composite is technically desirable for photovoltaic application, because 1-D nanostructures exhibit much better connectivity than spherical nanoparticles and act as large surface-area electron acceptors in a bulk heterojunction. [50] In addition, the nanorods are

confined in two dimensions modifying the band structure, which results in a tunable optical absorption edge [50] while allowing exciton diffusion and separation along the unconfined dimension [170]. As reported by Sun et al., CdSe nanorod/polymer hybrid solar cell with a power conversion efficiency of 2.6% can be obtained by mixing CdSe nanorods with an aspect ratio of 13 with P3HT [171].This also proved that the efficiency of hybrid photovoltaic devices can be improved by using nanocrystals with a higher aspect ratio. However, ligands that inhibit charge transfer still existed between the polymer and the nanocrystals. Therefore, development of semiconductor nanorods with high aspect ratio, without the use of surfactants and/or ligands, should be more technically interesting with improved power-conversion efficiency for a quantum dot-based photovoltaic device. Here, we report the synthesis of one dimensional CdS nanocrystals with various aspect ratios in the presence of conducting polymer head-to-tail (HT) poly(3-hexylthiophene-2,5-diyl) (P3HT). The HT-P3HT can access a low energy planar conformation, leading to highly conjugated polymers that provide flat, stacking macromolecular structures that allows self-assemble, providing efficient interchain and intrachain conductivity pathways. Moreover, the choice of solvent gives an impact on the extent to which the P3HT chains straighten out. Other study [172] found that the chains are initially rather coiled up and the extent to which they uncoiled to form straight structures varies strongly with the choice of solvent. Poor solvents lead to chains with a much shorter average hydrodynamic coil radius in solution.   In the case of P3HT, the addition of a minor amount of a poor solvent (e.g. methanol) to the solution of P3HT in a good solvent (e.g. chloroform) is accompanied by solvatochromic transition which was explained by Rughooputh et al. [173] as a rod-to-coil transition (stretched structure to ring structure). Therefore the physical conformation of P3HT chains is affected by solvents. Since the conformational change of the sulfur-bearing P3HT macromolecule

54

may be manipulated via a co-solvent method, the molecular structure of the resulting P3HT can be tunable with various conformations, e.g., from highly-tangled coil to elongated or straightened conformation. If this is what is expected, the exposed sulfur atoms along the backbone of the P3HT to the environment may provide anchorage sites for CdS to nucleate and growth. The P3HT is then used as a dual function macromolecule; that is, acting as a structure-directing template to manipulate the geometrical development of CdS nanocrystals, in the meantime, becoming an efficient photo-electron conductor when the final CdS-P3HT composite structure can be well constructed, which, to our best knowledge, is designed for the first time and is highly plausible for solar cell application.

## 6.2 Effect of temperature

Figures 6.1(a)-(c) show the transmission electron microscopy (TEM) images of the nanocrystals taken at 120 °C, 150 °C, and 180 °C, respectively. It was found that the size of the nanocrystals was increased with the reaction temperature. High resolution transmission electron microscopy (HRTEM) image, Figure 6.1(d), shows well-developed lattice fringes of the nanocrystals synthesized at 180 °C, indicating the nanocrystals possess high crystallinity.
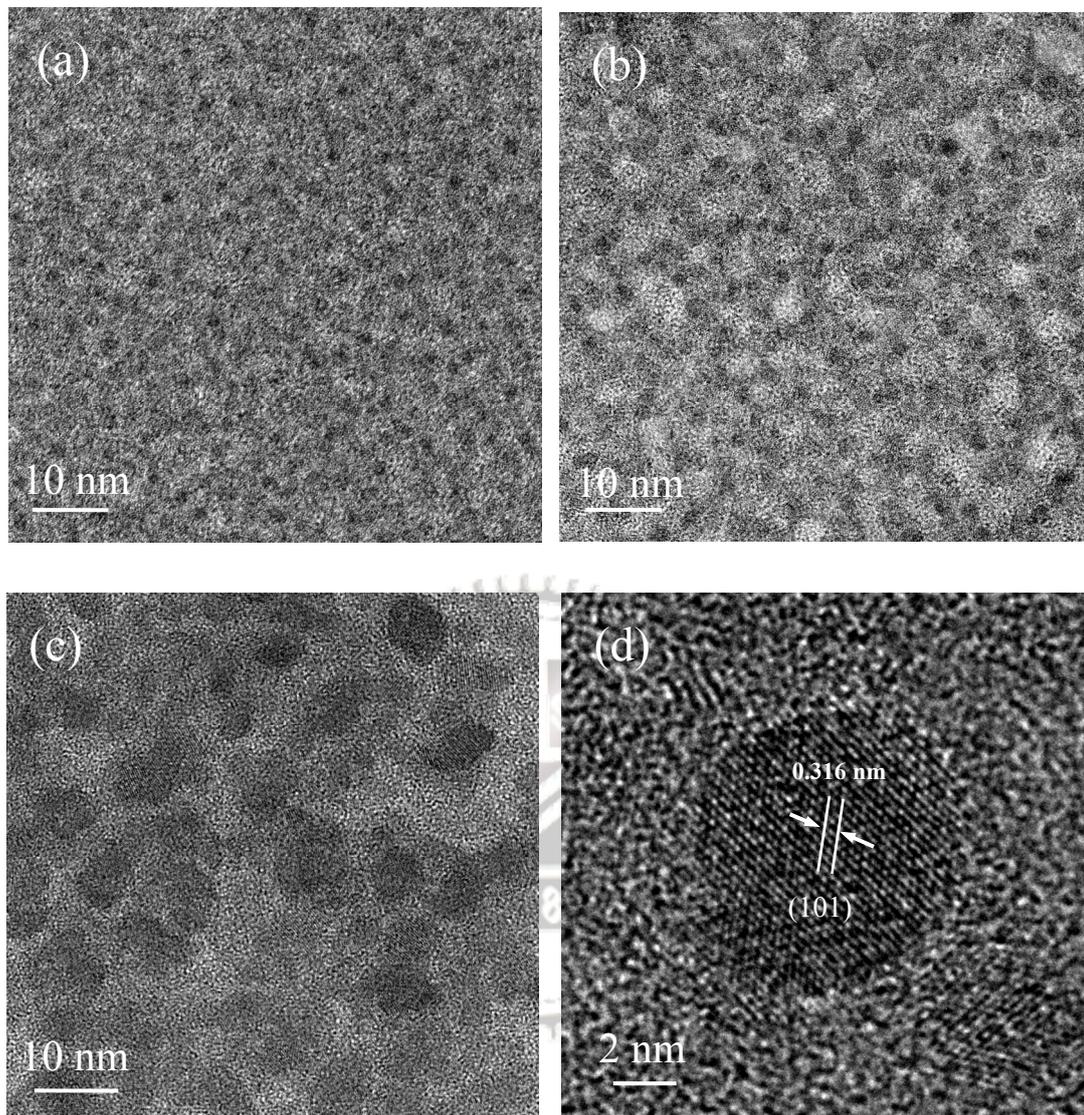
**Figure 6.1** TEM images of CdS nanocrystal ensembles taken at (a) 120, (b) 150, and (c) 180 °C (d) HRTEM image of the lattice planes in a single CdS nanocrystal.

## 6.3 Effect of concentration

To better understand the in-situ formation of CdS, the influence of reaction parameters, including the concentration of cadmium acetate (and sulfur) and the DCB-to-DMSO ratio on the in-situ reaction were investigated. Figure 6.2 shows the TEM images of CdS/P3HT samples prepared at different concentration of cadmium

acetate at 180 °C with ratio for DCB-to-DMSO of 8:4. When the concentration of cadmium acetate increases to 2.5mg/ml, CdS nanorods are formed accompanied by CdS nanocrystals, as shown in Figure 6.2(a). As the concentration increases to 8.3mg/ml, the amount of nanorods also increases and the nanorods become dominant in this condition as illustrated in Figure 6.2(b). For the sample synthesized from 8.3mg/ml, the diameter of the nanorods is almost the same as that of samples prepared from 2.5mg/ml but the aspect ratio increases to approximately 8. However, while the concentration exceeded 8.3mg/ml (i.e. 12.45mg/ml), except the formation of the nanorods, nanocrystals (i.e., defined as the ones with equiaxial dimension) are simultaneously observed, Figure 3(c), indicating there exists a critical concentration for the nanorod to evolve. The HRTEM image of a single nanorod (appeared in Figure 6.2(b)) is illustrated in Figure 6.2(d) which confirms a preferential growth of the CdS nanocrystals via its crystallographical (002) orientation. Moreover, the nanostructural evolution of the nanorod was observed in the presence of the P3HT, suggesting the macromolecule may act as a structure-directing template to assemble the growth of the nanocrystal. These observations indicate that the concentration at 8.3mg/ml provides optimal reaction condition for the growth of CdS nanorods, along the templated P3HT molecule, rather than those earlier studies where rod-like structure was evolved due to a self-assembly of individual equiaxal nanocrystals through dipole-dipole interactions [174].
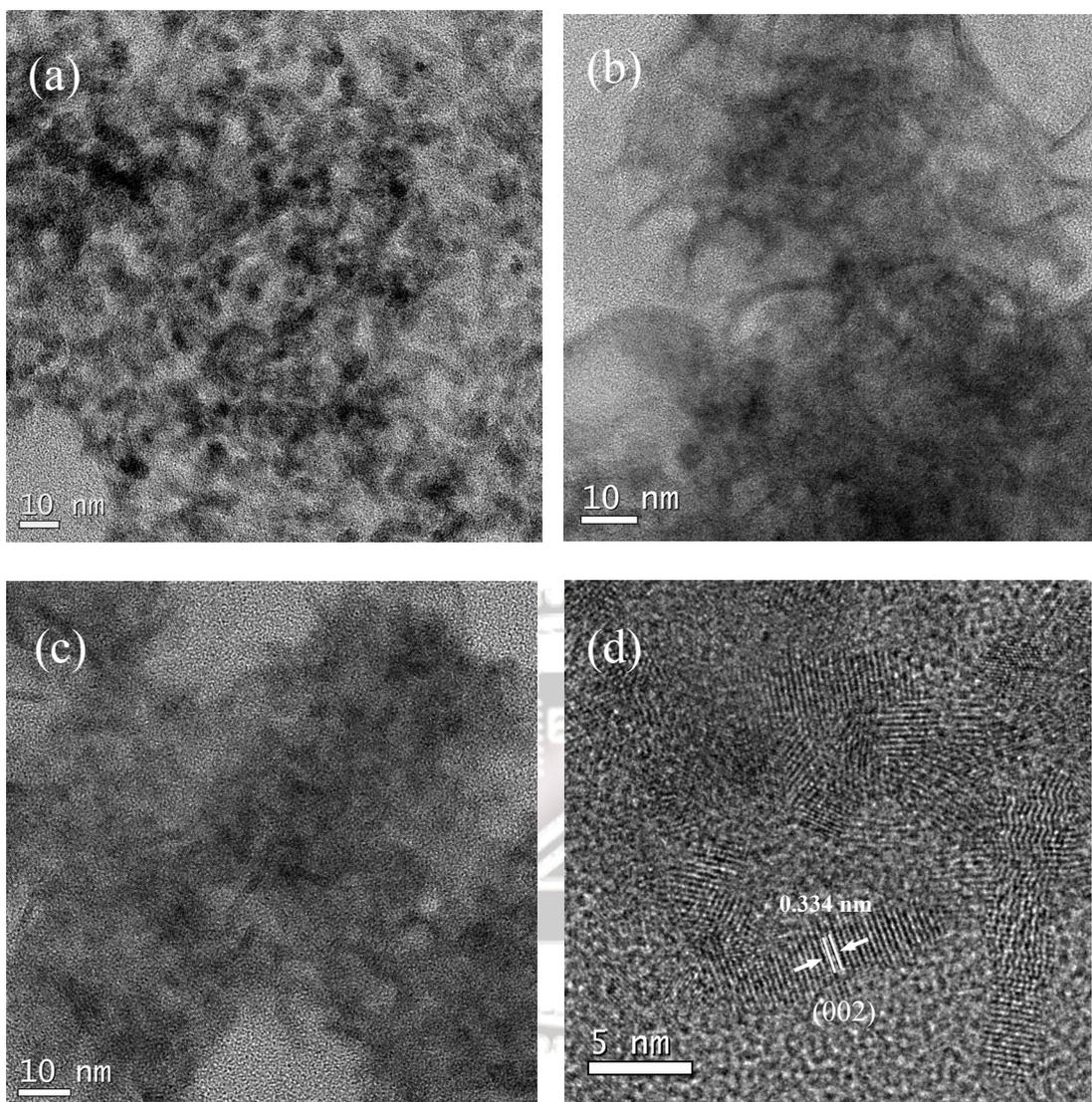
**Figure 6.2** TEM images of CdS nanorods synthesized in P3HT with cadmium acetate concentration of (a) 2.5 mg/ml, (b) 8.3 mg/ml, and (c) 12.45 mg/ml. (d) HRTEM image of the nanorod.

Besides the thermodynamic and kinetic factors controlling the synthesis of inorganic nanorods, we believe that P3HT should play a critical role in directing the growth mechanism. It is well known that both the size and the shape of many inorganic nanocrystals can be dimensionally tuned in a molecular-to-nanometric scale by employing various organic molecules as capping agents during the synthesis process [175]. In this study, the planar P3HT conformation may provide flat, stacking

molecular architecture to guide the growth of CdS nanocrystals in an oriented approach like capping agent. It was found that the morphology of the CdS nanorods is significantly determined by the concentration of cadmium acetate in the starting solution.

## 6.4 Mechanism of CdS growth

In order to further elucidate the role the P3HT in CdS crystal development, a comparison of the FTIR transmission spectrum of before and after adding cadmium acetate in reaction and after the reaction is given in Figure 6.3(a). These characteristic bands in the P3HT are 1506, 1455 (aromatic C=C stretching), 1381 (methyl bending), 1106 (C-S stretching), 818 (aromatic C-H out-of plain), and 722 cm$^{-1}$ (methyl rock). After adding cadmium acetate in the solution, characteristic bands of cadmium acetate molecules are observed at 1560 and 1418 cm$^{-1}$ (carboxylate stretching) which overlapped the characteristic bands in the P3HT (1506, 1455, 1381 cm$^{-1}$). However, a slightly shifted by 5 wavenumbers, corresponding to $6.4 \times 10^{-4}$ eV, to a lower energy region of C-S characteristic band is observed in the IR spectrum, after mixing of P3HT and Cd precursor, indicating a reduction of the C-S bond energy. This finding suggests additional intermolecular interaction that is activated at the expense of the original C-S bond energy, by, for instance, a slight distortion of electronic cloud of the C-S bond. The origin of such an additional intermolecular interaction most probably results from a strong dipole-dipole or ion-dipole interaction between the Cd$^{2+}$ ions and S atoms, prevailing along the backbone of the P3HT chain. The planar P3HT conformation may provide flat, stacking molecular architecture, as schematically shown in Figure 6.3(b). As such, the Cd$^{2+}$ ions may be immobilized in a confined space within the network structure of the P3HT through the dipole-dipole interaction and stayed in place while subjected to a subsequent nucleation-and-growth process

with the adding sulfur ions. This would result in uniformly and randomly distributed CdS nanocrystals and nanorods within the polymer, as evidenced in Figures 6.1 and 6.2. In order to further prove the hypothesis of this work, we performed a control experiment. It was running in the absence of P3HT but with the presence of both DCB and DMSO. The resulting nanoparticles were examined using TEM, where the obtained nanoparticles with longer aspect ratio, were not found but large particles with equiaxial geometry were found. Manoj et al. have reported DMSO can form a complex with Cd during CdS synthesis and results in the formation of capped CdS nanoparticles [176]. However, in this study, no so-called Cd(S)-DMSO complex formed during reactions according to the results of FTIR spectra. There is no any sign of the absorption peaks originating from DMSO or DCB was detected, such as 800 and 1261 $cm^{-1}$ which originated from Cd(S)-DMSO complex capped CdS nanoparticle itself.

It is known that the high-energy facets grow more quickly than the low-energy facets in a kinetic regime [175] and the (001) crystal face of CdS has the highest surface energy than all other crystal faces [177]. Consequently, a preferential growth of the CdS nanocrystals along the high-energy facet evolved in the presence of P3HT template, leading to the formation of CdS nanorods. However, if the cadmium acetate concentration is less than 2.5mg/ml, lower $Cd^{2+}$ ion concentration renders insufficient growth to form rod-like structure, resulting in formation of equiaxial nanocrystals, as schematically illustrated in Figure 6.3(c). However, with the increase in cadmium acetate concentration, nanorod was successfully developed, Figure 6.3(d). This is due to much more amount of free $Cd^{2+}$ions available in the solution that allow a subsequent growth of the nanorods by depositing onto the immobilized $Cd^{2+}$ ions along the chain.
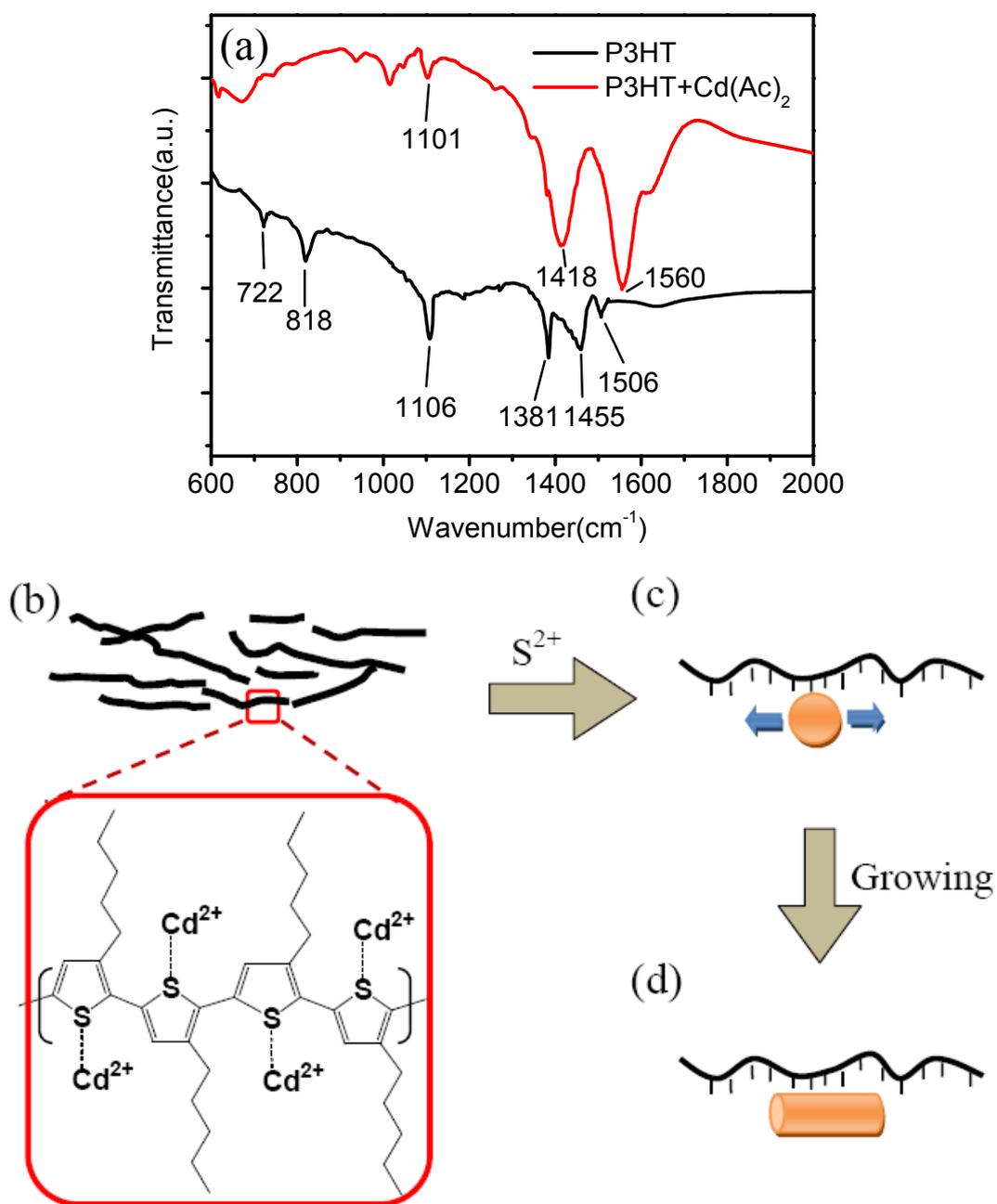
**Figure 6.3** (a) FTIR spectra before and after adding cadmium acetate in reaction and after the reaction (b) Schematic drawing for the proposed synthesis scheme of CdS/P3HT composite. The $Cd^{2+}$ ions were assumed to be coupled with the unpaired S along the P3HT planar chain network. Proposed mechanism for the growth of (c) CdS nanocrystals and (d) nanorods.

## 6.5 Effect of solvent ratios

The role of structural direction of the P3HT template is essential, since it is assumed, reasonably that the sulfur atoms along the backbone of the P3HT may act as active sites for $Cd^{2+}$ ions to anchor. Following addition of the sulfur precursor, the sites of $Cd^{2+}$ ion anchorage turn to be the sites for the nucleation and growth of CdS nanocrystal, along the backbone of the P3HT chain, forming CdS nanorod. The single-crystalline nature of the nanorods of various aspect ratios mentioned above suggests an epitaxial-like growth of the CdS nanocrystals along the exposed sulfur-bearing segments of a given macromolecular chain in a given solvent environment. Such a scenario, if molecularly accessible, can be applicable for the nanorods of technically desirable aspect ratio through the manipulation of co-solvent environment where the conformational development of the P3HT polymer can be possible. In other words, an extended and straightened, e.g., in a linear form of, P3HT chain can be evolved if a "good" solvent is applied upon the synthesis of the nanorod. The aspect ratio of the resulting nanorod can be controlled according to the length scale of the P3HT chain that extended into the diluting environment. On this basis, a variation of the DCB-to-DMSO volume ratio from 7:5, 8:4 to 9:3 gave the nanorods of aspect ratio increasing from 4, 8 to 16 for the samples with the same concentration under similar reaction conditions, respectively. As evidenced from Figure 6.4, the aspect ratio obtained from the 9:3 ratio was nearly doubled the value compared to that for DCB-to-DMSO of 7:5. Furthermore, it was found that when reaction time is over 30 min, the aspect ratio does not change too much. This demonstrates that a larger ratio of DCB to DMSO can enhances the aspect ratio and growth rate of the nanorods as a result of the conformational variation of P3HT chain in the co-solvent systems. Both structural morphologies of the CdS nanorods synthesized from the 9:3 and 7:5 ratios at 8.3mg/ml for 30 min are shown in Figure 6.5 (a) and 6.5(b), respectively.

This indicates that an elongated P3HT chain can be developed upon an increasing DCB-to-DMSO ratio, which corresponds to an increasing CdS size evolution along the (002) direction, resulting in the nanorods with higher aspect ratio. This finding strongly suggests that the templating mechanism of the P3HT macromolecule mentioned above is behaved as a result of a solvent-dependent variation of the polymer chain.
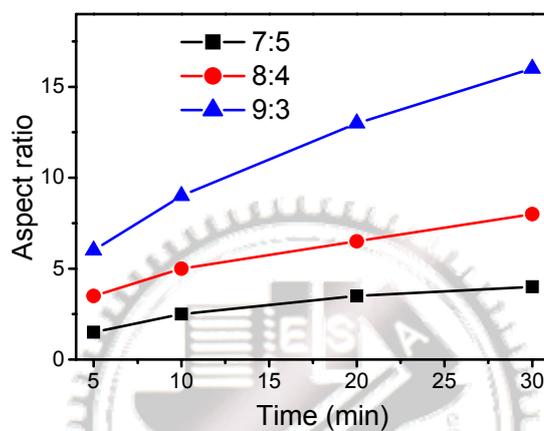


**Figure 6.4** Average aspect ratio of CdS nanocrystals plotted as a function of the reaction time for the CdS nanorods growth.

A recent study by Stavrinadis [174] indicated that the PbS nanorods developed from the PbS/MEH-PPV composite are primarily composed of chain of nanocrystals rather than single-crystal nanorod structure. However, in this study, we succeeded in producing CdS single-crystal nanorods in an in-situ method. Therefore, it is believed that the growth mechanism of single-crystal nanorod structures is related to P3HT special chain conformation and inter-chain spacing. In addition, it is well-known that the regioregular, head-to-tail P3HTs can access a low energy planar conformation, leading to highly conjugated polymers so we believe that P3HT may act as a molecular template for geometrical manipulation of CdS nanocrystals.
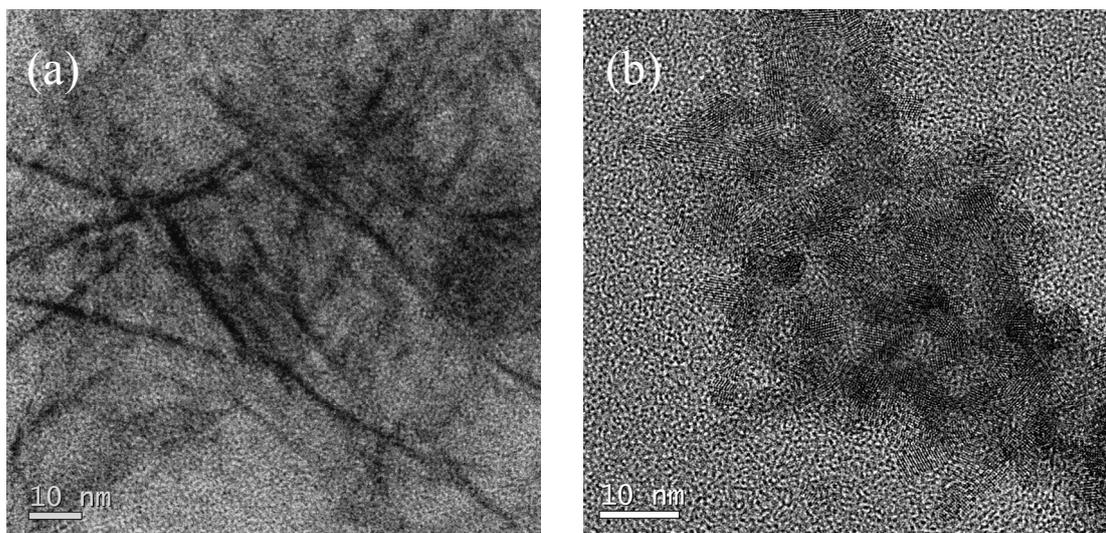
**Figure 6.5** TEM image of CdS nanorods synthesized in P3HT with volume ratio DCB-to-DMSO of (a) 9:3 and (b) 7:5.

## 6.6 Photovoltaic performance

Figure 6.6 shows the photoluminescence emission spectra of P3HT and CdS /P3HT composites in toluene. In agreement with previous work [162] a reduction in the spectral intensity of the composites relative to the reference P3HT sample was observed and the reduction of PL intensity is increased with the aspect ratio of CdS nanorod. This reduction of PL intensity is due to photogenerated charge transfer between the CdS and P3HT [33]. According to previous studies, the decreased photoluminescence intensity of the composites is related to an improvement in photovoltaic performance [52]. The photoluminescence quenching can be also used as a powerful tool for evaluation of charge transfer efficiency in the donor-acceptor blend composites [30, 178]. Once the photogenerated excitons are dissociated, the probability for recombination should be significantly reduced. This is a well-known effect of the ultrafast electron transfer from the donor to acceptor and it is expected to increase the exciton dissociation efficiency in photovoltaic devices [30, 178, 179].

Thus the synthesis of the composites with high-aspect-ratio, single-crystal CdS nanorods provides a significant interest and encourages for further investigations onto the photoconductivity assessment for solar cell use.
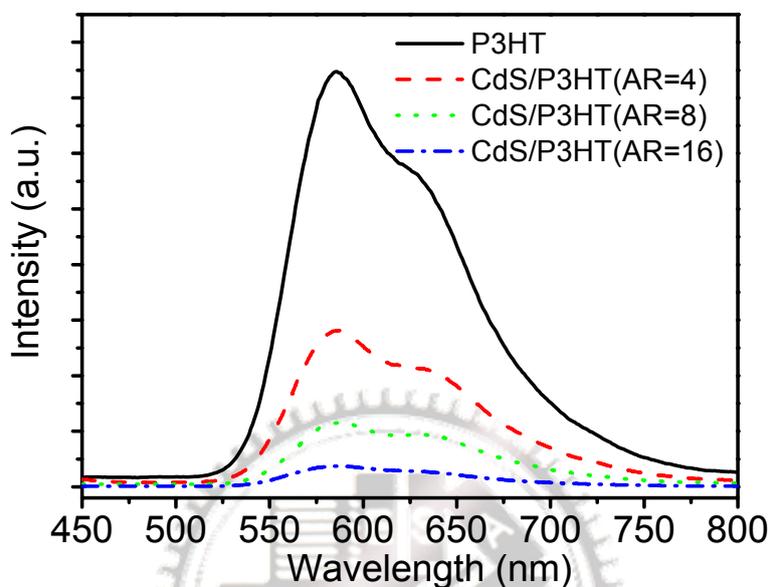


**Figure 6.6** Photoluminescence emission spectra for P3HT and CdS nanorods/P3HT composite solution (both solutions in toluene pumped at 450 nm).

Figure 6.7 gives a summary of operating characteristics for P3HT/CdS-based device using the synthesized CdS nanorods of various aspect ratios. Figure 6.7(a) shows the variation of both $J_{SC}$ and $V_{OC}$ with various aspect ratios of CdS nanorods. It was observed that $J_{SC}$ obviously increased with the aspect ratio of the CdS nanorods but $V_{OC}$, which is limited by the difference between the HOMO of the donor and the LUMO of the acceptor [20, 180], remained identical at ~0.64 V. It suggests a percolation of the CdS forming connective network across the device, rendering the device behaves like a complete heterojunction. The influence of aspect ratio of the CdS nanorods on power conversion efficiency (PCE) and fill factor (FF) is illustrated in Figure 8(b). Comparing with Figures 8(a) and 8(b), it can be found that both $J_{SC}$

and FF increased with the aspect ratio of the CdS nanorods, suggesting that the aspect ratio of CdS nanorods reduced charge recombination. The PCE of the well-assembled device using the nanorods with aspect ratio of 16 leads to a considerable improved power conversion efficiency as high as 2.9% due to an increase in both FF and $J_{SC}$. It was inferred that for the photoactive layers consisting of equiaxial nanoparticles, electron transport is dominated by hopping, but the band conduction is prevalent in the photoactive layers consisting of nanorods [50] because the presence of nanorods with high aspect ratio can penetrate through a large portion of the device to develop percolation pathways for electron transport. In other words, longer nanorods are easier to form a percolation path between two electrodes and thereby can thus fully contribute to photovoltaic conversion. Therefore, the increase in PCE and $J_{SC}$ is primarily a result of efficient charge transport.
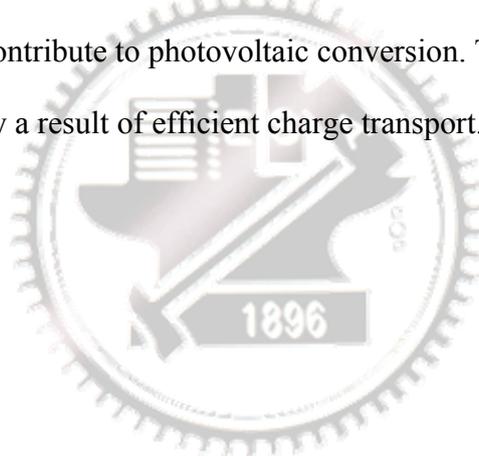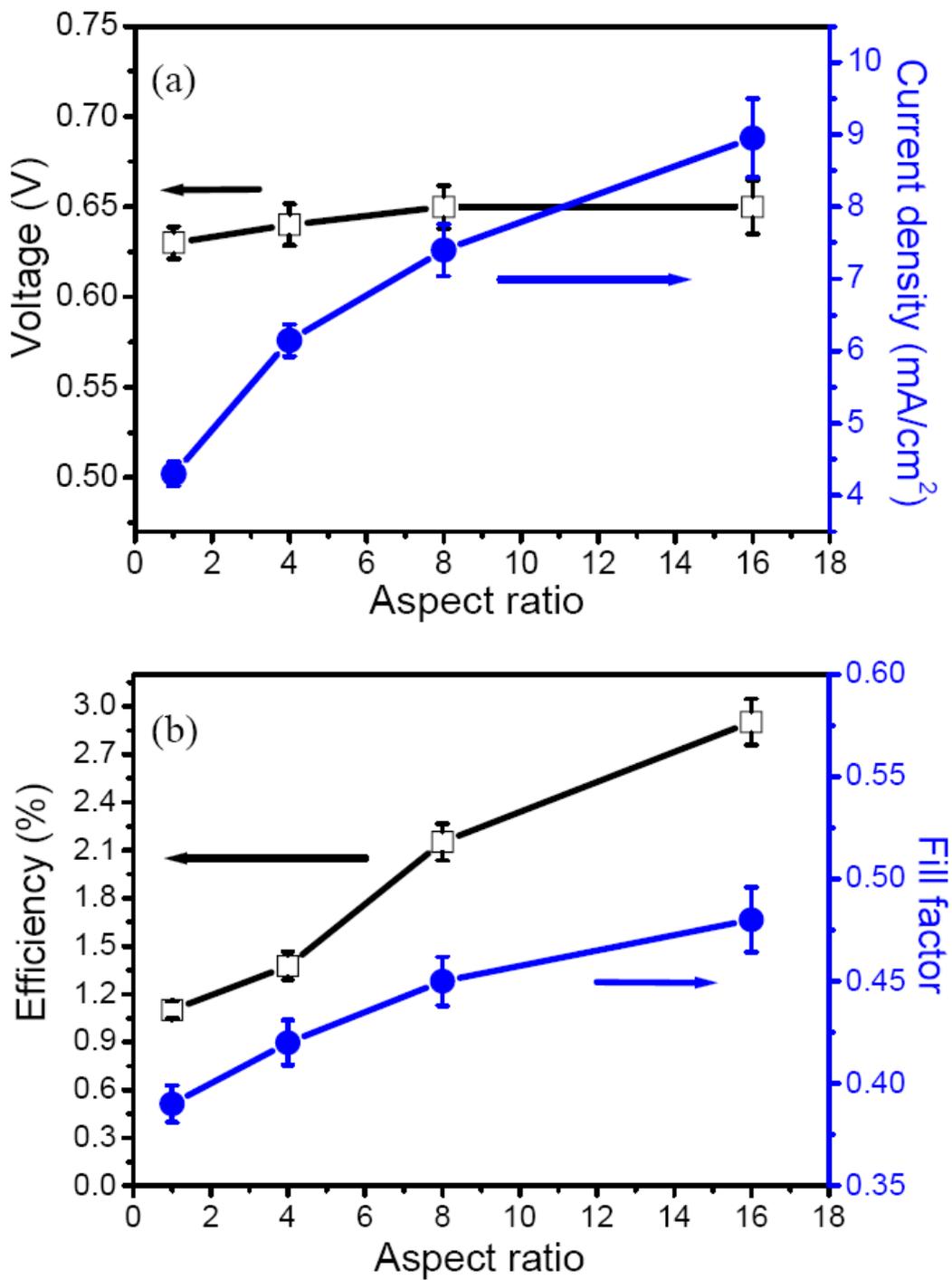
**Figure 6.7** Hybrid solar cell characteristics. (a) $V_{OC}$ and $J_{SC}$ (b) PCE and FF.

## 6.7 Summary

Formation of CdS nanorods and the corresponding variation of the aspect ratio of the nanorods can be well manipulated via a soft templating technology using the

planar P3HT polymer, as a molecular template upon synthesis, and in the meantime, as a conducting matrix to form final P3HT-CdS composite structure, which, to the best of our knowledge, has been explored for the first time. The formation of the nanorods with various aspect ratios, ranging from ~8 to 16, is controlled by the DCB-to-DMSO ratio of the co-solvent. The nanorods with higher aspect ratio allow connective network to develop in the P3HT matrix, facilitating percolation pathways for electron transport. Therefore, the charge transport is considerably enhanced by using the CdS nanorods with higher aspect ratio. The enhancement in carrier mobility can be accomplished by improving the CdS-P3HT interface without the involvement of surfactants. All above merits give a PCE to a level as high as 2.9%, albeit there has rooms in technical development not yet being fully explored and optimized in terms of dimensional control of the nanorods and device assembly in this investigation. The results offer significant practical advantages in CdS nanorod-based solar cell device compared to those solar cells reported via the use of conventional hybrid composites.

# Chapter 7

## Annealing Effect in Photovoltaic Performance for Hybrid P3HT/Elongated CdS nanocrystal solar cells

### 7.1 Introduction

Recently, solar cells based on soluble conjugated polymers have attracted attention because conjugated polymers are promising materials for the development of low-cost optoelectronic devices [221, 181]. Organic photovoltaic cells using conjugated polymer/fullerene blends in a bulk heterojunction architecture have been reported with efficiencies up to 6.5% [182]. A bulk heterojunction is usually composed of two phases in the photoactive layer: fullerenes or nanocrystals for the acceptor phase and polymers for the donor phase. In a bulk heterojunction, the large interfacial area between the donor and acceptor phases provides sufficient charge separation, which is a prerequisite for solar-cell operation [183]. Upon irradiation, the conjugated polymer absorbs the photons and produces excitons. Exciton dissociation is known to occur at the interface between two materials with different excited-state energy levels; the electron will move to the lower excited-state energy level of the acceptor because it is energetically favorable. Upon irradiation the electrons from the excitons in the conjugated polymer transfer to the nanocrystals, and the holes from the excitons in the nanocrystals transfer to the conjugated polymer. The optimum overall performance of a bulk heterojunction cell can only be achieved by balancing the various requirements of photogeneration, transport, and extraction of charge carriers.

The bulk heterojunction system still has some difficulty achieving the 10%

power conversion efficiency (PCE) required for commercialization. The most serious problem is the difficulty of controlling the solid-state phase morphology of the two phases in the photoactive layer because the exciton diffusion length in conjugated polymers is typically between 5 and 10 nm [184, 185]. A variety of ideal photovoltaic structures have been proposed with interdigitated, pure phases spaced by a distance equal to or less than the exciton diffusion length. Some approaches to control donor/acceptor morphology have recently been reported, including the choice of spin-coating solvent [186, 187], slow drying of spin-coated films [28, 188], and controlled thermal annealing [189, 190]. Among them, thermal annealing is indispensable for complete solvent evaporation and phase separation for the bulk heterojunction formation, and this annealing greatly influences the evolution of the film morphology and device efficiency of hybrid cells in polymer/fullerene systems [104-106, 191]. For instance, Reyes-Reyes et al. reported that a significant improvement in the power conversion efficiency from 1.1% to 5% for P3HT-PCBM blends can be obtained by subjecting the sample to thermal annealing, even at low PCBM loading fractions [191], because annealing changes not only the film crystallinity but also the aggregation within the PCBM nanophase. However, only a few reports have focused on polymer/inorganic semiconductor composites. Olson et al. reported that phase separation is heavily influenced by nanocrystal ligand choice [192]. The ligands often dominate the electrical performance of the nanocrystals because they are generally insulators (alkyl chains) that impede charge transport between individual nanocrystals. The ligands can also play an important role in controlling the degree of nanocrystal aggregation, the limitation of which can improve charge transport [54]. Though surface ligands are insulators that prevent charge transport between nanocrystals, surfactants or ligands have been widely used in most literature reports in polymer or polymer/semiconductor hybrid systems. In other

words, there are very few reports in the literature in which no ligands were used to control or fabricate composites. An in-situ-growth of the polymer/semiconductor hybrid system could be developed without ligands in order to enhance the performance. In our previous report [193], we discussed the development of an in-situ growth of CdS/P3HT with different aspect ratios of CdS and demonstrated that the photovoltaic efficiency can be much enhanced by using a larger aspect ratio of CdS nanorods in the CdS/P3HT system.

However, as mentioned before, the efficiency and morphology of hybrid cells eare strongly influenced by thermal annealing because it is able to change the interaction or bonding between the P3HT polymer and the nanoparticles, which will affect the device performance. To effectively employ this ligand-free poly(3-hexylthiophene-2,5-dyl) (P3HT)/CdS nanocrystals with various nanocrystal ARs material system, it is imperative to understand the interaction of P3HT with the CdS nanocrystals and how it affects the blend morphology, phase separation and ultimately the photovoltaic device performance. The effect of annealing on the physical interaction between P3HT polymer and CdS nanocrystals was investigated on in-situ-grown P3HT/CdS nanocrystals systems with various nanocrystal ARs. The UV-vis results revealed the presence of a strong interaction between the P3HT and the CdS nanocrystals, which would further influence the extent of CdS aggregation in these blend films during the annealing process depending on the AR of CdS nanocrystals. This study on the annealing-condition-dependent PCE reveals that the polymer-nanocrystal interaction has a dramatic effect on the photovoltaic performance of hybrid solar cell devices.

## 7.2 Annealing effect on optical properties

Figure 7.1(a) shows the UV-Vis absorption spectra for the thin films of P3HT and the

P3HT/CdS composites with various ARs as spun cast on glass substrates. For the pure P3HT film, the solid-state absorption spectra showed two peaks at 521 nm and 556 nm and one shoulder at 605 nm. The shoulder at 605 nm is generally attributed to a higher crystallization or ordering of intra-chain interactions in semiconducting polymers and the peak intensity depends on the order degree in the intermolecular chains of the microcrystalline domains [103, 190]. These bands can be attributed to the $\pi$–$\pi$* transition [103]. As the AR of CdS nanocrystal increases, the absorption bands are blue-shifted. The shift of $\pi$–$\pi$* transition absorption peaks to shorter wavelength indicates an increasing density of conformational defects, which causes the loss of conjugation [194, 195]. This indicates that the blue shifts are due to the in-situ growth of CdS nanocrystals in the P3HT matrix, which induced the consequent destruction of the P3HT chain ordering during solvent evaporation. Figure 7.1(b) and 1(c) show the UV–vis spectra measured for P3HT/CdS (AR=4 and 16) films before and after annealing at different temperatures for 60 min. After thermal annealing, the spectra shifted towards longer wavelengths and the shoulder at 610 nm became more distinguishable when the annealing temperature increased because the interchain interaction between P3HT chains is stronger [103]. It is implied that the annealing treatments can improve ordering of P3HT chains.
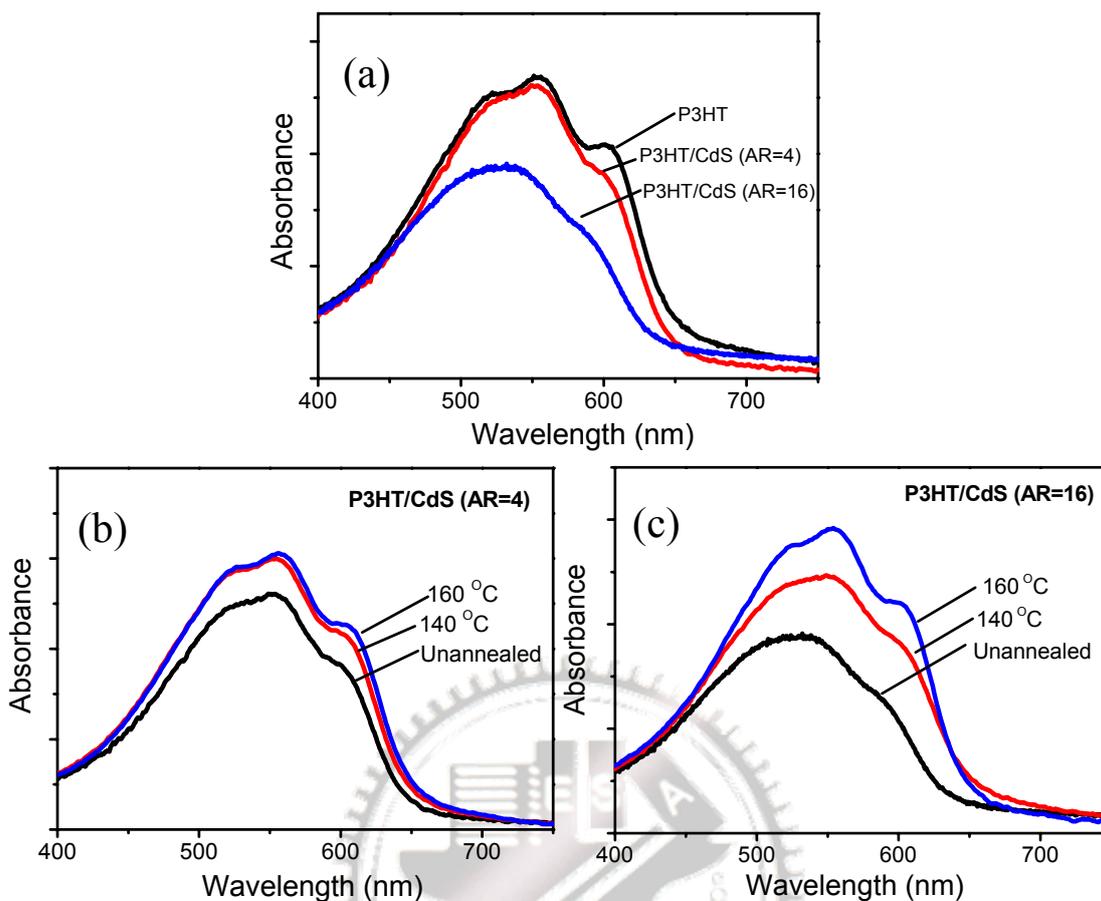
**Figure 7.1** (a) UV-Vis absorption spectra obtained for P3HT/CdS thin films with various ARs. UV-Vis absorption spectra of P3HT/CdS thin films with AR of (b) 4 and (c) 16 before and after annealing treatments.

The PL spectra in Figure 7.2 display the same trend, which supports this understanding of the structural variation of the P3HT/CdS composite film after annealing treatment. The PL intensity of the annealed sample was higher than that of the as-grown (or unannealed) samples. This indicates that the photo-induced electron transfer from the P3HT to CdS becomes less efficient upon annealing. The efficiency of electron transfer obviously depends on the mean distance between the conjugated polymer and CdS because the film thickness was much larger than the P3HT exciton diffusion length. The increase of the PL intensity on thermal annealing is consistent with an assumed increase in the size or number of P3HT crystallites with dimensions

73

larger than the exciton diffusion length, allowing for radiative relaxation rather than electron transfer at surrounding heterojunctions. Because the concentration of the CdS nanocrystals in the film does not change upon annealing, the change of the photoluminescence intensity should primarily originate from the CdS aggregation and the morphology evolution of the active layer. A larger increase in PL intensity was found for the P3HT/CdS composites with an AR of 4 (from line 1 to 3) than those with an AR of 16 (from line 4 to 6). This indicates that upon annealing, the photo-induced electron transfer from the P3HT to CdS for the CdS nanocrystals of AR=4 becomes less efficient than that with CdS nanocrystals of AR=16. Furthermore, the PL spectra of P3HT showed resolved vibronic structures at around 647 and 708 nm and found that Gaussian curves fit the PL curve well. The data of the Gaussian-fitting of the two peaks are shown in Table 1. The PL emission peak located at ~ 647 nm (1.92 eV) was assigned to the pure electronic transition and the peak at ~ 708 nm (1.75 eV) was assigned to the first vibronic band [196]. The red shifts in PL emission after annealing treatment suggest that the polymer chains are $\pi$-stacked on each other [94, 197]. The increase of the conformational order in the composites was attributed to the alignment of the polymer chains in the vicinity of nanocrystals during annealing treatments.
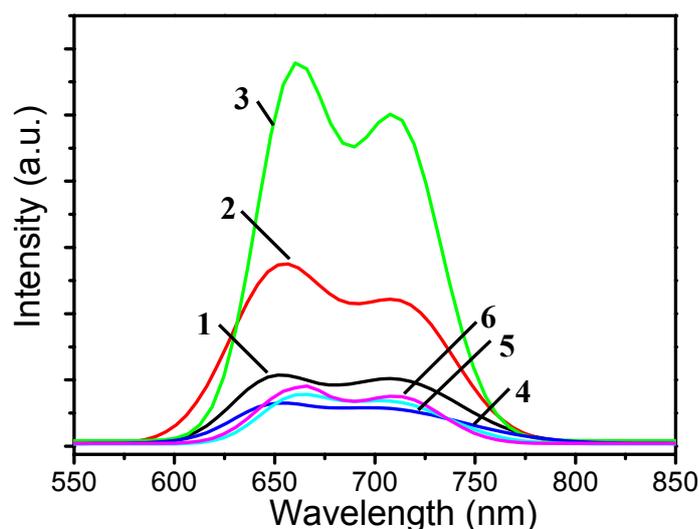
**Figure 7.2** The fluorescence spectra of P3HT/CdS nanocrystals with an AR of 4 and 16 before and after heat treatment. Line (1): AR=4, unannealed. Line (2): AR=4, 140 °C. Line (3): AR=4, 160 °C. Line (4): AR=16, unannealed. Line (5): AR=16, 140 °C. Line (6): AR=16, 160 °C.

**Table 3** PL measurement of the P3HT/CdS nanocrystals with different ARs.

|  | Annealing Temp. ($^O$C) | 0-0 transition (nm) | 0-1 transition (nm) |
|---|---|---|---|
| AR=4 | non | 647.6 | 708.7 |
|  | 140 | 651.5 | 713.6 |
|  | 160 | 658.8 | 713.7 |
| AR=16 | non | 645.7 | 700.2 |
|  | 140 | 657.5 | 706.4 |
|  | 160 | 659.7 | 711.9 |

## 7.3 AR effect on thermal properties

Figure 7.3 shows the DSC thermograms of pure P3HT and the P3HT/CdS nanocrystal composites. An exothermic peak showing the typical features of a melting transition

was detected for all the samples. The melting temperature of the P3HT/CdS nanocrystal composites depends on the crystallization conditions. The DSC data show that the exothermic peak was shifted to a lower temperature for the P3HT/CdS composites as compared to the pure P3HT, which is clear evidence of the influence of the CdS nanocrystals on the thermal properties. The shifting of the P3HT melting peak to a lower temperature indicates that the semi-crystalline nature of P3HT is partially hindered by CdS nanocrystals. We believe that the decrease in the crystallinity of the P3HT/CdS nanocrystal composites is related to the fact that the in-situ-grown CdS nanocrystals embedded between the P3HT chains inhibit the main-chain crystallization due to the strong interaction between the CdS nanocrystals and the P3HT [198]. Furthermore, it is noted that the P3HT/CdS nanocrystal composite with an AR=16 shows a larger shift than that with an AR of 4. This indicates that the degree of order in the P3HT is further reduced when the CdS of AR=16 is used. This observation, along with UV-vis absorption and PL measurements, indicates that on annealing, the growth of ordered polymer domains is more hindered by P3HT/CdS composites with an AR of 16. These differences from thermal annealing effects are important in the determination of the morphology of the device active layers and the improvement of the photovoltaic performance of P3HT/CdS composite-based solar cells.
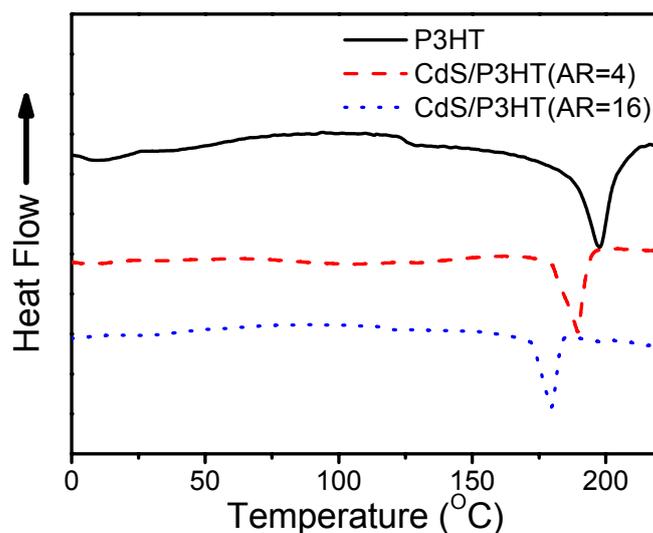
**Figure 7.3** DSC thermograms of pure P3HT and P3HT/CdS nanocrystals with an AR of 4 and 16 at a heating rate of 20 °C /min.

## 7.4 Annealing effect on photovoltaic performance

It is well known that the performances of photoactive layers based on P3HT/nanocrystal blends are usually enhanced when a thermal-annealing step is applied. Therefore, an optimization concerning the annealing temperature and duration was carried out for P3HT/CdS nanocrystals with an AR of 4 and 16. As shown in Figure 7.4, the device using the nanocrystals with an AR=16 shows a higher power conversion efficiency (PCE) as compared to that with an AR of 4 at different annealing conditions. Generally, for the photoactive layers consisting of equiaxial nanocrystals, electron transport is dominated by hopping. In contrast, for the photoactive layers consisting of elongated nanocrystals, the band conduction is prevalent in the P3HT/CdS composites [50] because nanorods with a high AR can penetrate through a large portion of the device to develop percolation pathways for electron transport. In other words, longer nanocrystals more easily form a percolation

77

path between two electrodes and can thus more fully contribute to photovoltaic conversion. Therefore, the PCE of the AR=16 composite is higher than that of the AR=4 composite because of more efficient charge transport.

In addition, the improved device performance depends heavily on the annealing conditions, as clearly seen in Figure 5. The devices annealed at 160 °C show the best performance, with efficiency as high as 1.5% (t=40 min) and 2.9% (t=60 min) for AR=4 and 16, respectively. This improvement is primarily attributed to the higher photon absorption and better crystallinity of the P3HT chains, as evidenced by the UV–vis spectra (Figure 2). However, as increasing the annealing temperature over 160 °C, it results in performance degradation, which can be explained by morphological changes and low structural stability at high temperatures.
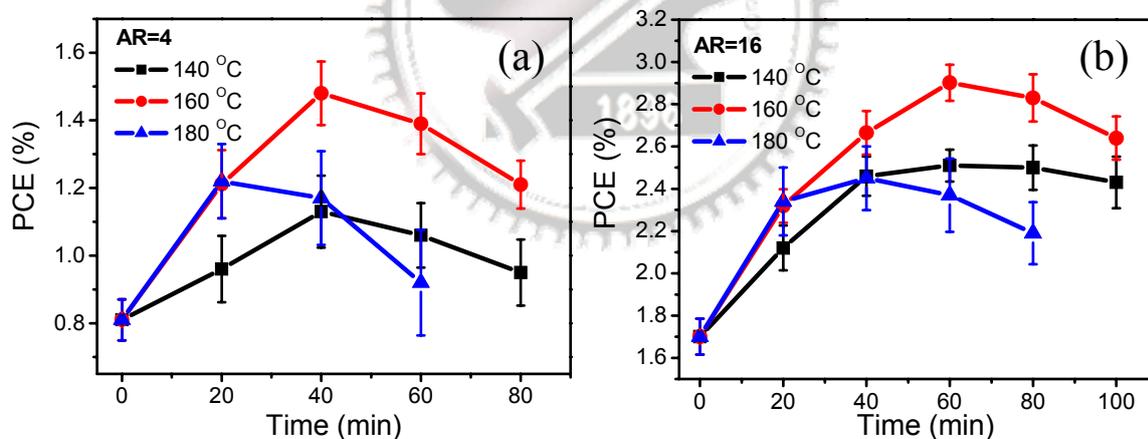


**Figure 7.4** Power conversion efficiency plotted as a function of annealing temperature and time.

## 7.5 Interaction between P3HT and CdS surface

Figure 7.5 shows the surface morphology change as monitored by AFM. The morphology can be further investigated for the origin of the long-term stability of P3HT/CdS devices with different annealing temperatures. For the as-deposited

(unannealed) film with AR=4 and 16, the surface is very smooth: the root mean square (rms) roughnesses are 1.067 nm and 1.184 nm, respectively. However, after thermal treatment at 160 °C, the rms roughnesses obtained from Figure 6(c) and 6(d) for AR=4 and 16 become 7.259 nm and 4.821 nm, respectively, because the CdS nanocrystals aggregate during thermal annealing. Moreover, it can be found that the scale of the aggregations for AR=4 is larger than that for AR=16, indicating that the CdS nanocrystals of AR=4 aggregate more easily than those of AR=16, which is in good agreement with the results of Figure 3. Compared with the film with AR=4, the film with AR=16 reveals rod-like texture due to a higher AR and smaller aggregations which consist of fewer CdS nanocrystals. As mentioned above, the best device performance and the highest PCE are obtained when the devices are annealed at 160 °C. Therefore, CdS nanocrystals aggregate excessively comparable to the exciting diffusion length, which leads to the reduced charge segregation and device efficiencies [199, 200].

(a)

(b)

(c)

(d)
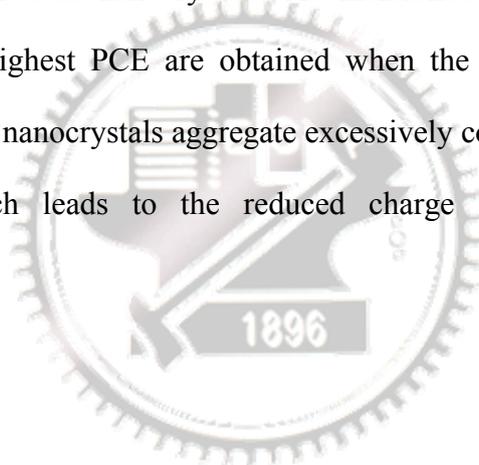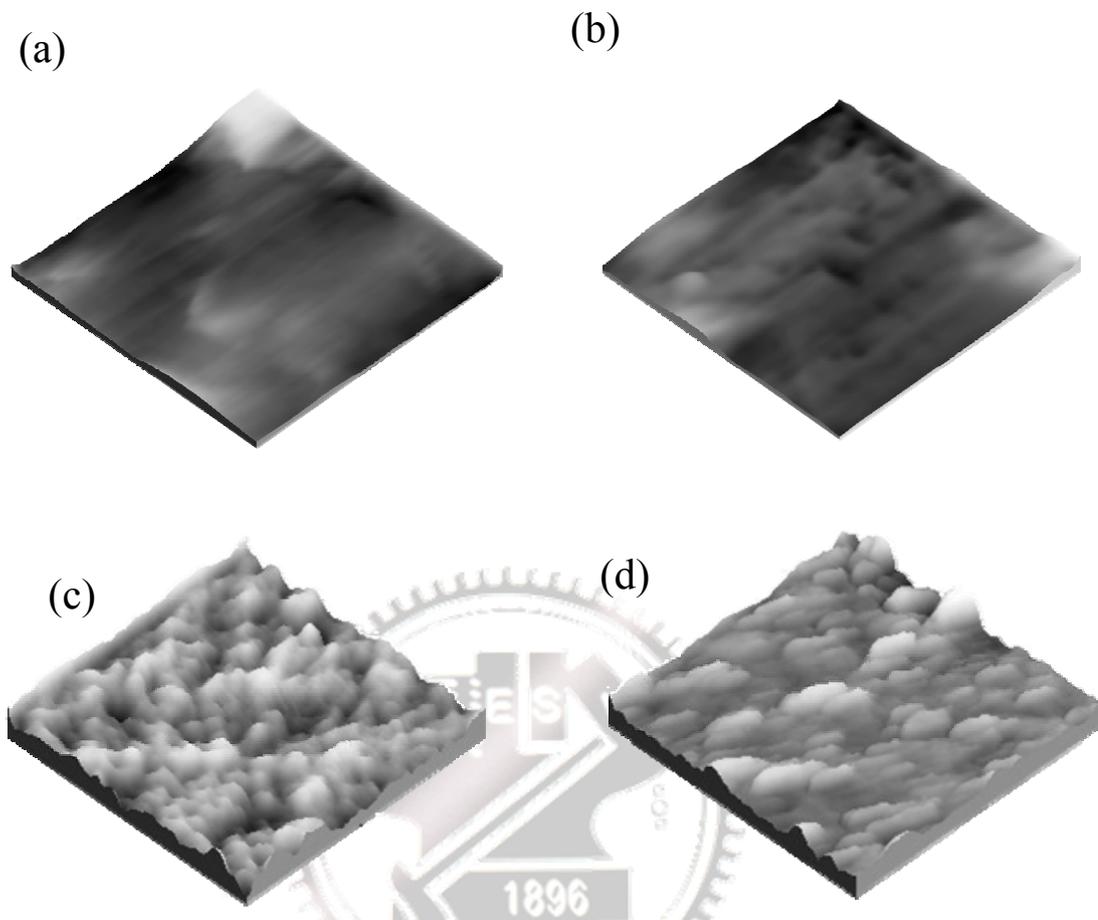
**Figure** AFM height images of P3HT/CdS films with (a) AR=4 and (b) AR=16. (c) AR=4 and (d) AR=16 annealed at 160 °C for 60 min.

To understand the interaction and molecular structure between P3HT and CdS nanocrystals during in-situ growth of P3HT/CdS, $^1$H NMR measurements were performed on the pristine P3HT and P3HT/CdS nanocrystals composites with an AR of 4 and 16. As shown in Figure 7(b) and 7(c), as compared to pure P3HT in Figure 7(a), it was found that the broader proton peaks at a chemical shift of ~6.98 (thiophene ring (a)) and ~2.79 ppm (hexyl chain (b)) were clearly observed for P3HT/CdS in Figure 7(b) and 6(c), which confirms that some interaction occurs between the polymer and the CdS. Additionally, the proton peaks from the hexyl chain (e) (~0.91 ppm) was only slightly broadened compared with the proton peaks

from the thiophene ring (a) and hexyl chain (b). A similar phenomenon also has been reported for polymer-CNT composites; the interactions of polymers with CNTs cause broadening and reduced intensity of ^{1}H NMR peaks [201, 202]. The closer the protons are to the surface of CNTs, the broader and weaker the peak will be. In addition, the degree of broadening in the peak corresponding to the thiophene ring is due to the corresponding protons coming very close to the nanoparticles [203]. This indicates that the thiophene ring is much closer to the CdS surface than the hexyl chain. This conclusion was further supported by the change of the relative intensity of proton peaks (a), (b), and (e). In the pristine P3HT solution, the ratio of protons (a), (b), and (e) is almost 1:2:3, whereas in P3HT/CdS, this ratio is ~0.94:1.89:3.0 and 0.85:1.73:3.0 for AR=4 and 16, respectively. As a result, although the polymer backbone interacts with the CdS surface, the hexyl chain is relatively free in solution. This is shown schematically in Figure 8(a), where the thiophene ring is in close spatial proximity to the CdS surface. Furthermore, a stronger adsorption between CdS nanoparticles and P3HT takes place at AR=16, indicating that the P3HT chain prefers to adsorb to a longer flat surface due to the planar P3HT conformation. This explains the observations made earlier on the basis of absorption and DSC spectra.
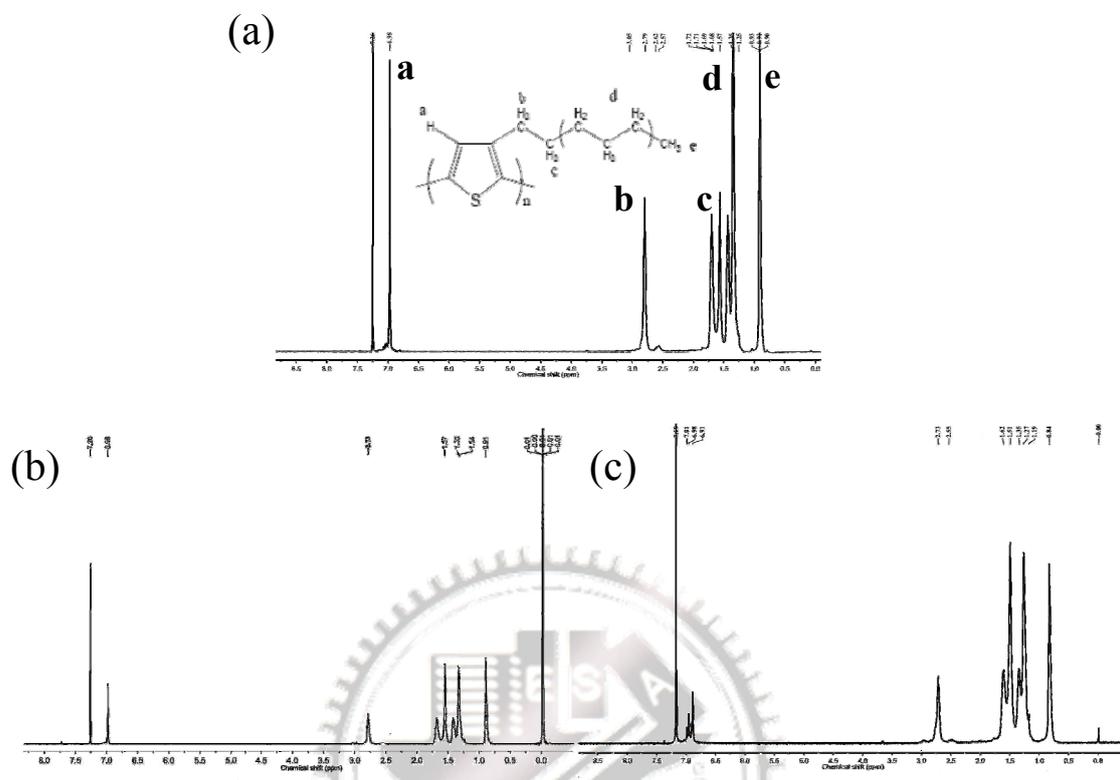
**Figure 7.6** $^1$H NMR spectra for (a) P3HT and P3HT/CdS composites with the AR of (b) 4 and (c) 16.

In previous reports [204], it has demonstrated that only a relatively small number of polymer segments within a chain are directly bound to the surface because of conformational limitations introduced by the particles, in addition to other restrictions on chain conformation as illustrate in Figures 7.7(b) and 7.7(c). For P3HT/CdS with AR=16, the polymer chain segments display a stronger interaction with the surface of the CdS, resulting in a denser layer and short loops close to the surface [205], as shown in Figure 7.7(b). On the contrary, the loops extend farther into the polymer matrix and form a region of lower density of polymer when AR is 4, as shown in Figure 7.7(c) [205]. It is noted that denser polymer chains can shield the surface from

other chains, likely resulting in a denser layer formed from fewer chains with fewer entanglements with other chains [204, 205]. Therefore, the strength of the interaction of a polymer molecule with the surface of the nanocrystals controls both the polymer molecular conformation at the surface and the entanglement distribution in a larger region surrounding the nanocrystal. Hence, a higher degree of entanglement will result in a larger number of polymer chains that are associated with a given nanocrystal, of which only a fraction is actually anchored to the surface. As a result, the strength of the interaction directly affects the aggregation rate of the CdS nanocrystals in the P3HT matrix during the annealing treatments, which causes the change in the morphology and the PCE (Figure 7.4 and 7.5).
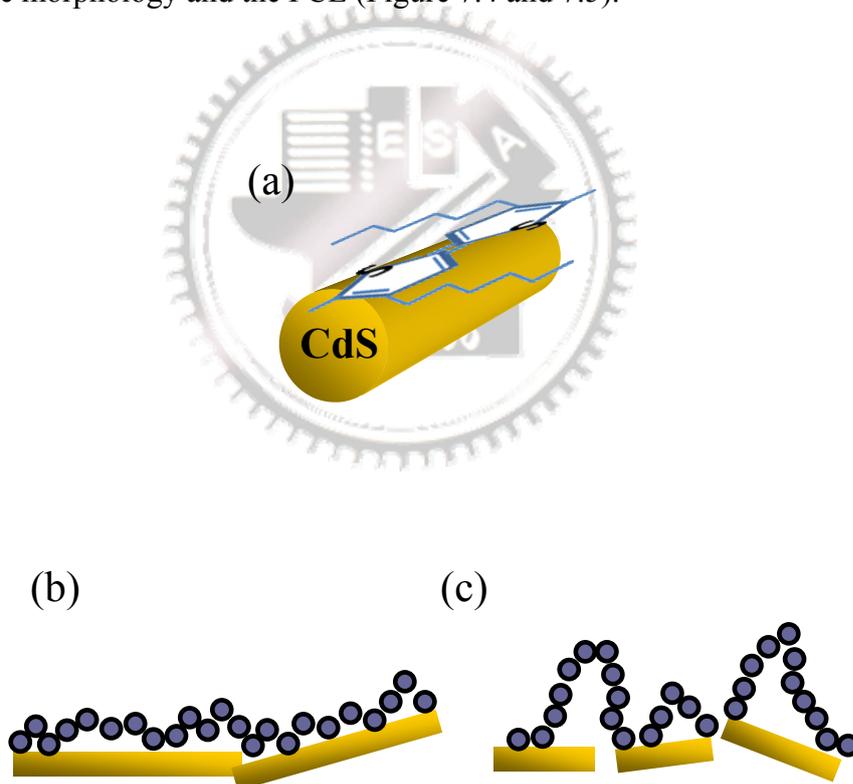


**Figure 7.7** (a) Schematic illustration of the molecular structure near the interface between CdS and P3HT, indicating the adsorption characteristics of polymer chains onto the surface of the nanoparticles. (b) A strong adsorption polymer adheres to the surface and most of the segments reside on the surface and (c) a weak adsorption polymer adheres to the surface and most of the segments reside in loops.

## 7.5 Summary

We prepared P3HT/CdS nanocrystal nanocomposites with different ARs by the in-situ method. Upon annealing Photoluminescence measurements confirmed the formation of polymer crystallites and also showed that the photo-induced electron transfer becomes effective as the AR increases. The $^1$H NMR results demonstrated that the thiophene ring is much closer to the CdS surface than the hexyl chain, and that the interaction strength between P3HT and CdS increases with the AR of the CdS nanocrystal. As a result, a lower AR drives the extensive aggregation of CdS in the polymer matrix upon annealing treatment, as evidenced by AFM. The annealing-condition-dependent PCE study revealed that this interaction shows not only a dramatic effect on the aggregation of nanocrystals during the annealing process but also device performance upon annealing. Therefore, a higher PCE (or Photovoltaic performance) can be obtained for the in-situ-growth P3HT/CdS with AR=16 upon annealing treatment at 160 °C for 60 min.

# Chapter 8

# Improvement in Photovoltaic Performance for Hybrid P3HT/elongated CdS nanocrystals solar cells with F-doped SnO$_2$ Arrays

## 8.1 Introduction

Organic photovoltaic devices are drawing attention because of their potential for the production of flexible and large-area solar cells at very low cost. Furthermore, polymer-inorganic hybrid solar cells are of particular interest because they combine the solution process ability of polymers with the high electron mobility of inorganic semiconductors [102]. Recently, hole-conducting polymers have been combined with a wide range of inorganic nanomaterials, including CdSe quantum dots, rods, tetrapods, hyper-branched colloids [50, 85, 87, 171] PbS, PbSe, CuInS$_2$ and CuInSe$_2$ nanoparticles [6,14, 53, 153, 206]. In general, the optimal device thickness of a bulk heterojunction solar cell is typically 100-200 nm, depending on the combination of materials. The optimal thickness is determined by the equilibrium between absorption of the films and charge carrier transport in the device. The amount of exciton generation increases with thickness because of a greater total absorption of light. However, the extent of recombination may also increase for very thick films due to the increased distance required for the charges to reach the electrodes, resulting in a decrease of overall power conversion efficiency. Therefore, a continuous ordered inorganic nanostructure that may help charge carrier collection and transport can potentially address this issue [107, 138, 156, 207]. For example, nanorod arrays not

only solve the above-mentioned problem, but also provide far greater surface area (over 100 times more) than thin films, which thus offer great advantages in applications where surface area plays a critical role in improving charge collection. As a result, it might be possible to achieve both large absorption and an efficient charge transport with thicker film devices. Therefore, the possibility of utilizing one-dimensional nanorods in both dye-sensitized solar cells and organic solar cells may help to boost device performance. This concept has already been attempted with ZnO and $TiO_2$ nanorods and nanotubes [8, 119, 140, 208, 209]. For instance, Olson et al. reported a P3HT/ZnO nanorod cell exhibiting a short-circuit current density ($J_{SC}$) of 2.2 mA/cm$^2$, an open-circuit voltage ($V_{OC}$) of 0.44 V, a fill factor (FF) of 0.56 and an efficiency of 0.53% using nanorods grown in basic conditions [8]. They also reported that the introduction of phenyl $C_{61}$-butyric acid methyl ester (PCBM) into the hybrid devices could significantly improve the efficiency of the devices by up to 2.03%. Nelson and Peiro´ et al. also reported hybrid photovoltaic devices using polymer/ZnO nanorod combinations [119, 140]. These reports revealed the importance of using nanorod array electrodes to improve the photovoltaic performance. However, up to now, very little work has been published regarding the fabrication of transparent conductive nanorods in solar cells [210, 211]. It is expected that increasing the interface area between the electrode and metal oxide will improve device performance by increasing charge capture. At present, indium tin oxide (ITO) has been the most commonly used plane anode in thin-film solar cells. Recently, Wang et al. produced ITO nanowires by electrophoretic deposition and demonstrated that nanowire electrodes could enhance the device performance of dye-sensitized solar cells [211]. We believe in the possibility of creating a nanostructured electrode to improve hybrid cell performance, especially if it can be achieved via simple and low-cost processes for the fabrication of oxide nanostructures.

Tin oxide, $SnO_2$ is an insulator and an important, colorless, low-cost, large-bandgap (n-type) semiconductor material. When doped with Sb or F ions, F-doped $SnO_2$ (FTO) is an ideal candidate for applications requiring a transparent conductive oxide due to its ability to adhere strongly to glass, resistance to physical abrasion, chemical stability, high optical visible transparency and electrical conductivity, such that FTO is widely used as a transparent conducting oxide substrate [212] as well as electrode material for energy conversion [213]. Recently, FTO nanorod electrodes developed by template-filling methods have been also demonstrated by Russo et al [214]. However, this method needs complex processes to remove the anodic alumina template. Therefore, in this study, a spray pyrolysis deposition process (SPD) was developed to obtain a good distribution of FTO film on ZnO nanorods grown using the aqueous solution method. The method not only makes it possible to coat ZnO nanorods with a thin, nominally uniform layer of FTO, but also controls the FTO thickness. In this study, it has been demonstrated that the efficiency of the P3HT/CdS/ZnO nanorod solar cell can be improved by nearly ~2 fold by coating the nanorod arrays in an FTO layer using SPD. Both ZnO nanorod length and FTO layer thickness had a crucial effect on the cell output characteristics. Moreover, we investigated effect of elongated CdS nanocrystals on the performance of FTO-coated ZnO nanorod polymer solar cells with a thick hybrid layer of CdS/P3HT.

## 8.2 Microstructure of FTO-coated ZnO nanorods

Figure 8.1(a) shows an FE-SEM image of the as-synthesized ZnO nanorods. The ZnO nanorods had a diameter that ranged from 80 to 90 nm and lengths of up to 380 nm depending on the growth conditions. The length of the ZnO nanorod increased with

the growth time, where the average length of the nanorods was estimated from the cross-sectional FE-SEM images (Figure 8.1(b)). The average length increased from ca. 140 to 380 nm by prolonging the growth reaction time from 90 to 180 min. Figure 8.1(c) show the image of ZnO nanorods coated with a 10 nm FTO layer by the spray pyrolysis deposition process (SPD). After the SPD process, the nanorods, as shown in the inset of Figure 8.1(c), exhibited increased diameters and rough surfaces as compared to those in Figure 8.1(a). This result indicates that FTO was successfully deposited on the ZnO nanorods. Figure 8.1(d) shows the X-ray diffraction (XRD) patterns of the FTO-coated ZnO nanorods and template ZnO nanorods. The distinct peaks corresponding to ZnO and $SnO_2$ were also observed, and the major diffraction peaks of the coating specimen were consistent with the known tetragonal $SnO_2$ structure with lattice constants given in the literature of a = 4.755 Å and c = 3.199 Å (JCPDS 41- 1445). Furthermore, it was noted that the peak of tetragonal $SnO_2$ (101) almost overlapped with the main peaks of ZnO (002). It was concluded that the coated FTO layers retained their perfect crystalline phase and physical structure, which further confirmed that an FTO layer rather than an alloy was formed. The broad peaks of $SnO_2$ in the XRD spectrum indicated that the nanoparticles were small. The average size of the nanoparticles as calculated by the Scherrer equation was about 9 nm. In addition, no obvious peaks corresponding to $SnCl_2$, Sn or other tin oxides were observed in the pattern.

Figure 8.2(a) shows a typical low-resolution TEM image of the FTO-coated ZnO nanorods. It was observed that almost all ZnO nanorods had been fully coated with thin and uniform layers. The thickness of the coating was estimated to be about 10 nm. The corresponding high-magnification TEM image in Figure 8.2(b) clearly shows that the FTO nanoparticles were crystalline and well-distributed on the nanorods. The inset of Figure 8.2(b) is the corresponding fast Fourier transform (FFT) diffraction pattern,

which can be indexed to tetragonal $SnO_2$. The two clear polycrystalline rings correspond to crystal faces of (110) and (101) of tetragonal $SnO_2$.

In order to optimize the FTO-coated ZnO nanorods for organic solar cells, ZnO nanorod arrays were grown for different periods of time by controlling the growth time. As demonstrated in Figure 8.1(b), the average length increased from 140 to 380 nm and the diameter of the nanorods was in the range of 80-90 nm for all cases, and almost independent of the reaction time. Figure 8.3(a) shows the TEM image of CdS/P3HT samples prepared at cadmium acetate concentrations of 0.83 mg/mL at 120 $^o$C with a DCB-to-DMSO ratio of 8:4 that demonstrated the size of CdS nanocrystals to be 2-3 nm. The structural morphologies of the CdS nanorods synthesized from the DCB-to-DMSO volume ratios of 7:5, 8:4 and 9:3 at a lower cadmium acetate concentration of 8.3 mg/mL for 30 min are shown in Figure 8.3(b), 3(c), and 3(d), respectively. It was found that a variation of the DCB-to-DMSO volume ratio from 7:5 to 8:4 to 9:3 at a lower cadmium acetate concentrations of 8.3 mg/mL gave CdSe nanocrystals with aspect ratios increasing from ~4 to ~8 to ~16 for the samples with the same concentration under similar reaction conditions, which is corresponding to the length of CdS about 9 nm, 18 nm, and 39 nm, respectively. The role of the structural direction of the P3HT template was demonstrated in our previous work [193]. An elongated P3HT chain can be developed by increasing the DCB-to-DMSO ratio, resulting in CdS nanocrystals with a higher aspect ratio.
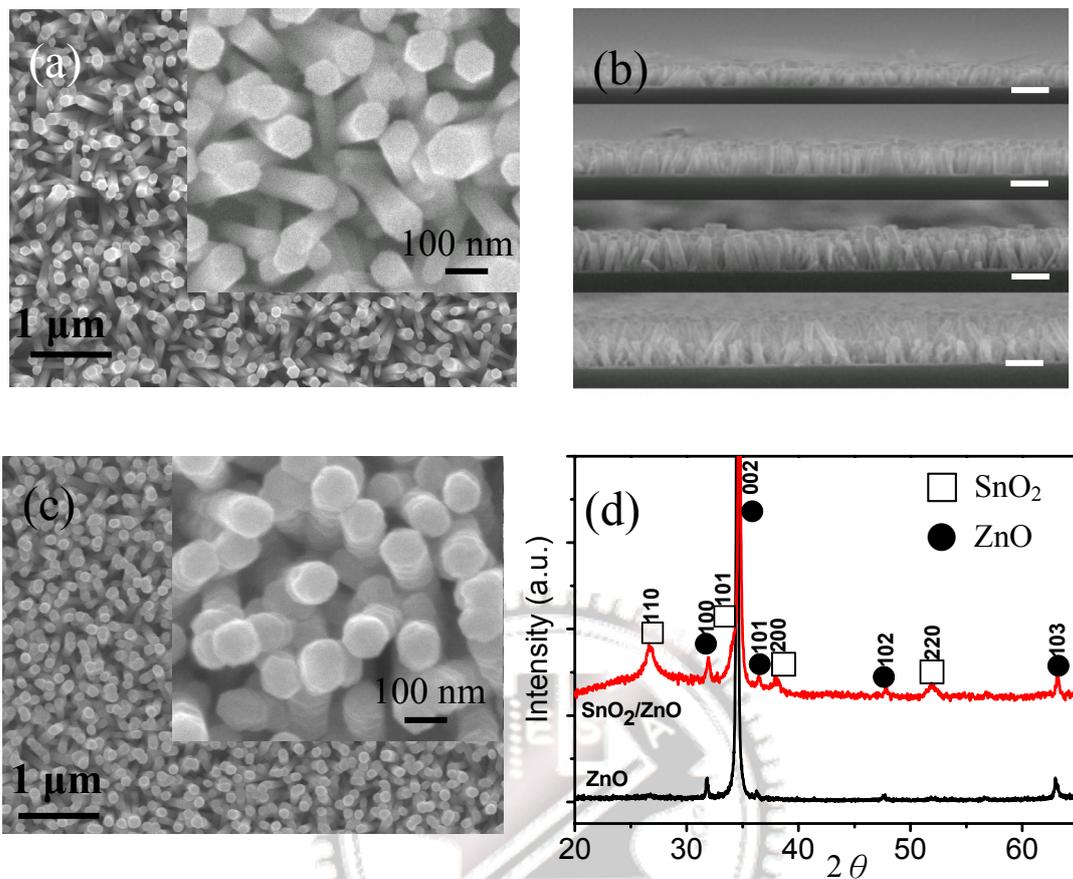
**Figure 8.1** FE-SEM images of (a) ZnO nanorods micrograph, (b) cross-sectional ZnO nanorods with various lengths, (c) ZnO nanorods coated with a 10 nm FTO layer. (d) XRD patterns of ZnO nanorods and ZnO nanorods coated with a 10 nm FTO layer. The scale bar in Figure 8.1(b): 300 nm.
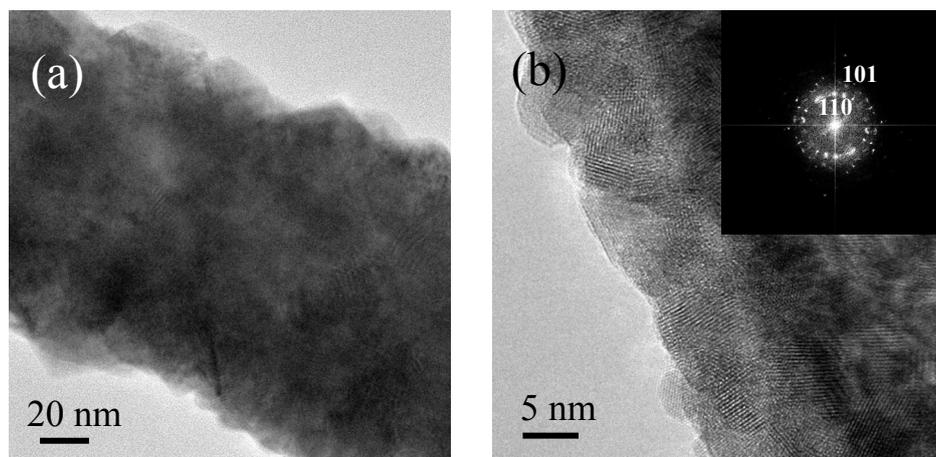


**Figure 8.2** (a) TEM image and (b) HRTEM micrograph of ZnO nanorods coated with a 10 nm FTO layer. The inset is the corresponding FFT diffraction pattern.
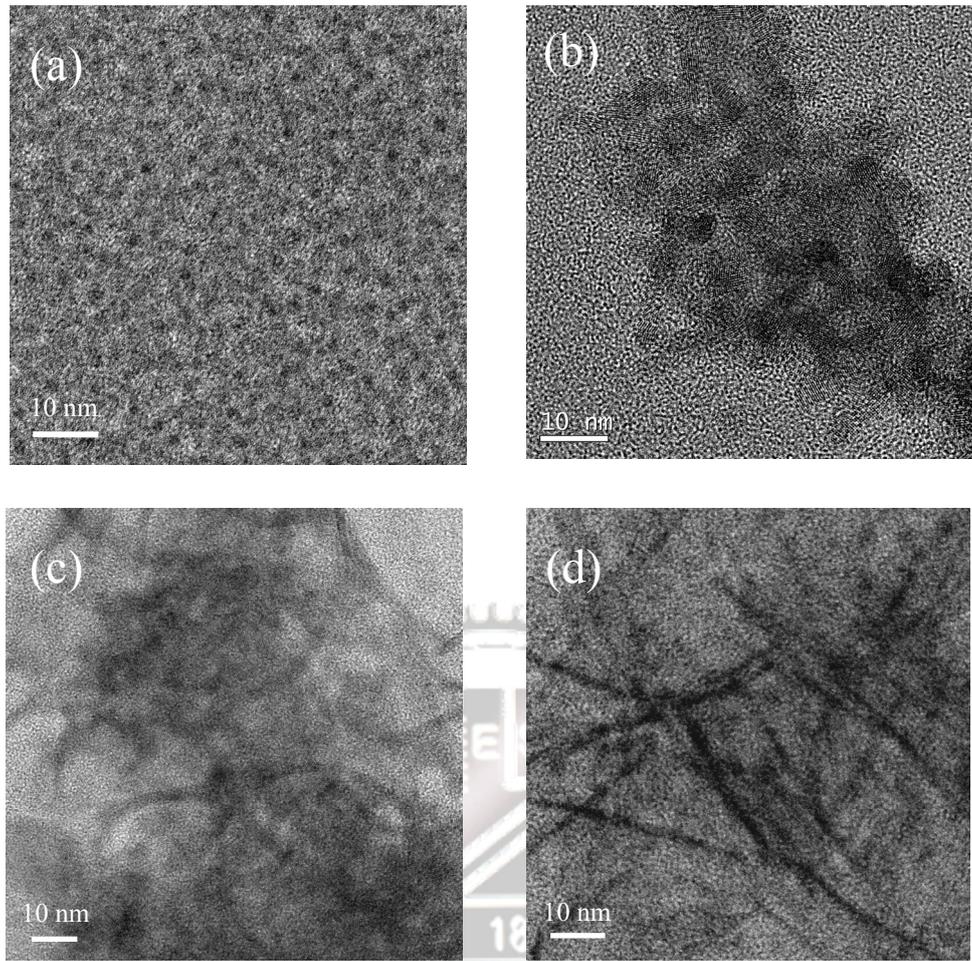
**Figure 8.3** (a) TEM image of CdS nanocrystals/P3HT composites synthesized at 120 $^o$C. TEM image of CdS nanocrystals synthesized in P3HT with a volume ratio of DCB-to-DMSO of (b) 7:3, (c) 8:4 and (d) 9:3 at 180 $^o$C.

## 8.3 Effect of ZnO nanorod length and FTO thickness

To investigate the dependence of the device performance on the length of the FTO-coated ZnO nanorods, power conversion efficiency (PCE), fill factor (FF), short circuit current density ($J_{SC}$) and open-circuit voltage ($V_{OC}$), a series of devices with 25 nm thickness FTO were prepared where the P3HT/CdSe had an aspect ratio of 1. Figures 8.4(a) and 8.4(b) illustrate the device performance as a function of the length of the FTO-coated ZnO nanorods. We observed that the device without nanorods showed a $J_{SC}$ of 3.8 mA cm$^{-2}$, a $V_{OC}$ of 0.56 V and a FF of 34%, resulting in a PCE of

0.70%. With the array with 320 nm FTO-coated ZnO nanorods, the PCE was improved to 1.8% under the same conditions as a result of the increased values for $J_{SC}$ of 6.8 mA cm$^{-2}$, $V_{OC}$ of 0.62 V and FF of 44%. The $J_{SC}$ increased strongly with the lengths of the nanorods. In addition, the FF was improved from 34% to 44% by introducing the FTO-coated ZnO arrays, although the improvement in $V_{OC}$ was small. The improvement in both $J_{SC}$ and FF mainly contributed to the increase of PCE from 0.70% to 1.8% as a result of the increase in the FTO-coated ZnO nanorod length. In our devices, the absorption layer was very thick (up to 450 nm), which improved the light absorption. However, when the nanorod was short, the probability of exciton recombination was higher with a thicker active layer due to the small carrier mobility. As the nanorod length increased, the average distance from the generation point of the charge carriers to the FTO electrode decreased, resulting in an increase in the number of charge carriers collected by the FTO-coated ZnO nanorods, which leads to an improvement of FF and $J_{SC}$. However, an increase in the nanorod length from 320 to 380 nm resulted in a decreased $J_{SC}$, which may be due to the annealing treatment being insufficient to drive P3HT to completely fill the volume between the longer nanorods [215]. Therefore, the ability to improve performance by efficient electron collection using longer nanorods may eventually be limited by issues with P3HT infiltration.

To further clarify the role of the CdS nanocrystals, a system without CdS in the P3HT layer was compared. As shown the inset of Figure 8.4(a), it was found that the incorporation of CdS into P3HT resulted in a large increase in $J_{SC}$ as compared with the device without CdS. This result demonstrates that the interface between the P3HT and FTO-coated ZnO nanorods makes a small contribution to the charge separation, and the charge separation mainly occurs at the P3HT/CdS interface. The reason for the more efficient charge separation at the P3HT/CdS interface could be attributed to

much larger interface area and large energy difference between P3HT and FTO. From the results above, we can conclude that these excitons are mainly dissociated to electrons and holes at the interface between P3HT and CdS, and that the FTO-coated ZnO nanorod array structure permits vertical charge transport from the active layer. Therefore, it is believed that the role of FTO-coated ZnO nanorod arrays in this study can be considered as an electron collector that collects the electrons more efficiently than a planar cathode structure.
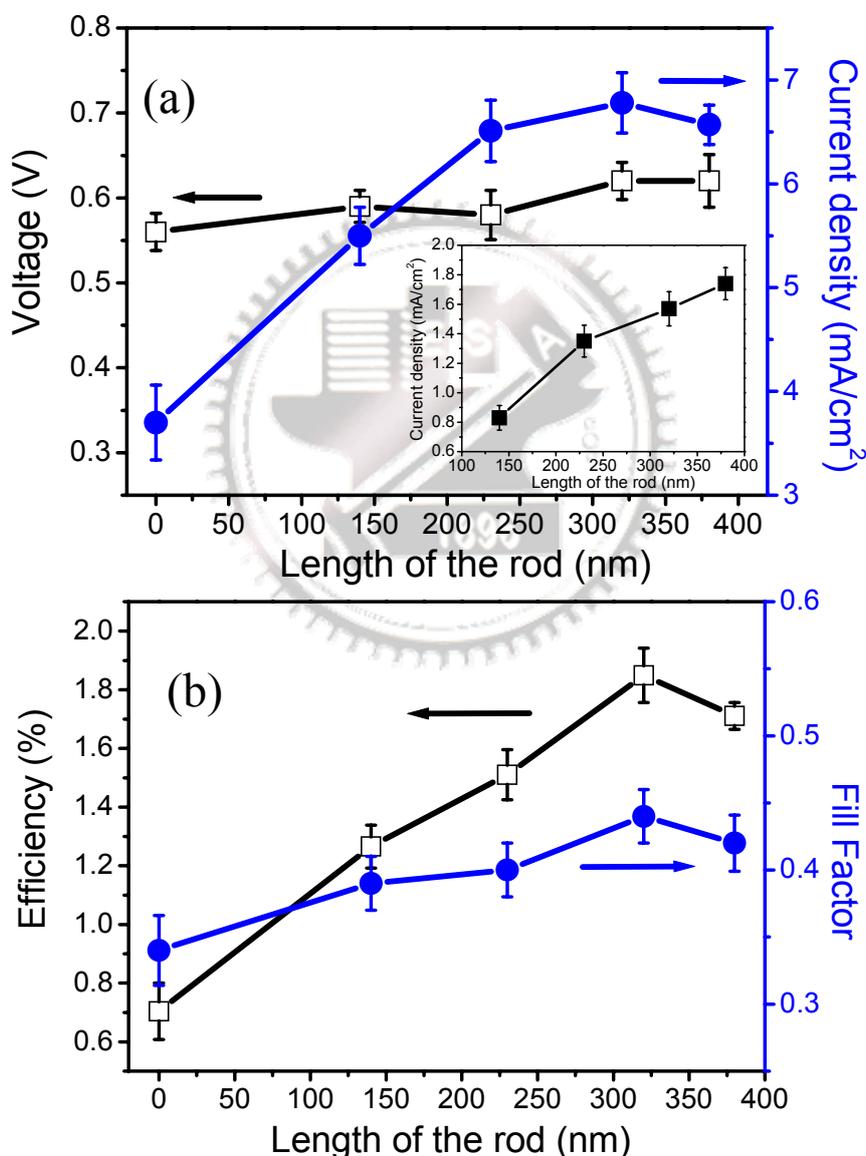


**Figure 8.4** Hybrid solar cell characteristics. (a) $V_{OC}$ and $J_{SC}$ (c) fill factor and PCE plotted as a function of nanorod length. The inset is $J_{SC}$ plotted as a function of nanorod length (without CdS nanocrystals).

After charge separation at the CdS/P3HT interface, the electrons generated at the conduction band of CdS (-4.0 eV) [216] can be transferred to the conduction band of $SnO_2$ (-4.4 eV) [216], which has a high electron mobility that helps charge-carrier collection and transport. Moreover, the conduction band of ZnO is slightly higher in energy than that of $SnO_2$, so the FTO layer dominates electron transport. Furthermore, because the $SnO_2$ has high electron mobility compared to most organic semiconducting materials, the electrons can be quickly collected by the FTO layer. Consequently, the FTO-coated ZnO nanorods work as electron collectors by shortening the average electron diffusion distance in the CdS network of the bulk heterojunction, resulting in a reduction in charge recombination.

To better understand the function of the FTO layer, we tested several devices with different thicknesses of the FTO layer. A nanorod length of 320 nm was used in all devices. Because the FTO layer dominates electron transport, the effect of the FTO thickness on the performance of the bulk heterojunction solar cells needed to be further clarified in this system. Figure 8.5 shows the current density (J) versus applied voltage (V) characteristics for several devices fabricated on FTO-coated ZnO nanorods with varying FTO thicknesses. It was found that the ZnO nanorod devices coated with 10, 25 and 40 nm exhibited an enhanced J-V response compared with the bare ZnO nanorod device. The FTO-coated ZnO nanorod devices showed a significantly higher $J_{SC}$ values but little change in the $V_{OC}$. It is well known that the $J_{SC}$ and the resultant resistances of the devices are obviously related to the FTO thickness. Table 4 summarizes the J–V characteristics and series resistance ($R_S$) of these devices as a function of FTO thickness. The devices with FTO layers show overall improvements in $R_S$ compared to those without the FTO layer. The $R_S$ was calculated from the inverse gradient of the J–V curve at 1 V under illumination. The $R_S$ reflects the ohmic loss in the entire device, which results from a combination of

the contact resistance and charge transfer rate at the interface. The Rs of the device varied with the FTO thickness, which implies that the measurement of series resistance supports the earlier inference. In the present case, the decrease in $R_S$ should be related to the reduction in contact resistance between the FTO layer and active organic layer, which provides a better conduction path to the electrons between the active organic layer and the cathode. Moreover, as reported previously in the literature, the mobility of the $SnO_2$ nanostructure (125 $cm^2$ $s^{-1}$ $V^{-1}$) [217] was orders of magnitude higher than that of single crystal ZnO (1-5 $cm^2$ $s^{-1}$ $V^{-1}$) [218]. This result implies that the photoinjected electrons in the FTO-coated ZnO nanorod cells will tend to travel in the thin FTO shells. In other words, the fastest pathway in these cells is mostly along the pathway of the FTO layer. The transport of electrons through $SnO_2$ is more energetically favorable than through ZnO, resulting in a decreased series resistance with increasing FTO thickness. Therefore, for the device with 25 nm FTO, the PCE was improved to 1.8% as a result of the increased values for $J_{SC}$ of 6.8 mA $cm^{-2}$, $V_{OC}$ of 0.62 V and FF of 44%. However, as the FTO thickness increased to 40 nm, the $J_{SC}$ decreased to 5.4 mA $cm^{-2}$. Figure 8.5 (b) shows normalized absorption spectra of ZnO nanorods coated with varying thicknesses of FTO layers. Compared with the absorption spectrum of the bare ZnO nanorod sample, the absorption spectrum of ZnO coated with a 40 nm FTO layer exhibited a blue shift. The blue shift suggested that some P3HT chain segments remain locked in a coiled configuration and are unable to be crystallized, resulting in a lower hole mobility of P3HT [219, 220]. A similar observation was also reported by Coakley et al., who demonstrated poorly ordered P3HT infiltration deep in the mesoporous structure due to the filtering effect [220]. This caused the photocurrent of this device to be limited by the transport of holes to the top electrode. Thus, holes undergo back recombination easier with an electron in the $TiO_2$ before escaping the polymer-$TiO_2$ region [107].
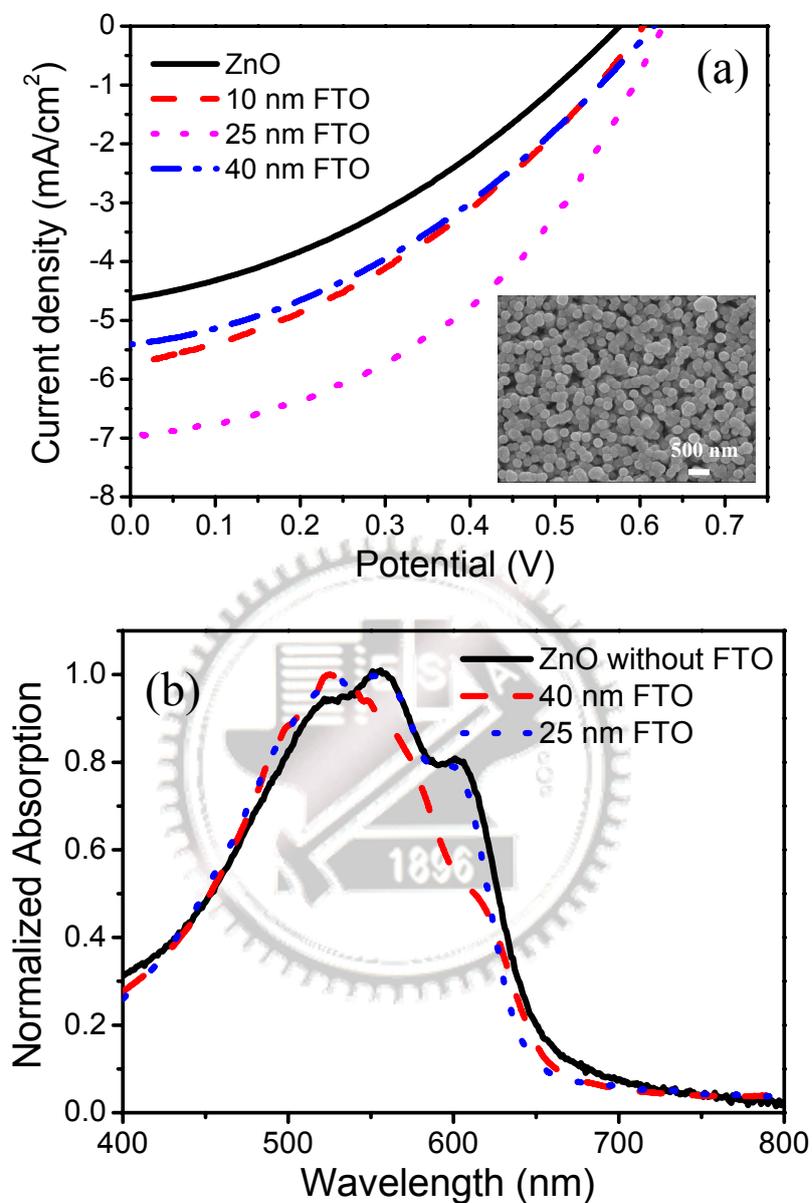
**Figure 8.5** (a) Current J-V curves of the photovoltaic devices with and without an FTO layer under 100 mW cm$^{-2}$ of AM1.5 irradiation. (b) CdS/P3HT absorption spectra following infiltration into the ZnO nanorods and FTO-coated ZnO nanorods.

**Table 4** Photovoltaic characteristics of devices fabricated on FTO-coated ZnO nanorods of various thicknesses. The series resistance ($R_S$) was extracted from the slopes of the $J-V$ curves at 1 V.

| FTO thickness (nm) | $V_{OC}$ (V) | $J_{SC}$ (mA/cm$^2$) | FF (%) | PCE (%) | $R_S$ ($\Omega$ cm) |
|---|---|---|---|---|---|
| 0 | 0.58 | 4.6 | 36 | 0.96 | 41 |
| 10 | 0.60 | 5.7 | 37 | 1.3 | 18 |
| 25 | 0.62 | 6.8 | 44 | 1.8 | 11 |
| 40 | 0.61 | 5.4 | 38 | 1.2 | 13 |

## 8.4 CdS nanocrystal effect

To investigate the role of the elongated CdS nanocrystals in the nanostructured electrode, we measured devices with various aspect ratios (AR) of CdS nanocrystals, where different nanorod lengths and FTO thickness were prepared for the study, as shown in Figure 8.6. Figure 8.6(a) shows the PCE of the devices fabricated with different FTO thicknesses plotted as a function of the AR of the CdS nanocrystals. It was noted that although the thickness of the FTO varied, the trends of the PCE were very similar. Compared to that of the devices without CdS, the incorporation of CdS into the P3HT enhanced the $J_{SC}$ and PCE. As shown in Figure 8.6(a), for the devices with an FTO thickness of 25 nm, the PCE was increased from 0.37% for P3HT without CdS to 1.8% with CdS of AR=1 (spherical shape). This result indicates that the addition of CdS plays a very important role in the enhanced $J_{SC}$. With a further increase in the AR of CdS to 4, the PCE was further increased up to 2.6%. A maximum PCE value appeared in the device with AR=4 for a ZnO nanorod length of 320 nm. When the AR exceeded 4, the PCE started to decrease due to the decreased $J_{SC}$. In addition, Figure 8.6(a) also demonstrates that the improvement in the performance of the devices also depended on the FTO thickness, which was explained

above. On the other hand, according to our previous study [193], it was demonstrated that the efficiency (and $J_{SC}$) of a P3HT/CdS nanocrystal device on a planar electrode can be increased by nearly two times at most by using elongated CdS nanocrystals (squares, Figure 8.6(b)). However, for the device with a nanorod length of 320 nm (circles, Figure 8.6(b)), upon increasing the aspect ratio of CdS nanocrystals from 1 to 4, the elongated CdS nanocrystals also contributed to the improved efficiency, resulting in the highest efficiency of 2.6%, but further increasing the AR to 8 and 16 caused a deterioration in efficiency. This phenomenon (or trend) is inconsistent with that of a planar electrode in our previous study [193]. We believed the nanorod array morphology limited it due to the incomplete penetration of elongated nanocrystals. The average nanorod density were estimated to be about $6 \times 10^9$ cm$^{-2}$ by FE-SEM images so the average distance between nanorods was ~80 nm. As the FTO thickness is 25 nm, the average distance between the nanorods decreased to ~30 nm, indicating it is difficult for longer nanocrystals to penetrate into between nanorods. Therefore, a maximum efficiency of the device appeared at the AR=4 (length ~9 nm) for the 320 nm ZnO nanorods. As a short length of 230 nm was used, it was found that the maximum efficiency of the device occurs at the CdS nanocrystals with an AR of 8 (length~18 nm) (triangles, Figure 8.6(b)). Furthermore, when an AR is above 8, the efficiency decreased slowly with increasing aspect ratio as compared to that with a nanorod length of 320 nm. Although the average distances between the nanorods were equal in calculation, the nanorods were not well-defined vertically; thus, the possibility of interlacing nanorods increases with nanorod length, resulting in more inaccessible internal space to the elongated CdS nanocrystals (not to the polymer). It can be supposed that the efficiency (or $J_{SC}$) is related to the penetration of elongated CdS nanocrystals among nanorods because the $V_{OC}$ of these devices remained almost constant when the AR was varied from 1 to 16. Here, for the devices with a nanorod

length of 320 nm, the best efficiency of 2.7 % was obtained. It was concluded that longer nanocrystals (e.g., AR=16) are more inaccessible to deeper space among nanorods. These results suggest that the maximum efficiency changes with not only the AR of the elongated nanocrystals, but also the nanorod array morphology.
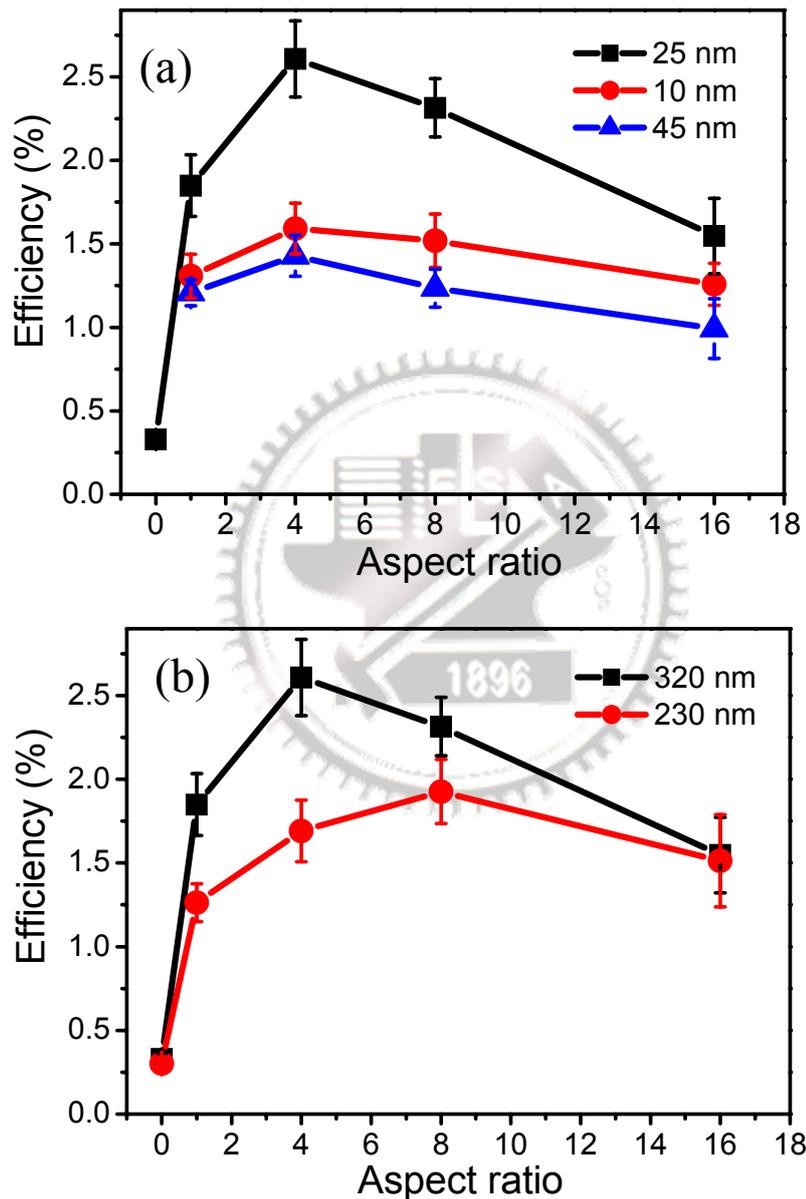


**Figure 8.6** (a) Efficiency of devices with different FTO thicknesses plotted as a function of the aspect ratio of CdS nanocrystals. (b) Efficiency of devices with different nanorod lengths plotted as a function of the aspect ratio of CdS nanocrystals.

## 8.5 Summary

Hybrid P3HT/elongated CdS nanocrystal photovoltaic devices using FTO-coated ZnO nanorod arrays as electrodes as a function of nanorod length, FTO thickness, and CdS aspect ratio have been well studied in this work. The performance of the hybrid photovoltaic devices was improved as the nanorod length was increased, suggesting that the introduction of the direct carrier transport electrode could enhance the performance of the photovoltaic devices. The FTO layer provided a better conduction path for electrons. As a result, in the case of spherical CdS (AR=1), the device fabricated from 320 nm ZnO nanorods with a 25 nm FTO layer showed the best efficiency of 1.8%. The use of elongated CdS nanocrystals with an AR of 4 made a large contribution to the improvement in PCE up to 2.6% but PCE started to decrease with a further increase in the AR, indicating the nanorod array morphology limited it due to the incomplete penetration of elongated nanocrystals. We believe that the use of current device architecture with nanorod array electrode provides a feasible way to enhance photovoltaic performance.

# Chapter 9

# Conclusions

- **MgO-coated ZnO nanorod arrays**

➢ Annealing at high temperatures (>700 °C) in $O_2$ atmospheres leads to Mg diffusion in ZnO and MgZnO alloy formation.

➢ A blue shift in the near-band-edge emission was observed as a result of the alloy band gap widening and the visible emission from the MgO-doped ZnO nanorods annealed at 800 °C in $H_2/N_2$ is centered at about 454 nm. In contrast, the visible emission from the MgZnO nanorods annealed $O_2$ is at 595 nm.

- **CdS QDs-decorated ZnO nanorod/P3HT hybrid solar cells**

➢ The $J_{SC}$ is highly related to the size of CdS QDs due to the improvement of electron injection efficiency but $V_{OC}$ also increases by decorating QDs but it is slightly dependent on the size of CdS QDs.

➢ A photovoltaic device based on the decorated-QD nanorod structure with P3HT polymer shows PCE over four times greater than that for a similar device without QDs. The best power conversion efficiency is 0.21% (100 mW $cm^{-2}$).

- **In-situe synthesis of P3HT/CdS nanocomposites and hybrid solar cells**

➢ Formation of CdS nanorods and the corresponding variation of the aspect ratio of the nanorods can be well manipulated via a soft templating technology using the planar P3HT polymer, as a molecular template upon synthesis.

➢ The charge transport is considerably enhanced by using the CdS nanorods with higher aspect ratio and thus the best PCE is as high as 2.9% when the aspect ratio is 16.

➢ The $^1$H NMR results demonstrated that the thiophene ring is much closer to the CdS surface than the hexyl chain, and that the interaction strength between P3HT

and CdS increases with the AR of the CdS nanocrystal.

➢ The annealing-condition-dependent PCE study revealed that this interaction has a dramatic effect on the aggregation of nanocrystals during the annealing processes.

➢ The interaction strength dependence on the AR correlates directly to the CdS aggregation rate and thus influences the maintenance device performance upon annealing.

● **P3HT/CdS hybrid solar cells with F-doped SnO$_2$ array**

➢ The performance of the hybrid photovoltaic devices was improved as the nanorod length was increased because the introduction of the direct carrier transport electrode could enhance the performance of the photovoltaic devices.

➢ In the case of spherical CdS (AR=1), the device fabricated from 320 nm ZnO nanorods with a 25 nm FTO layer showed the best efficiency of 1.8%.

➢ The use of elongated CdS nanocrystals with an AR of 4 made a large contribution to the improvement in PCE up to 2.6% but PCE started to decrease because the nanorod array morphology limited it due to the incomplete penetration of elongated nanocrystals.

● **CdS-pHEMA Hybrid**

➢ The hybrid is synthesized using an in-situ polymerization following an in-situ chemical reduction, where the resulting particle size and the distribution of CdS nanocrystals can be narrowly manipulated.

➢ The hybrids, containing a relatively small amount of the CdS NCs, exhibit a pronounced photoluminescence spectrum shift when in contact with a number of dielectric liquids and such a pronounced dielectric-confinement effect has been experimentally verified and modeled.

➢ It is envisioned that this novel hybrid can be used as a functional materials for

chemical sensing applications via a change in its optical appearance and/or photoluminescence emission spectra as a result of dielectric stimulus.

# References

[1] J. Zhao, A. Wang, P. Altermatt, M. A. Green, Twenty-four percent efficient silicon solar cells with double layer antireflection coatings and reduced resistance loss, *Appl. Phys. Lett.* **1995**, 66, 3636.

[2] J. Zhao, A. Wang, M. A. Green, F. Ferrazza, 19.8% efficient "honeycomb" textured multicrystalline and 24.4% monocrystalline silicon solar cells, *Appl. Phys. Lett.* **1998**, 73, 1991.

[3] C. B. Murray, D. J. Norris, M. G. Bawendi, Synthesis and characterization of nearly monodisperse CdE (E=sulfur, selenium, tellurium) semiconductor nanocrystallites, *J. Am. Chem. Soc.* **1993**, 115, 8706.

[4] X.G. Peng, J. Wickham, A.P. Alivisatos, Kinetics of II-VI and III-V Colloidal Semiconductor Nanocrystal Growth: "Focusing" of Size Distributions, *J. Am. Chem. Soc.* **1998**, 120, 5343.

[5] X. G. Peng, L. Manna, W. D. Yang, J. Wickham, E. Scher, A. Kadavanich, A.P. Alivisatos, Shape control of CdSe nanocrystals, *Nature* **2000**, 404,59.

[6] P. W. C. Zhang, S. A. McDonald, G. Kostantatos, E. H. Sargent, Enhanced infrared photovoltaic efficiency in PbS nanocrystal/semiconducting polymer composites: 600-fold increase in maximum power output via control of the ligand barrier, *Appl. Phys. Lett.* **2005**, 87, 233101.

[7] S. E. Shaheen, D. S. Ginley, G. E. Jabbour, Organic-based photovoltaics toward low-cost power generation, *MRS Bull.* **2005**, 30, 10.

[8] D. C. Olson, J. Piris, R. T. Collins, S. E. Shaheen and D. S. Ginley, Hybrid photovoltaic devices of polymer and ZnO nanofiber composites, *Thin Solid Films* **2006**, 496, 26.

[9] P. Ravirajan, A. M. Peiró, M. K. Nazeeruddin, M. Graetzel, D. D. C. Bradley, J. R. Durrant, and J. Nelson, Hybrid Polymer/Zinc Oxide Photovoltaic Devices

with Vertically Oriented ZnO Nanorods and an Amphiphilic Molecular Interface Layer, *J. Phys. Chem. B* **2006**, 110, 7635.

[10] J. Rotalsky, D. Meissner, Photocurrent spectroscopy for the investigation of charge carrier generation and transport mechanisms in organic p/n-junction solar cells, *Sol. Energ. Mat. Sol. Cells* **2000,** 63, 37.

[11] C. W. Tang In, US Patent, **1979**, p 4,164,431.

[12] G. Yu, K. Pakbaz, and A. J. Heeger, Semiconducting polymer diodes: Large size, low cost photodetectors with excellent visible-ultraviolet sensitivity, *Appl Phys Lett.* **1994**, 64, 3422.

[13] J. Boucle, P. Ravirajan, Nelson, Hybrid polymer–metal oxide thin films for photovoltaic applications, *J. Mater Chem* **2007**, 17, 3141.

[14] E. Arici, N.S. Sariciftci, D. Meissne, Hybrid Solar Cells Based on Nanoparticles of CuInS2 in Organic Matrices, *Adv. Funct. Mater.* **2003**, 13, *165*.

[15] H. Weller, Colloidal Semiconductor Q-Particles: Chemistry in the Transition Region Between Solid State and Molecules, *Angew. Chem., Int. Ed. Engl.* **1993**, *32*, 41.

[16] A. Moliton, J. M. Nunzi, How to model the behaviour of organic photovoltaic cells**,** *Polym Int* **2006**, 55, 583.

[17] S. C. J. Meskers, J. Hübner, M. Oestreich, and H. Bässler, Dispersive Relaxation Dynamics of Photoexcitations in a Polyfluorene Film Involving Energy Transfer: Experiment and Monte Carlo Simulations, *J. Phys. Chem. B* **2001**, 105, 9139.

[18] G. G. Malliaras, J. R. Salem, P. J. Brock, and J. C. Scott, Photovoltaic measurement of the built-in potential in organic light emitting diodes and photodiodes, *J. Appl. Phys.* **1998**, 84, 1583.

[19] A. M. Cowley and S. M. Sze, Surface States and Barrier Height of Metal

Semiconductor Systems, *J. Appl. Phys.* **1965**, 36, 3212.

[20] C. J. Brabec, A. Cravino, D. Meissner, N. S. Sariciftci, T. Fromherz, M. T. Rispens, L. Sanchez, J. C. Hummelen, Origin of the Open Circuit Voltage of Plastic Solar Cells, *Adv. Funct. Mater.* **2001**, 11, 374.

[21] H. Frohne, S.E. Shaheen, C. J. Brabec, D. C. Muller, N. S. Sariciftci, K. Meerholz, Influence of the Anodic Work Function on the Performance of Organic Solar Cells, *ChemPhysChem* **2002**, 3, 795.

[22] C. J. Brabec, Organic photovoltaics: technology and market, *Sol. Energy Mater. Sol. Cells* **2004**, 83, 273.

[23] J. Liu, Y. Shi, Y. Yang, Solvation-Induced Morphology Effects on the Performance of Polymer-Based Photovoltaic Devices**,** *Adv. Funct. Mater.* **2001**, 11, 420.

[24] T. J. Savenije, J. M. Warman, A. Goossens, Visible light sensitisation of titanium dioxide using a phenylene vinylene polymer, *Chem. Phys. Lett.* **1998**, 287, 148.

[25] A. F. Nogueira, I. Montanari, J. Nelson, J. R. Durrant, C. Winder, N. S. Sariciftci, C. J. Brabec, Charge Recombination in Conjugated Polymer/Fullerene Blended Films Studied by Transient Absorption Spectroscopy, *J. Phys. Chem. B* **2003**, 107, 1567.

[26] S. A. Choulis, J. Nelson, Y. Kim, D. Poplavskyy, T. Kreouzis, J. R. Durrant, D. Bradley, Investigation of transport properties in polymer/fullerene blends using time-of-flight photocurrent measurements, *Appl. Phys. Lett.* **2003**, 83, 3812.

[27] H. J. Snaith, A. C. Arias, A. C. Morteani, C. Silva, R. H. Friend, Charge Generation Kinetics and Transport Mechanisms in Blended Polyfluorene Photovoltaic Devices, *Nano Lett.* **2002**, 2, 1353.

[28] S. E. Shaheen, C. J. Brabec, N. S. Sariciftci, F. Padinger, T. Fromherz, J. C. Hummelen, 2.5% efficient organic plastic solar cells, *Appl. Phys. Lett.* **2001**, 78,

841.

[29] J. Kroom, M. Wienk, W. Verhees, J. Hummelen, Accurate efficiency determination and stability studies of conjugated polymer/fullerene solar cells, *Thin Solid Films* **2002**, 403–404, 223.

[30] G. Yu, A.J. Heeger, Charge separation and photovoltaic conversion in polymer composites with internal donor/acceptor heterojunctions, *J. Appl. Phys.* **1995**, 78, 4510.

[31] J. Yu, D.H. Hu, P.F. Barbara, Unmasking Electronic Energy Transfer of Conjugated Polymers by Suppression of $O_2$ Quenching, *Science* **2000**, 289, 327.

[32] D.S. Ginger, N.C. Greenham, Charge transport in semiconductor nanocrystals, *Synth. Met.* **2001**, 124, 117.

[33] D. S. Ginger, N. C. Greenham, Photoinduced electron transfer from conjugated polymers to CdSe nanocrystals, *Phys. Rev. B* **1999**, 59, 10622.

[34] Y. G. Kim, B. C. Thompson, N. Ananthakrishnan, G. Padmanaban, S. Ramakrishnan, J. R. Reynolds, Focus Section: Variable band gap conjugated polymers for optoelectronic and redox applications, *J Mater Res* **2005**, 20, 3188.

[35] R. J. Kline, M. D. McGehee, E. N. Kadnikova, J. Liu, J. M. J. Fréchet, and M. F. Toney, Dependence of Regioregular Poly(3-hexylthiophene) Film Morphology and Field-Effect Mobility on Molecular Weight, *Macromolecules* **2005**, 38, 3312.

[36] Z. Bao, A. Dodabalapur, A. Lovinger, Soluble and processable regioregular poly(3-hexylthiophene) for thin film field-effect transistor applications with high mobility, *Appl. Phys. Lett.* **1996**, 69, 4108.

[37] H. Sirringhaus, N. Tessler, R. Friend, Integrated optoelectronic devices based on conjugated polymers, *Science* **1998**, 280, 1741.

[38] L. Bozano, S.A. Carter, J.C. Scott, G.G. Malliaras, P.J. Brock, Temperature- and field-dependent electron and hole mobilities in polymer light-emitting diodes,

*Appl. Phys. Lett.* **1999,** 74, 1132.

[39] A. Babel, S. Jenekhe, Electron Transport in Thin-Film Transistors from an n-Type Conjugated Polyme, *Adv. Mater.* **2002**, 14, 371.

[40] R. D. McCullough, R.D. Lowe, Enhanced electrical conductivity in regioselectively synthesized poly(3-alkylthiophenes), *J. Chem. Soc. Chem. Commun.* **1992**, 70.

[41] X. Wu, T. Chen, R.D. Rieke, Synthesis of Regioregular Head-to-Tail Poly[3-(alkylthio)thiophenes]. A Highly Electroconductive Polymer, *Macromolecules* **1996,** 29, 7671.

[42] H. Sirringhaus, P.J. Brown, R. Friend, M.M. Nielsen, K. Bechgaard, B.M.W. Langeveld-Voss, A.J.H. Spiering, R.A.J. Janssen, E.W. Meijer, Microstructure–mobility correlation in self-organised, conjugated polymer field-effect transistors, *Synth. Met.* **2000**, 111–112, 29.

[43] X. Jiang, R. Patil, Y. Harima, J. Ohshita, A. Kunai, Influences of Self-Assembled Structure on Mobilities of Charge Carriers in π-Conjugated Polymers, *J. Phys. Chem. B* **2005**, 109, 221.

[44] G. Juska, K. Arlauskas, R. Osterbacka, H. Stubb, Time-of-flight measurements in thin films of regioregular poly(3-hexyl thiophene), *Synth. Met.* **2000**, 109, 173.

[45] A. N. Aleshin, H. Sandberg, H. Stubb, Two-dimensional charge carrier mobility studies of regioregular P3HT, *Synth. Met.* **2001**, 121, 1449.

[46] A. Assadi, C. Svensson, M. Willander, O. Inganas, Field-effect mobility of poly(3-hexylthiophene), *Appl. Phys. Lett.* **1988**, 53, 195.

[47] J. Paloheimo, P. Kuivalainen, H. Stubb, E. Vuorimaa, D.Y. Lahti, Molecular field-effect transistors using conducting polymer Langmuir–Blodgett films, *Appl. Phys. Lett.* **1990**, 56, 1157.

[48] H. Sirringhaus, P. J. Brown, R. H. Friend, M. M. Nielsen, K. Bechgaard, B. M.

W. Langeveld-Voss, A. J. H. Spiering, R. A. J. Janssen, E. W. Meijer, P. Herwig, D. M. de Leeuw, Two-dimensional charge transport in self-organized, high-mobility conjugated polymers, *Nature* **1999**, 401, 685.

[49] A. P. Alivisatos, Semiconductor clusters, nanocrystals, and quantum dots, *Science* **1996,** 271, 933.

[50] W. Huynh, J. Dittmer, A. P. Alivisatos, Hybrid Nanorod-Polymer Solar Cells, *Science* **2002**, 295, 2425.

[51] W. Huynh, X. Peng, A. P. Alivisatos, CdSe Nanocrystal Rods/Poly(3-hexylthiophene) Composite Photovoltaic Devices, *Adv. Mater.* **1999**, 11, 923.

[52] N. C. Greenham, X. Peng, A. P. Alivisatos, Charge separation and transport in conjugated-polymer/semiconductor-nanocrystal composites studied by photoluminescence quenching and photoconductivity, *Phys. Rev. B* **1996**, 54, 17628.

[53] S. McDonald, G. Konstantatos, S. Zhang, P. W. Cyr, E. J. D. Klem, L. Levina, H. Sargent, Solution-processed PbS quantum dot infrared photodetectors and photovoltaics, *Nat. Mater.* **2005**, 4, 138.

[54] E. Arici, D. Meissner, F. Schäffler, N. S. Sariciftci, Core/shell nanomaterials in photovoltaics, *Int. J. Photoenergy* **2003**, 4, 199

[55] M. L. Steigerwald, L. Eisrus, Semiconductor crystallites: a class of large molecules, *Acc. Chem. Res.* **1990**, 23, 183.

[56] S. A. Empedocles, M. G. Bawendi, Spectroscopy of Single CdSe Nanocrystallites, *Acc. Chem. Res.* **1999**, 32, 389.

[57] C. J. Murphy, J. L. Coffer, Quantum Dots: A Primer, *Appl. Spectr.* **2002**, 56, 16A.

[58] M. Green, Third generation photovoltaics: Ultra-high conversion efficiency at

low cost, *Progr. Photovolt.* **2001**, 9, 123.

[59] M. Green, Third generation photovoltaics: solar cells for 2020 and beyond, *Physica E* **2002**, 14, 65.

[60] C. T. Black, C. B. Murray, R. L. Sandstrom, S. Sun, Spin-Dependent Tunneling in Self-Assembled Cobalt-Nanocrystal Superlattices, *Science* **2000**, *290*, 1131

[61] S. Günes, K. P. Fritz, H. Neugebauer, N. S. Sariciftci, S. K. and G. D. Scholes, Hybrid solar cells using PbS nanoparticles, *Sol. Energy Mater*. *Sol. Cells* **2006**, *91*, 420.

[62] Z. A. Peng, X. G. Peng, Mechanisms of the Shape Evolution of CdSe Nanocrystals, *J. Am. Chem. Soc.* **2001**, 123, 1389.

[63] Z. A. Peng, X. G. Peng, Nearly Monodisperse and Shape-Controlled CdSe Nanocrystals via Alternative Routes:  Nucleation and Growth, *J. Am. Chem. Soc.* **2002**, 124, 3343.

[64] W. U. Huynh, J. J. Dittmer, W. C. Libby, G. L. Whiting, A. P. Alivisatos, Controlling the Morphology of Nanocrystal-Polymer Composites for Solar Cells, *Adv. Funct. Mater.* **2003**, 13, 73.

[65] L. Manna, E.C. Scher, A. P. Alivisatos, Synthesis of Soluble and Processable Rod-, Arrow-, Teardrop-, and Tetrapod-Shaped CdSe Nanocrystals, *J. Am. Chem. Soc.* **2000**, 122, 12700.

[66] A. Fiore, R. Mastria, M. G. Lupo, G. Lanzani, C. Giannini, E. Carlino, G. Morello, M. De Giorgi, Y. Li, R. Cingolani, L. Manna, Tetrapod-Shaped Colloidal Nanocrystals of II−VI Semiconductors Prepared by Seeded Growth, *J. Am. Chem. Soc.* **2009**, 131, 2274.

[67] Y. W. Jun, S. M. Lee, N. J. Kang, J. W. Cheon, Controlled Synthesis of Multi-armed CdS Nanorod Architectures Using Monosurfactant System, *J. Am. Chem. Soc.* **2001**, 123, 5150.

[68] E. Arici, H. Hoppe, F. Schaffler, D. Meissner, M. A. Malik, N.S. Sariciftci, Hybrid solar cells based on inorganic nanoclusters and conjugated polymers, *Thin Solid Films* **2004**, 451–452, 612.

[69] M. A. Malik, N. Revaprasadu, P. O'Brien, A Novel Route for the Preparation of CuSe and CuInSe2 Nanoparticles, *Adv. Mater.* **1999**, 11, 1441.

[70] Y. Li, J. Wan, Z. Gu, The formation of cadmium sulfide nanowires in different liquid crystal systems, *Mater. Sci. Eng. A* **2000**, 286, 106.

[71] C. C. Chen, C. Y. Chao, Z. H. Lang, Simple Solution-Phase Synthesis of Soluble CdS and CdSe Nanorods, *Chem. Mater.* **2000**, 12, 1516.

[72] B. A. Simmons, S. C. Li, V. T. Jhon, G. L. Mcpherson, A. Bose, W. L. Zhou, J. B. He, *Nano Lett.* **2002**, 2, 263.

[73] P. Zhang, L. Gao, Synthesis and Characterization of CdS Nanorods via Hydrothermal Microemulsion, *Langmuir* **2003**, 19, 208.

[74] J. Yang, J. Zheng, S. Yu, L. Yang, G. Zhou, Y.T. Qian, Formation Process of CdS Nanorods via Solvothermal Route, *Chem. Mater.* **2000**, 12, 3259.

[75] M. Chen, Y. Xie, J. Lu, Y. Xiong, S. Zhang, Y. T. Qian, X. Liu, Synthesis of rod-, twinrod-, and tetrapod-shaped CdS nanocrystals using a highly oriented solvothermal recrystallization technique, *J. Mater. Chem.* **2002**, 12, 748.

[76] F. Gao, Q. Y. Lu, S.H. Xie, D. Y. Zhao, A Simple Route for the Synthesis of Multi-Armed CdS Nanorod-Based Materials, *Adv. Mater.* **2002**, 14, 1537.

[77] Y. W. Wang, G. W. Meng, L. D. Zhang, C. H. Liang, J. Zhang, Catalytic Growth of Large-Scale Single-Crystal CdS Nanowires by Physical Evaporation and Their Photoluminescence, *Chem. Mater.* **2002**, 14, 1773.

[78] W.-C. Kwak, T. G. Kim, W. Lee, S.-H. Han, Y.-M. Sung, Template-Free Liquid-Phase Synthesis of High-Density CdS Nanowire Arrays on Conductive Glass, *J. Phys. Chem. C* **2009**, 113, 1615.

[79] P. Chartier, H. N. Cong, C. Sene, Hybrid organic–inorganic photovoltaïc junctions:: case of the all thin-film CdSe/poly(3-methylthiophene) junction, *Sol. Energy Mater. Sol. Cells* **1998**, 52, 413.

[80] P. K. Nair, M. T. S. Nair, V. M. Garcia, O. L. Arenas, Y. Pena, A. Castillo, I. T. Ayala, O. Gomez-Daza, A. Sanchez, J. Campos, H. Hu, R. Suarez, M. E. Rincon, Semiconductor thin films by chemical bath deposition for solar energy related applications, *Sol. Energy Mater. Sol. Cells* **1998**, 52, 313.

[81] D. Lincot, Electrodeposition of semiconductors, *Thin Solid Films* **2005**, 487, 40.

[82] H. Hoppe, N. S. Sariciftci, Morphology of polymer/fullerene bulk heterojunction solar cells, *J. Mater. Chem.* **2006**, *16*, 45.

[83] Hoppe, J. Ph.D. Thesis, Linz, **2004**.

[84] L. Wang, Y. Liu, X. Jiang, D.H. Qin, Y. Cao, Enhancement of Photovoltaic Characteristics Using a Suitable Solvent in Hybrid Polymer/Multiarmed CdS Nanorods Solar Cells, *J. Phys. Chem. C* **2007**, 111, 9538.

[85] I. Gur, N. A. Fromer, C. P. Chen, A.G. Kanaras, A. P. Alivisatos, Hybrid Solar Cells with Prescribed Nanoscale Morphologies Based on Hyperbranched Semiconductor Nanocrystals, *Nano Lett.* **2007**, 7, 409.

[86] Y. Zhou, Y. Li, H. Zhong, J. Hou, Y. Ding, C. Yang, Y. Li, Hybrid nanocrystal/polymer solar cells based on tetrapod-shaped $CdSe_xTe_{1-x}$ nanocrystals , *Nanotechnology* **2006**, 17, 4041.

[87] B. Sun, E. Marx, N.C. Greenham, Photovoltaic Devices Using Blends of Branched CdSe Nanoparticles and Conjugated Polymers, *Nano Lett.* **2003**, 3, 961.

[88] B. Sun, H.J. Snaith, A. Dhoot, S. Westenhoff, N.C. Greenham, Vertically segregated hybrid blends for photovoltaic devices with improved efficiency, *J. Appl. Phys.* **2005**, 97, 014914.

112

[89] Y. S. Liu, L. Wang, D. H. Qin, Y. Cao, Photovoltaic Devices from Multi-Armed CdS Nanorods and Conjugated Polymer Composites, *Chin. Phys. Lett.* **2006**, 23, 3345.

[90] I. Gur, N.A. Fromer, A.P. Alivisatos, Controlled Assembly of Hybrid Bulk−Heterojunction Solar Cells by Sequential Deposition, *J. Phys. Chem. B* **2006**, 110, 25543.

[91] L. Manna, D.J. Milliron, A. Meisel, E.C. Scher, A.P. Alivisatos, Controlled growth of tetrapod-branched inorganic nanocrystals, *Nat. Mater.* **2003**, 2, 382.

[92] J. Chang, B. Sun, D.W. Breiby, M.M. Nielsen, T.I. Solling, M. Giles, R.D. McCullough, H. Sirringhaus, Enhanced Mobility of Poly(3-hexylthiophene) Transistors by Spin-Coating from High-Boiling-Point Solvents, *Chem. Mater.* **2004**, 16, 4772.

[93] J. Liu, E. Sheina, T. Kowalewski, R. D. McCullough, Tuning the Electrical Conductivity and Self-Assembly of Regioregular Polythiophene by Block Copolymerization: Nanowire Morphologies in New Di- and Triblock Copolymers, *Angew. Chem. Int. Ed.* **2002**, 41, 329.

[94] H. Yang, T.J. Shin, L. Yang, K. Cho, C.Y. Ryu, Z. Bao, Effect of Mesoscale Crystalline Structure on the Field-Effect Mobility of Regioregular Poly(3-hexyl thiophene) in Thin-Film Transistors, *Adv. Funct. Mater.* **2005**, 15, 671.

[95] D. J. Milliron, A. P. Alivisatos, C. Pitois, C. Edder, J. M. J. Frechet, Electroactive Surfactant Designed to Mediate Electron Transfer Between CdSe Nanocrystals and Organic Semiconductors, *Adv. Mater.* **2003**, 15, 58.

[96] J. Liu, T. Tanaka, K. Sivula, A. P. Alivisatos, J. M. J. Frechet, Employing End-Functional Polythiophene To Control the Morphology of Nanocrystal−Polymer Composites in Hybrid Solar Cells, *J. Am. Chem. Soc.* **2004**, 126, 6550.

[97] C. Querner, A. Benedetto, R. Demadrille, P. Rannou, P. Reiss, Carbodithioate-Containing Oligo- and Polythiophenes for Nanocrystals' Surface Functionalization, *Chem. Mater.* **2006**, 18, 4817.

[98] Q. Zhang, T.P. Russell, T. Emrick, Synthesis and Characterization of CdSe Nanorods Functionalized with Regioregular Poly(3-hexylthiophene), *Chem. Mater.* **2007**, 19, 3712.

[99] Z. Lin, Organic-Inorganic Nanohybrids through the Direct Tailoring of Semiconductor Nanocrystals with Conjugated Polymers, *Chem. Eur. J.* **2008**, 14, 6294.

[100] J. De Girolamo, P. Reiss, A. Pron, Supramolecularly Assembled Hybrid Materials via Molecular Recognition between Diaminopyrimidine-Functionalized Poly(hexylthiophene) and Thymine-Capped CdSe Nanocrystals, *J. Phys. Chem. C* **2007**, 111, 14681.

[101] J. De Girolamo, P. Reiss, A. Pron, Hybrid Materials from Diaminopyriminide-functionalized Poly(hexylthiophene) and Thymine-capped CdSe Nanocrystals: Part II Hydrogen Bond Assisted Layer-by-layer Molecular Level Processing, *J. Phys. Chem. C* **2008**, 112, 8797.

[102] W. J. E. Beek, M. M. Wienk, R. A. J. Janssen, Hybrid Solar Cells from Regioregular Polythiophene and ZnO Nanoparticles, *Adv. Funct. Mater.* **2006**, 16, 1112.

[103] P. J. Brown, D. S. Thomas, A. Kohler, J. Wilson, J. S. Kim, C. Ramsdale, H. Sirringhaus, R. H. Friend, Effect of interchain interactions on the absorption and emission of poly(3-hexylthiophene), *Phys. Rev. B* **2003**, 67, 064203.

[104] T. Ahn, H. Lee, S. H. Ha, Effect of annealing of polythiophene derivative for polymer light-emitting diodes, *Appl. Phys. Lett.* **2002**, 80, 392.

[105] T. Erb, U. Zhokhavets, G. Gobsch, S. Raleva, B. Stuhn, P. Schilinsky, Ch.

Waldauf, Ch. J. Brabec, Correlation Between Structural and Optical Properties of Composite Polymer/Fullerene Films for Organic Solar Cells, *Adv. Funct. Mater.* **2005**, 15, 1193.

[106]    J. J. Dittmer, E. A. Marseglia, H. R. Friend, Electron Trapping in Dye/Polymer Blend Photovoltaic Cells, *Adv. Mater.* **2000**, 12, 1270.

[107]    K. M. Coakley, D. McGehee, Photovoltaic cells made from conjugated polymers infiltrated into mesoporous titania, *Appl. Phys. Lett.* **2003**, 83, 3380.

[108]    L. B. Roberson, M. A. Poggi, J. Kowalik, G. P. Smestad, L. A. Bottomley, L. M. Tolbert, Correlation of morphology and device performance in inorganic–organic $TiO_2$–polythiophene hybrid solid-state solar cells, *Coord. Chem. Rev.* **2004**, 248, 1491.

[109]    R. Zhu, C. Y. Jiang, B. Liu, S. Ramakrishna, Highly Efficient Nanoporous $TiO_2$-Polythiophene Hybrid Solar Cells Based on Interfacial Modification Using a Metal-Free Organic Dye, *Adv. Mater.* **2009**, 21, 994.

[110]    T. On, A Simple Route for the Synthesis of Mesostructured Lamellar and Hexagonal Phosphorus-Free Titania ($TiO_2$), *Langmuir* **1999**, 15, 8561.

[111]    N. Kouklin, L. Menon, A. Z. Wong, D. W. Thompson, J. A. Woollam, P. F. Williams, S. Bandyopadhyay, Giant photoresistivity and optically controlled switching in self-assembled nanowires, *Appl. Phys. Lett.* **2001**, 79, 4423.

[112]    D. S. Xu, Y. J. Xu, D. P. Chem, L. G. Guo, L. L. Gui, Y. Q. Tang, Preparation of CdS Single-Crystal Nanowires by Electrochemically Induced Deposition, *Adv. Mater.* **2000**, 12, 520.

[113]    D. Routketvitch, T. Bigioni, M. Moskovits, J.M. Xu, Electrochemical Fabrication of CdS Nanowire Arrays in Porous Anodic Aluminum Oxide Templates, *J. Phys. Chem.* **1996**, 100, 14037.

[114]    J. S. Suh, J. S. Lee, Surface enhanced Raman scattering for CdS nanowires

deposited in anodic aluminum oxide nanotemplate, *Chem. Phys. Lett.* **1997**, 281, 384.

[115]     J. D. Klein, R. D. Herrick, D. Palmer, M.J. Sailor, C. J. Brumlick, C. R. Martin, Electrochemical fabrication of cadmium chalcogenide microdiode arrays, *Chem. Mater.* **1993**, 5, 902.

[116]     D. Xu, X. Shi, G. Guo, L. Gui, Y. Tang, Electrochemical Preparation of CdSe Nanowire Arrays, *J. Phys. Chem. B* **2000**, 104, 5061.

[117]     Y. Kang, D. Kim, Well-aligned CdS nanorod/conjugated polymer solar cells, *Sol. Energy Mater. Sol. Cells* **2006**, 90, 166.

[118]     K. M. Coakley, Y. Liu, M. D. McGehee, K. L. Frindell, G. D. Stucky, Infiltrating Semiconducting Polymers into Self-Assembled Mesoporous Titania Films for Photovoltaic Applications**,** *Adv. Funct. Mater.* **2003**, 13, 301.

[119]     P. Ravirajan, A. M. Peiró, M. K. Nazeeruddin, M. Graetzel, D. C. Bradley, J. R. Durrant, and J. Nelson*,* Hybrid Polymer/Zinc Oxide Photovoltaic Devices with Vertically Oriented ZnO Nanorods and an Amphiphilic Molecular Interface Layer, *J. Phys. Chem. B* **2006**, 110, 7635.

[120]     C. Goh, S. R. Scully, and M. D. McGehee, Effects of molecular interface modification in hybrid organic-inorganic photovoltaic cells, *J. Appl. Phys.* **2007**, 101, 114503.

[121]     W. W. Yu and X. Peng, Formation of High-Quality CdS and Other II-VI Semiconductor Nanocrystals in Noncoordinating Solvents: Tunable Reactivity of Monomers, *Angew. Chem. Int. Ed.* **2002**, 41, 2368.

[122]     S. J. Pearton, D. P. Norton, K. Ip, Y. W. Heo, T. Steiner, Recent progress in processing and properties of ZnO, *Superlattices Microstruct.* **2003**, 34, 3.

[123]     S. W. Lee, M.C. Jeong, J. M. Myoung, G. S. Chae, I.J. Chung, Magnetic alignment of ZnO nanowires for optoelectronic device applications, *Appl. Phys.*

*Lett.* **2007**, 90, 133115.

[124]    T. Makno, Y. Sagawa, M. Kawasaki, A. Ohtomo, R. Shiroki, K. Tamura, T. Yasuda, H. Koinuma, Band gap engineering based on $Mg_xZn_{1-x}O$ and $CdyZn_{1-y}O$ ternary alloy films, *Appl. Phys. Lett.* **2001**, 78, 1237.

[125]    W. Liu, S. Gu, S. Zhu, J. Ye, F. Qin, S. Liu, X. Zhou, L. Hu, R. Zhang, Y.Shi, Y. Zheng, The deposition and annealing study of MOCVD ZnMgO, *J. Crystal Growth* **2005**, 277, 416.

[126]    J. Y. Zhang, Z. T. Zhang, T. M. Wang, A New Luminescent Phenomenon of ZnO Due to the Precipitate Trapping Effect of MgO, *Chem. Mater.* **2004,** 16, 768.

[127]    G. N. Panin, A. N. Baranov, Y. J. Oh, T. W. Kang, Luminescence from ZnO/MgO nanoparticle structures prepared by solution techniques, *Curr. Appl. Phys.* **2004**, 4, 647.

[128]    H. Yang, Y. Li, D. P. Norton, S. J. Pearton, S. Jung, F. Ren, L.A. Boatner, Characteristics of unannealed ZnMgO/ZnO p-n junctions on bulk (100) ZnO substrates, *Appl. Phys. Lett.* **2005**, 86, 172103.

[129]    S. Sasa, M. Ozaki, K. Koike, M. Yano, M. Inoue, High-performance ZnO/ZnMgO field-effect transistors using a hetero-metal-insulator-semiconductor structure, *Appl. Phys. Lett.* **2006**, 89, 053502.

[130]    C. C. Lin, H. C. Liao, S. Y. Chen, and S. Y. Cheng. Luminescent and structural characteristics of ZnO nanorods fabricated by postannealing, *J. Vac. Sci. Technol. B* **2006**, 24, 304.

[131]    G. N. Panin, A. N. Baranov,Y. J. Oh, T. W. Kang, T. W. Kim, Effect of thermal annealing on the structural and the optical properties of ZnO/MgO nanostructures, *J. Cryst. Growth* **2005**, 279, 494.

[132]     Y. M. Lu, C. X. Wu, Z. P. Wei, Z. Z. Zhang, D. X. Zhao, J. Y. Zhang, Y. C. Liu, D. Z. Shen, X. W. Fan, Characterization of ZnO/Mg$_{0.12}$Zn$_{0.88}$O heterostructure grown by plasma-assisted molecular beam epitaxy, *J. Crystal Growth* **2005**, 278, 299.

[133]     J. F. Sarver, F. L. Katnack, F. A. Hummel, Phase Equilibria and Manganese-Activated Fluorescence in the System Zn$_3$(PO$_4$)$_2$-Mg$_3$(PO$_4$)$_2$, *J. Electrochem. Soc.* **1959**, 106, 960.

[134]     N. Arul Dhas, A. Zaban, A. Gedanken, Surface Synthesis of Zinc Sulfide Nanoparticles on Silica Microspheres: Sonochemical Preparation, Characterization, and Optical Properties, *Chem. Mater.* **1999**, 11, 806.

[135]     M. H. Huang, Y. Y. Wu, H. Feick, N. Tran, E. Weber, P. D. Yang, Catalytic Growth of Zinc Oxide Nanowires by Vapor Transport, *Adv. Mater.* **2001**, 13, 113.

[136]     Ohtomo, R. Shiroki, I. Ohkubo, H. Koinuma, M. Kawasaki, Thermal stability of supersaturated Mg$_x$Zn$_{1-x}$O alloy films and Mg$_x$Zn$_{1-x}$O/ZnO heterointerfaces, *Appl. Phys. Lett.* **1999**, 75, 4088.

[137]     T. W Zeng, Y. Y Lin, H. H. Lo, C. W. Chen, C. H. Chen, S. C. Liou, H. Y. Huang, W. F. Su, large interconnecting network within hybrid MEH-PPV/TiO2 nanorod photovoltaic devices, Nanotechnology **2006**, 17, 5387.

[138]     B. Kannan, K. Castelino, A. Majumdar, Design of Nanostructured Heterojunction Polymer Photovoltaic Devices, Nano Lett. **2003**, 3, 1729.

[139]     J. Nelson, *Curr. Opini. Solid State Mater. Sci.*, Organic photovoltaic films, **2002**, 6, 87

[140]     A. M. Peiró, P. Ravirajan, K. Govender, D. S. Boyle, P. O'Brien, D. D. C. Bradley, J. Nelson, and J. R. Durrant, Hybrid polymer/metal oxide solar cells based on ZnO columnar structures, *J. Mater. Chem.* **2006**, 16, 2088.

[141]    R. Cohen, L. Kronik, A. Shanzer, D. Cahen, A. Liu, Y. Rosenwaks, J. K. Lorenz, and A. B. Ellis, Molecular Control over Semiconductor Surface Electronic Properties: Dicarboxylic Acids on CdTe, CdSe, GaAs, and InP, *J. Am. Chem. Soc.* **1999,** 121, 10545.

[142]    G. J. Meyer, Molecular Approaches to Solar Energy Conversion with Coordination Compounds Anchored to Semiconductor Surfaces, *Inorg. Chem.* **2005**, 44, 6852.

[143]    S. Hugger, R. Thomann, T. Heinzel, T. Thurn-Albrecht, Semicrystalline morphology in thin films of poly(3-hexylthiophene), Colloid Polym. Sci. **2004**, 282, 932.

[144]    H. Sirringhaus, Device Physics of Solution-Processed Organic Field-Effect Transistors, *Adv. Mater.* **2005**, 17, 2411.

[145]    H. G. O. Sandberg, G. L. Frey, M. N. Shkunov, H. Sirringhaus, R. H. Friend, M. M. Nielsen, C. Kumpf, Ultrathin Regioregular Poly(3-hexyl thiophene) Field-Effect Transistors, *Langmuir* **2002**, 18, 10176.

[146]    C. J. Brabec, C. Winder, N. S. Sariciftci, J. C. Hummelen, A. Dhanabalan, P. A. van Hal, R. A. j. Janssen, A Low-Bandgap Semiconducting Polymer for Photovoltaic Devices and Infrared Emitting Diodes, *Adv, Funct. Mater.* **2002**, 12. 709.

[147]    P. Ravirajan, S. A. Haque, J. R. Durrant, D. Poplavskyy, D. D. C. Bradley, J. Nelson, Hybrid nanocrystalline TiO$_2$ solar cells with a fluorene–thiophene copolymer as a sensitizer and hole conductor, *J. Appl. Phys.* **2004**, 95, 1473.

[148]    A. Boulesbaa, A. Issac, D. Stockwell, Z. Huang, J. Huang,; J. Guo, T. Lian, Ultrafast Charge Separation at CdS Quantum Dot/Rhodamine B Molecule Interface, *J. Am. Chem. Soc.* **2007**, 129, 15132.

[149]    Lukas Schmidt-Mende, Shaik M. Zakeeruddin, and Michael Grätzel,

Efficiency improvement in solid-state-dye-sensitized photovoltaics with an amphiphilic Ruthenium-dye, *Appl. Phys. Lett.* **2005**, 86, 013504.

[150]     L. E. Brus, Electron–electron and electron-hole interactions in small semiconductor crystallites: The size dependence of the lowest excited electronic state, *J. Chem. Phys.* **1984**, 80, 4403.

[151]     L. E. Brus, simple model for the ionization potential, electron affinity, and aqueous redox potentials of small semiconductor crystallites, *J. Chem. Phys.* **1983**, *79*, 5566.

[152]     K. M. Coakley, M. D. McGehee, Conjugated Polymer Photovoltaic Cells, *Chem. Mater.* **2004**, 16, 4533.

[153]     D. Cui, J. Xu, T. Zhu, G. Paradee, S. Ashok, M. Gerhold, Harvest of near infrared light in PbSe nanocrystal-polymer hybrid photovoltaic cells, *Appl. Phys. Lett.* **2006**, 88, 183111.

[154]     A. A. R. Watt, D. Blake, J. H. Warner, E. A. Thomsen, E. L. Tavenner, H. Rubinsztein-Dunlop, P. Meredith, *J. Phys. D* **2005**, 38, 2006.

[155]     W. J. E. Beek, M. M. Wienk, M. Kemerink, X. N. Yang, R. A. J. Janssen, Hybrid Zinc Oxide Conjugated Polymer Bulk Heterojunction Solar Cells, *J. Phys. Chem. B* **2005**, 109, 9505.

[156]     Y. Kang, N. Park, D. Kim, Hybrid solar cells with vertically aligned CdTe nanorods and a conjugated polymer, *Appl. Phys. Lett.* **2005**, 86, 113101.

[157]     A. C. Arango, L. R. Johnson, V. N. Bliznyuk, Z. Schlesinger, S. A. Carter, H.-H. Hörhold, Efficient Titanium Oxide/Conjugated Polymer Photovoltaics for Solar Energy Conversion, *Adv. Mater.* **2000**, 12, 1689.

[158]     M. Matsumura, Y. Saho, H. Tsubomura, Photocatalytic hydrogen production from solutions of sulfite using platinized cadmium sulfide powder, *J. Phys. Chem.* **1983**, 87, 3807.

[159]    S. M. Lee, Y. W. Jun, S. N. Cho, J. Cheon, Single-Crystalline Star-Shaped Nanocrystals and Their Evolution: Programming the Geometry of Nano-Building Blocks, *J. Am. Chem. Soc.* **2002**, 124, 11244.

[160]    S. M. Lee, S. N. Cho, J. Cheon, Anisotropic Shape Control of Colloidal Inorganic Nanocrystals, *Adv. Mater.* **2003**, 15, 441.

[161]    J. Joo, H. B. Na, T. Yu, J. H. Yu, Y. W. Kim, F. Wu, J. Z. Zhang, T. Hyeon, Generalized and Facile Synthesis of Semiconducting Metal Sulfide Nanocrystals, *J. Am. Chem. Soc.* **2003**, 125, 11100.

[162]    A. Watt, E. Thomsen, P. Meredith, H. Rubinsztein-Dunlop, A new approach to the synthesis of conjugated polymer–nanocrystal composites for heterojunction optoelectronics, *Chem. Commun.* **2004**, 2334.

[163]    A. Watt, P. Meredith, J.D. Riches, S. Atkinson, H. Rubinsztein-Dunlop, A PbS quantum-cube: conducting polymer composite for photovoltaic applications, *Current Applied Physics* **2004**, 4, 320.

[164]    R. Adelung, O. C. Aktas, J. Franc, A. Biswas, R. Kunz, M. Elbahri, J. Kanzow, U. Schürmann, F. Faupel, Strain-controlled growth of nanowires within thin-film cracks, *Nat Mater* **2004**, 3, 375.

[165]    Q. Yang, K. Tang, C. Wang, Y. Qian, S. Zhang, PVA-Assisted Synthesis and Characterization of CdSe and CdTe Nanowires, *J Phys Chem B* **2002**, 106, 9227.

[166]    J. H. Zhan, X. G. Yang, D. W. Wang, S. D. Li, Y. Xie, Y. Xia, Y. Qian, Polymer-Controlled Growth of CdS Nanowires, *Adv Mater* **2000**, 12, 1348.

[167]    Y. Xie, Z. Qiao, M. Chen, X. Liu, Y. Qian, $\gamma$-Irradiation Route to Semiconductor/Polymer Nanocable Fabrication, *Adv. Mater.* **1999**, 11, 1512.

[168]    H. Niu, L. Zhang, M. Gao, Y. Chen, Amphiphilic ABC Triblock Copolymer-Assisted Synthesis of Core/Shell Structured CdTe Nanowires,

*Langmuir* **2005**, 21, 4205.

[169]    C. S. Yang, D. D. Awschalom, G. D. Stucky, Growth of CdS Nanorods in Nonionic Amphiphilic Triblock Copolymer Systems, *Chem Mater* **2002**, 14, 1277.

[170]    I. Gur, N. A. Fromer, M. L. Geier, A. P. Alivisatos, Air-Stable All-Inorganic Nanocrystal Solar Cells Processed from Solution, *Science* **2005**, 310, 462.

[171]    B. Sun, N. C. Greenham, Improved efficiency of photovoltaics based on CdSe nanorods and poly(3-hexylthiophene) nanofibers, *Phys Chem Chem Phys* **2006**, 8, 3557.

[172]    Tom J. Savenije, Jessica E. Kroeze, Xiaoniu Yang, Joachim Loos, The formation of crystalline P3HT fibrils upon annealing of a PCBM:P3HT bulk heterojunction, *Thin Solid Films* **2006**, 511, 2.

[173]    S. D. D. V. Rughooputh, S. Hotta, A. J. Heeger, F. Wudl, Chromism of soluble polythienylenes, *J. Polym. Sci., Polym. Phys. Ed.* **1987**, 25, 1071.

[174]    A. Stavrinadis, R. Beal, J. M. Smith, H. E. Assender, and A. A. R. Watt, Direct Formation of PbS Nanorods in a Conjugated Polymer, *Adv. Mater.* **2008**, 20, 3105.

[175]    F. Chen, R. Zhou, L. Yang, M. Shi, G. Wu, M. Wang, and H. Chen, One-Step Fabrication of CdS Nanorod Arrays via Solution Chemistry, *J. Phys. Chem. C* **2008**, 112, 13457.

[176]    M. E. Wankhede and S. K. Haram, Synthesis and Characterization of Cd−DMSO Complex Capped CdS Nanoparticles, *Chem. Mater.* **2003,** 15, 1296.

[177]    S. Hongyu, X. Li, Y. Chen, W. Li, F. Li, B. Liu and X. Zhang, The control of the growth orientations of electrodeposited single-crystal nanowire arrays: a case study for hexagonal CdS, *Nanotechnology*, **2008**, 19, 225601.

[178]    J. Yu, D. H. Hu, P. F. Barbara, Unmasking Electronic Energy Transfer of

Conjugated Polymers by Suppression of $O_2$ Quenching, *Science* **2000**, 289, 1327.

[179]    G. D. Scholes, D. S. Larsen, G. R. Fleming, G. Rumbles, P. L. Burn, Origin of line broadening in the electronic absorption spectra of conjugated polymers: Three-pulse-echo studies of MEH-PPV in toluene, *Phys. Rev. B* **2000**, 61, 13670.

[180]    L. J. A. Koster, V. D. Mihailetchi, R. Ramaker, and P. W. M. Blom, Light intensity dependence of open-circuit voltage of polymer:fullerene solar cells, *Appl. Phys. Lett.* **2005**, 86, 123509.

[181]    J. M. Kroon, S.C. Veenstra, L. H. Slooff, W. J. H Verhees, M. M. Koetse, J. Sweelssen, H. F. M. Schoo, W. J. E. Beek, M. M. Wienk, R. A. J. Janssen, X. Yang, J. Loos, V. D. Michailetchi, P. W. M. Blom, J. Knol, J. C. Hummelen, Polymer based photo-voltaics: novel concepts, materials and state-of-the art efficiencies, in: 20th European Photovoltaic Solar Energy Conference and Exhibition, Barcelona, Spain, 6–10 June **2005**.

[182]    J. Y. Kim, K. Lee, N. E. Coates, D. Moses, T. Nguyen, M. Dante, A. J. Heeger, Efficient tandem polymer solar cells fabricated by all-solution processing, *Science* **2007**, 317, 222.

[183]    G. Yu, J. Gao, J. C. Hummelen, F. Wudl, A. J. Heeger, Polymer photovoltaic cells: Enhanced efficiencies via a network of internal donor-acceptor, *Science* **1995**, 270, 1789.

[184]    D. E. Markov, E. Amsterdam, P. W. M. Blom, A. B. Sieval, J. C. J. Hummelen, Accurate Measurement of the Exciton Diffusion Length in a Conjugated Polymer Using a Heterostructure with a Side-Chain Cross-Linked Fullerene Layer, *J. Phys. Chem. A* **2005**, 109, 5266.

[185]    J. J. M. Halls, K. Pichler, R. H. Friend, S. C. Moratti, A. B. Holmes, Exciton diffusion and dissociation in a poly(p-phenylenevinylene)/$C_{60}$ heterojunction photovoltaic cell, *Appl. Phys. Lett.* **1996**, 68, 3120.

[186]    G. Li, V. Shrotriya, J. Huang, Y. Yao, T. Moriarty, K. Emery and Y. Yang, High-efficiency solution processable polymer photovoltaic cells by self-organization of polymer blends, *Nat. Mater.* **2005**, 4**,** 86.

[187]    V. D. Mihailetchi, H. Xie, B. Boer, L. M. Popescu, J. C. Hummelen, P. W. M. Blom and L. J. A. Koster, Origin of the enhanced performance in poly(3-hexylthiophene): [6,6]-phenyl $C_{61}$-butyric acid methyl ester solar cells upon slow drying of the active layer, *Appl. Phys. Lett.* **2006**, 89, 012107.

[188]    Y. Kim, S. A. Choulis, J. Nelson, D. D. C. Bradley, S. Cook and J. R. Durrant ,Device annealing effect in organic solar cells with blends of regioregular poly(3-hexylthiophene) and soluble fullerene, *Appl. Phys. Lett.* **2005**, 86, 063502.

[189]    H. Hoppe and N. S. Sariciftci, Morphology of polymer/fullerene bulk heterojunction solar cells, *J. Mater. Chem* **2006**, 16, 45.

[190]    D. Chirvase, J. Parisi, J. C. Hummelen and V. Dyakonov, Influence of nanomorphology on the photovoltaic action of polymer–fullerene composites, *Nanotechnology* **2004**, 15, 1317.

[191]    M. Reyes-Reyes, K. Kim, D. L. Carroll, High-efficiency photovoltaic devices based on annealed poly(3-hexylthiophene) and 1-(3-methoxycarbonyl)-propyl-1- phenyl-(6,6)$C_{61}$ blends, *Appl. Phys. Lett.* **2005**, 87, 083506.

[192]    J. D. Olson, G. P. Gray, S. A. Carter, Optimizing hybrid photovoltaics through annealing and ligand choice, *Sol. Energy Mater. Sol. Cells* **2009**, 93, 519.

[193]    H. C. Liao, S. Y. Chen, and D. M. Liu, In-Situ Growing CdS Single-Crystal Nanorods via P3HT Polymer as a Soft Template for Enhancing Photovoltaic Performance, *Macromolecules* **2009**, 42, 6558.

[194]    S. Hotta, S. D. D. V. Rughooputh, A. J. Heeger, Conducting polymer

composites of soluble polythiophenes in polystyrene, *Synth. Met.* **1987**, 22, 79.

[195]    O. Inganas, W. R. Salaneck, J. E. Osterholm, J. Laakso, Thermochromic and solvatochromic effects in poly(3-hexylthiophene), *Synth. Met.* **1988**, 22, 395.

[196]    M. Sharma, D. Kaushik, R.R. Singh, R.K. Pandey, Study of electropolymerised polyaniline films using cyclic voltammetry, atomic force microscopy and optical spectroscopy, *J. Mater. Sci.: Mater. Electron.* **2006**, 17, 537.

[197]    L. Li, C. M. Chan, K. L. Yeung, J. X. Li, K. M. Ng, Y. Lei, Direct Observation of Growth of Lamellae and Spherulites of a Semicrystalline Polymer by AFM, *Macromolecules* **2001**, 34, 316.

[198]    L. MANDELKERN, "Crystallization of Polymers" (McGraw- Hill, New York, 1964). DSC.

[199]    S. Miyanishi, K. Tajima and K. Hashimoto, Morphological Stabilization of Polymer Photovoltaic Cells by Using Cross-Linkable Poly(3-(5-hexenyl)thiophene), Macromolecules **2009**, 42, 1610.

[200]    A. Swinnen, I. Haeldermans, M. vande Ven, J. D'Haen, G. Vanhoyland, S. Aresu, M. D'Olieslaeger, J. Manca, Tuning the Dimensions of C60-Based Needlelike Crystals in Blended Thin Films, *Adv. Funct. Mater*. **2006**, 16, 760.

[201]    A. Star, J. F. Stoddart, D. Steuerman, M. Diehl, A. Boukai, E. W. Wong, X. Yang, S. W. Chung, H. Choi, J. R. Heath, Preparation and Properties of Polymer-Wrapped Single-Walled Carbon Nanotubes, *Angew. Chem. Int. Ed.* **2001**, 40, 1721.

[202]    J. Chen, H. Liu, W. A. Weimer, M. D. Halls, D. H. Waldeck, G. C. Walker, Noncovalent Engineering of Carbon Nanotube Surfaces by Rigid, Functional Conjugated Polymers, *J. Am. Chem. Soc.* **2002**, 124, 9034.

[203]    O. Jardetzky, G.C.K. Roberts, NMR in Molecular Biology, Academic Press,

New York, **1981**, 227.

[204]    R. Tannenbaum, M. Zubris, K. David, D. Ciprari, K. Jacob, I. Jasiuk, N.
Dan, FTIR Characterization of the Reactive Interface of Cobalt Oxide
Nanoparticles Embedded in Polymeric Matrices, *J. Phys. Chem. B* **2005**, *110*,
2227.

[205]    Lipatov, Y. S. *Polymer Reinforcement*; Chem Tec Publishing: Ontario
Canada, **1995**, 385.

[206]    E. Arici, H. Hoppe, F. Schaffler, D. Meissner, M. A. Malik, N. S. Sariciftci,
Morphology effects in nanocrystalline CuInSe$_2$-conjugated polymer hybrid
systems, *Appl. Phys. a-Mater. Sci. Processing* **2004**, 79, 59.

[207]    C. C. Oey, A. B. Djurišić, H. Wang, K. K. Y. Man, W. K. Chan, M. H. Xie, Y.
H. Leung, A. Pandey, J-M Nunzi and P. C. Chui, Polymer–TiO$_2$ solar cells: TiO$_2$
interconnected network for improved cell performance, *Nanotechnology* **2006**,
17, 706.

[208]    M. Law, L.E. Greene, J.C. Johnson, R. Saykally, P. Yang, Nanowire
dye-sensitized solar cells, *Nature Mater.* **2005,** 4**,** 455.

[209]    P. Charoensirithavorn, S. Yoshikawa, High-efficiency Dye-sensitized Solar
Cell Based on ZnO Nanorod Arrays Electrode, *Mater. Res. Soc. Symp. Proc.*
**2007**, 974, CC07.

[210]    E. Joanni, R. Savu, de Sousa G ´oesM, P. R. Bueno, J. N. de Freitas, A. F.
Nogueira, E. Longoa and J. A. Varela, Dye-sensitized solar cell architecture
based on indium–tin oxide nanowires coated with titanium dioxide, *Scr. Mater.*
**2007**, 57, 277.

[211]    H. W. Wang, C. F. Ting, M. K. Hung, C. H. Chiou, Y. L. Liu, Z. Liu, K. R
Ratinac and S. P. Ringer, Three-dimensional electrodes for dye-sensitized solar
cells: synthesis of indium–tin-oxide nanowire arrays and ITO/TiO$_2$ core–shell

nanowire arrays by electrophoretic deposition, *Nanotechnology* **2009**, 20, 055601.

[212]    E. Elangovan, K. Ramamurthi, Optoelectronic properties of spray deposited SnO$_2$:F thin films for window materials in solar cells, *J. Optoelectron. Adv. Mater.* **2003**, 5, 45.

[213]    N. Park, M. G. Kang, K. S. Ryu, K. M. Kim, S. H. Chang, Photovoltaic characteristics of dye-sensitized surface-modified nanocrystalline SnO$_2$ solar cells, *J. Photochem. Photobiol. A* **2004**, 161, 105.

[214]    B. Russo, G. Z. Cao, Fabrication and characterization of fluorine-doped thin oxide thin films and nanorod arrays via spray pyrolysis, *Appl. Phys. A* **2008**, 90, 311.

[215]    Y. J. Lee, M. T. Lloyd, D. C. Olson, R. K. Grubbs, P. Lu, R. J. Davis, J. A. Voigt and J. W. P. Hsu, Optimization of ZnO Nanorod Array Morphology for Hybrid Photovoltaic Devices, *J. Phys. Chem. C*, **2009**, 113, 15778.

[216]    J. C. Lee, W. Lee, S. H. Han, T. G. Kim, Y. M. Sung, Synthesis of hybrid solar cells using CdS nanowire array grown on conductive glass substrates, *Electrochemistry Communications* **2009**, 11, 231.

[217]    M. S. Arnold, P. Avouris, Z. W. Pan, Z. L. Wang, Field-Effect Transistors Based on Single Semiconducting Oxide Nanobelts, *J. Phys. Chem. B* **2003**, 107, 659.

[218]    C. H. Seager, S. M. Myers, Quantitative comparisons of dissolved hydrogen density and the electrical and optical properties of ZnO, *J. Appl. Phys.* **2003**, 94, 2888.

[219]    C. Yang, F.P. Orfino, S. Holdcroft, A Phenomenological Model for Predicting Thermochromism of Regioregular and Nonregioregular Poly(3-alkylthiophenes), *Macromolecules* **1996**, 29, 6510.

[220]    C. Roux, M. Leclerc, Rod-to-coil transition in alkoxy-substituted polythiophenes, *Macromolecules* **1992**, 25, 2141.

[221]    A. P. Alivisatos, Semiconductor Clusters, Nanocrystals, and Quantum Dots, *Science* **1996,** 271, 933.

[222]    V. L. Klimov, A. A.`Mikhailovsky, S. Xu, A. Malko, J. A. Hollingsworth, C. A. Leatherdale, H. J. Eisler, M. G. Bawendi, Optical Gain and Stimulated Emission in Nanocrystal Quantum Dots, *Science* **2000** 290 314.

[223]    X. G. Peng, L. Manna, W. D. Yang, J. Wickham, E. Scher, A. Kadavanich, A. P. Alivisatos, Shape control of CdSe nanocrystals, *Nature* **2000,** 404, 59.

[224]    S. Chaudhary, M. Ozkan, W. C. Chan, Trilayer hybrid polymer-quantum dot light-emitting diodes, *Appl. Phys. Lett.* **2004**, 84, 2925.

[225]    S. Coe, W. K. Woo, M. Bawendi, V. Bulovic, Electroluminescence from single monolayers of nanocrystals in molecular organic devices, *Nature* **2002,**420, 800.

[226]    B. Ballou, B. C. Lagerholm, L. A. Ernst, M. P. Bruchez, A. S. Waggoner, Noninvasive Imaging of Quantum Dots in Mice, *Bioconjugate Chem.* **2004,** 15, 79.

[227]    B. Dubertret, P. Skourides, D. J. Norris, V. Noireaux, A. H. Brivanlou, A. Libchaber, In Vivo Imaging of Quantum Dots Encapsulated in Phospholipid Micelles, *Science* **2002,** 298, 1759.

[228]    X. Y. Wu, H. J. Liu, J. Q. Liu, K. N. Haley, J. A. Treadway, J. P. Larson, N. F. Ge, F. Peale, Bruchez M P Immunofluorescent labeling of cancer marker Her2 and other cellular targets with semiconductor quantum dots, *Nat. Biotechnol* **2003,** 21, 41.

[229]    X. G. Peng, M. Xiao, Photoactivated CdSe Nanocrystals as Nanosensors for Gases, *Nano Lett.* **2003,** 3, 819.

[230]    A. B. Ellis, Probing Polymer Adsorption Using an Emissive Semiconductor Substrate:  Adsorption of Poly(acrylic acid) onto Cadmium Selenide, *Macromolecules* **2000,** 33, 582.

[231]    L. M. Liz-Marzán, P. Mulvaney, The Assembly of Coated Nanocrystals, *J. Phys. Chem. B* **2003,** 107, 7312.

[232]    S. Xu, J. Zhang, C. Paquet, Y. Lin, E. Kumacheva, From Hybrid Microgels to Photonic Crystals, *Adv. Funct. Mater.* **2003**, 13, 468.

[233]    J. Lee, V. C. Sundar, J. R. Heine, M. G. Bawendi, K. F. Jensen, Full Color Emission from II-VI Semiconductor Quantum Dot-Polymer Composites, *Adv. Mater.* **2000,** 12, 1102.

[234]    H. Zhang, Z. Cui, Y. Wang, K. Zhang, X. Ji, C. Lü, B. Yang, M. Gao, From Water-Soluble CdTe Nanocrystals to Fluorescent Nanocrystal-Polymer Transparent Composites Using Polymerizable Surfactants, *Adv. Mater.* **2003,** 15, 777.

[235]    S. C. Farmer and T. E. Patten, Photoluminescent Polymer/Quantum Dot Composite Nanoparticles, *Chem. Mater.* **2001**, 13, 3920.

[236]    N. Gaponik, D. Talapin V, A. L. Rogach, A. Eychmuller and H. Weller, Efficient Phase Transfer of Luminescent Thiol-Capped Nanocrystals:  From Water to Nonpolar Organic Solvents, *Nano Lett.* **2002,** 2, 803.

[237]    M. Moffitt, H. Vali and A. Eisenberg, Spherical Assemblies of Semiconductor Nanoparticles in Water-Soluble Block Copolymer Aggregates, *Chem. Mater.* **1998,** 10, 1021.

[238]    F. M. Pavel and R. A. Mackay, Reverse Micellar Synthesis of a Nanoparticle/Polymer Composite, *Langmuir* **2000,** 16, 8568.

[239]    C. H. Chew, T. D. Li, L. H. Gan, C. H. Quek and L. M. Gan, Bicontinuous-Nanostructured Polymeric Materials from Microemulsion

Polymerization, *Langmuir* **1998,** 14, 6068.

[240]     M. Brust, M. Walker, D. Bethell, D. J. Schiffrin and R. Whyman, Journal of the Chemical Society, Chemical Communications, *J. Chem. Soc. Chem. Commun.* **1994,** 801.

[241]     C. L. Li and N. Murase, Synthesis of Highly Luminescent Glasses Incorporating CdTe Nanocrystals through Sol−Gel Processing, *Langmuir* **2004,** 20 1.

[242]     H. Zhang, Z. Cui, Y. Wang, K. Zhang, X. Ji, C. Lu, B. Yang and M. Gao, From Water-Soluble CdTe Nanocrystals to Fluorescent Nanocrystal-Polymer Transparent Composites Using Polymerizable Surfactants *Adv. Mate*r. **2003,** 15, 777.

[243]     E. Kroll, F. M. Winnik, R. F. Ziolo, In Situ Preparation of Nanocrystalline γ-Fe2O3 in Iron(II) Cross-Linked Alginate Gels, *Chem. Mater.* **1996,** 8, 1594.

[244]     R. S. Kane, R. E. Cohen, R. Silley, Synthesis of Doped ZnS Nanoclusters within Block Copolymer Nanoreactors, *Chem. Mater.* **1999,** 11, 90.

[245]     J. Dai, M. L. Bruening, Catalytic Nanoparticles Formed by Reduction of Metal Ions in Multilayered Polyelectrolyte Films, *Nano Lett.* **2002,** 2, 497.

[246]     T. C. Wang, M. F. Rubner, R. E. Cohen, Polyelectrolyte Multilayer Nanoreactors for Preparing Silver Nanoparticle Composites: Controlling Metal Concentration and Nanoparticle Size, *Langmuir* **2002,** 18, 3370.

[247]     Z. B. Sun, W. Q. Chen, X. Z. Dong, and X. M. Duan, A Facile Size-control Method of CdS Nanoparticles In-situ Synthesized in Polymer Matrix by Adjusting Ratio of Acidic Acid with Metallic Complex in Acrylate Photoresist Resin, *Chemistry Letters* **2007,** 36, 156.

[248]     T. D. Luccio, A. M. Laera, and L. Tapfer, Controlled Nucleation and Growth of CdS Nanoparticles in a Polymer Matrix, *J. Phys. Chem. B* **2006,** 110,

12603.

[249]     M. Moffitt, H. Vali, A. Eisenberg, Spherical Assemblies of Semiconductor Nanoparticles in Water-Soluble Block Copolymer Aggregates, *Chem. Mater.* **1998,** 10, 1021.

[250]     L. Spanhel, M. Haase, H. Weller, A. Henglein, Photochemistry of colloidal semiconductors. 20. Surface modification and stability of strong luminescing CdS particles**,** *J. Am. Chem. Soc.* **1987,** 109, 5649.

[251]     Y. Y. Liu, T. H. Tung, T. Y. Li, S. Y. Chen, and D. M. Liu, In situ synthesis of hybrid nanocomposite with highly order arranged amorphous metallic copper nanoparticle in poly(2-hydroxyethyl methacrylate) and its potential for blood-contact uses, *Acta Biomaterialia* **2008,** 4, 2052.

[252]     P. Q. Zhao, X. L. Wu, J. Y. Fan, K. C. Paul and G. G. Siu, Enhanced and tunable blue luminescence from CdS nanocrystal–polymer composites, *Scripta Materialia*, **2006,** 5,5 1123.

[253]     R. Tsu and D. Babić , Doping of a quantum dot, *Appl. Phys. Lett.* **1994,** 64, 1806.

[254]     A. Franceschetti and A. Zunger, Pseudopotential calculations of electron and hole addition spectra of InAs, InP, and Si quantum dots, *Phys. Rev. B* **2000,** 62, 2614.

[255]     M. Zahn, Y. Oohi, D. B. Fenneman, R. J Gripshover, V. H. Gehman, Dielectric properties of water and water/ethylene glycol mixtures for use in pulsed power system design, *Proceedings of the IEEE* **1986,** 74, 1182.

[256]     L. Gao and J. Z. Gu, Effective dielectric constant of a two-component material with shape distribution, *J. Phys. D: Appl. Phys.* **2002,** 35, 267.

[257]     L. E. Brus, A simple model for the ionization potential, electron affinity, and aqueous redox potentials of small semiconductor crystallites, *J. Chem. Phys.*

**1983,** 79, 5566.

[258]     D. Babi´c, R. Tsu and R. F. Greene, Ground-state energies of one- and two-electron silicon dots in an amorphous silicon dioxide matrix, *Phys. Rev. B* **1992,** 45, 14150.

[259]     M. Iwamatsu, M. Fujiwara, N. Happo and K. Horii, Effects of dielectric discontinuity on the ground-state energy of charged Si dots covered with a $SiO_2$ ayer, *J. Phys. Condens. Matter* **1997,** 9, 9881.

[260]     G. Allan, C. Delerue, M. Lannoo and E. Martin, Hydrogenic impurity levels, dielectric constant, and Coulomb charging effects in silicon crystallites, *Phys. Rev. B* **1995,** 52, 11982.

[261]     S. Das, S. Chakrabarti and S. Chaudhuri, Optical transmission and photoluminescence studies of ZnO–MgO nanocomposite thin films, *J. Phys. D: Appl. Phys.* **2005,** 38, 4021.

[262]     M. Lannoo, C. Delerue, and G. Allan, Screening in Semiconductor Nanocrystallites and Its Consequences for Porous Silicon, *Phys. Rev. Lett.* **1995,** 74, 3415.

# Curriculum Vitae

**Name: Hung-Chou Liao**

27.07.1981    Born in Taoyuan (Taiwan)

1999-2003    Undergraduate study in the department of materials science and engineering at National Chiao Tung University

2003-2005    Graduate study in the department of materials science and engineering at National Chiao Tung University

**Master Thesis:** Post Annealing and MgO Doping of ZnO nanorods

2005-2010    PhD study in the department of materials science and engineering at National Chiao Tung University (Taiwan)

**PhD Thesis:** In-situ Synthesis and Characterization of P3HT/CdS nanocomposites for Heterojunction Solar Cell Applications

# Publication list

## *Journal*

1. **H. C. Liao**, P. C. Kuo, C. C. Lin, S. Y. Chen, "Synthesis and optical properties of ZnO-ZnS core-shell nanotube arrays", *J. Vac. Sci. Technol., B* **24** (2006) 2198.

2. **H. C. Liao,** Y. Y. Liu, S. Y. Chen, D. M. Liu, "A nanoporous optically transparent CdS-pHEMA hybrid with high optical sensing capability to dielectric liquids", *Nanotechnology*, **20** (2009), 095504.

3. **H. C. Liao**, C. C. Lin, S. Y. Chen, "Effect of thermal annealing on the structural and the optical properties of MgO-Coated ZnO nanorods", *J. Nanosci. Nanotechnol.*, **10** (2010), 4696.

4. **H. C. Liao**, S. Y. Chen, D. M. Liu, "In-situ Growing CdS Single-Crystal Nanorods via P3HT Polymer as a Soft Template for Enhancing Photovoltaic Performance", *Macromolecules*, **42** (2009) 6558.

5. **H. C. Liao**, C. C. Lin, Y. W. Chen, S. Y. Chen, "Improvement in Photovoltaic Performance for Hybrid P3HT/elongated CdS nanocrystals solar cells with F-doped $SnO_2$ Arrays", *J. Mater. Chem.*, 20 (2010) 5429.

6. C. C. Lin, **H. C. Liao**, S. Y. Chen, and S. Y. Cheng, "Luminescent and structural properties of ZnO nanorods by post annealing", *J. Vac. Sci. Technol., B* **24** (2006) 304.

7. C. C. Lin, H. P. Chen, **H. C. Liao**, and S. Y. Chen, "Enhanced luminescent and electrical properties of hydrogen-plasma ZnO nanorods grown on wafer-scale flexible substrates", *Appl. Phys. Lett.,* **86** (2005) 183103.

8. T. Y. Liu, **H. C. Liao**, C. C. Lin, S. H. Hu, and S. Y. Chen, "Biofunctional ZnO Nanorod Arrays Grown on Flexible Substrates", *Langmuir.*, **22** (2006) 5804.

## *Conference Papers*

1. **H. C. Liao**, C. C. Lin, H. P. Chen, and S. Y. Chen "Photoluminescence study of arrayed ZnO nanorods on flexible substrate with hydrogen plasma treatment", International Electron Devices and Materials Symposia, Hsinchu, Taiwan, Dec. 20th -24th , 2004.

2. **H. C. Liao**, C. C. Lin, S. Y. Chen, and S. Y. Cheng, "High electron injection structure in hybrid solar cells", IEEE Proceedings of 2008 Conference on Optoelectronic and Microelectronic Materials and Devices (COMMAD '08), (2008) 285.

3. T. Y. Liu, **H. C. Liao**, C. C. Lin, S. S. Hu, C. S. Hsiao and S. Y. Chen, "Immobilization of proteins on arrayed ZnO nanorods grown on thermoplastic polyurethane (TPU) flexible substrate for biomedical applications", 2005 MRS Spring Meeting, San Francisco, California, U. S. A., March 28th - April 1st ,2005.

4. C. C. Lin, **H. C. Liao**, H. P. Chen, and S. Y. Chen, " Luminescent and structural properties of ZnO nanorods by post annealing", The 1st international conference on one-dimensional nanomatetrials, Taipei, Taiwan, Jan. 10th-14th, 2005.

5. P. C. Kuo, C. C. Lin, **H. C. Liao**, and S. Y. Chen, "Synthesis and properties of ZnS/ZnO core-shell nanotube arrays", The 1st international conference on one-dimensional nanomatetrials, Taipei, Taiwan, Jan. 10th-14th, 2005.